An X-ray survey of the 2 Jy sample – I. Is there an accretion mode dichotomy in radio-loud AGN?

Journal Item

Monthly Notices
of the
ROYAL ASTRONOMICAL SOCIETY

MNRAS **440,** 269–297 (2014)
Advance Access publication 2014 March 10

doi:10.1093/mnras/stu263

An X-ray survey of the 2 Jy sample – I. Is there an accretion mode dichotomy in radio-loud AGN?

B. Mingo,[1,2★] M. J. Hardcastle,[1] J. H. Croston,[3] D. Dicken,[4] D. A. Evans,[5] R. Morganti[6,7] and C. Tadhunter[8]

[1]*School of Physics, Astronomy & Mathematics, University of Hertfordshire, College Lane, Hatfield AL10 9AB, UK*
[2]*Department of Physics and Astronomy, University of Leicester, University Road, Leicester LE1 7RH, UK*
[3]*School of Physics and Astronomy, University of Southampton, Southampton SO17 1SJ, UK*
[4]*Institut d'Astrophysique Spatiale, Université Paris Sud, F-91405 Orsay, France*
[5]*Harvard–Smithsonian Center for Astrophysics, 60 Garden Street, Cambridge, MA 02138, USA*
[6]*ASTRON, the Netherlands Institute for Radio Astronomy, Postbus 2, NL-7990 AA Dwingeloo, the Netherlands*
[7]*Kapteyn Astronomical Institute, University of Groningen, PO Box 800, NL-9700 AV Groningen, the Netherlands*
[8]*Department of Physics and Astronomy, University of Sheffield, Hounsfield Road, Sheffield S3 7RH, UK*

Accepted 2014 February 6. Received 2014 February 6; in original form 2013 May 31

ABSTRACT

We carry out a systematic study of the X-ray emission from the active nuclei of the $0.02 < z < 0.7$ 2 Jy sample, using *Chandra* and *XMM–Newton* observations. We combine our results with those from mid-infrared, optical emission-line and radio observations, and add them to those of the 3CRR sources. We show that the low-excitation objects in our samples show signs of radiatively inefficient accretion. We study the effect of the jet-related emission on the various luminosities, confirming that it is the main source of soft X-ray emission for our sources. We also find strong correlations between the accretion-related luminosities, and identify several sources whose optical classification is incompatible with their accretion properties. We derive the bolometric and jet kinetic luminosities for the samples and find a difference in the total Eddington rate between the low- and high-excitation populations, with the former peaking at ∼1 per cent and the latter at ∼20 per cent Eddington. Our results are consistent with a simple Eddington switch when the effects of environment on radio luminosity and black hole mass calculations are considered. The apparent independence of jet kinetic power and radiative luminosity in the high-excitation population in our plots supports a model in which jet production and radiatively efficient accretion are not strongly correlated in high-excitation objects, though they have a common underlying mechanism.

Key words: galaxies: active – X-rays: galaxies.

1 INTRODUCTION

Our knowledge of active galactic nuclei (AGN), their observational properties and underlying mechanisms has vastly increased over the last few decades. We now know that these objects are powered through gas accretion on to some of the most supermassive black holes (SMBH) that sit in the centres of most galaxies (e.g. Magorrian et al. 1998). Radio-loud objects are particularly important to our understanding of AGN, since, despite the fact that they constitute only a small fraction of the overall population, it is during this phase that the impact of the AGN on their surrounding environment (through the production of jets and large-scale outflows and shocks) can be most directly observed and measured (e.g. Kraft et al. 2003; Cattaneo et al. 2009; Croston et al. 2011). Moreover, radio galaxies make up over 30 per cent of the massive galaxy population, and it is likely that all massive galaxies go through a radio-loud phase, as the activity is expected to be cyclical (e.g. Best et al. 2005; Saikia & Jamrozy 2009).

It is now commonly accepted that the dominant fuelling mechanism for radio-quiet objects is the accretion of cold gas on to the black hole from a radiatively efficient, geometrically thin, optically thick accretion disc (Shakura & Sunyaev 1973). However, this may not be the case for radio-loud objects. Hine & Longair (1979) noticed the existence of a population of radio-loud objects which lacked the high-excitation optical emission lines traditionally associated with AGN. These so-called low-excitation radio galaxies (LERGs) or weak-line radio galaxies (WLRGs) cannot be unified with the rest of the AGN population (high-excitation galaxies in general and radio galaxies in particular, or HERGs), since their

★ E-mail: bmingo@extragalactic.info

differences are not merely observational or caused by orientation or obscuration. It has been argued that LERGs accrete hot gas (see e.g. Hardcastle, Evans & Croston 2007a; Janssen et al. 2012) in a radiatively inefficient manner, through optically thin, geometrically thick accretion flows (RIAF; see e.g. Narayan & Yi 1995; Quataert 2003). These objects thus lack the traditional accretion structures (disc and torus) commonly associated with active nuclei (see e.g. van der Wolk et al. 2010; Fernández-Ontiveros et al. 2012; Mason et al. 2012), and seem to be channelling most of the gravitational energy into the jets, rather than radiative output. This makes them very faint and difficult to detect with any non-radio-selected surveys.

Current models (e.g. Bower et al. 2006; Croton et al. 2006) suggest that the radiatively efficient process may be dominant at high redshifts, and to be related to the scaling relation between black hole mass and host galaxy's bulge mass (e.g. Silk & Rees 1998; Heckman et al. 2004). Radiatively efficient accretion may also be the mode involved in the apparent correlation (and delay) between episodes of star formation and AGN activity in the host galaxies (e.g. Hopkins 2012; Ramos Almeida et al. 2013). Radiatively inefficient accretion is believed to be more common at low redshifts (Hardcastle et al. 2007a), and to play a crucial role in the balance between gas cooling and heating, both in the host galaxy and in cluster environments (McNamara & Nulsen 2007; Antognini, Bird & Martini 2012). These two types of accretion are often called 'quasar mode' and 'radio mode', which is somewhat misleading, given that there are radiatively efficient AGN with jets and radio lobes. This change of a predominant accretion mode with redshift is applicable primarily to the largest galaxies and most massive SMBH, since smaller systems evolve differently.

As pointed out by e.g. Laing et al. (1994), Blundell & Rawlings (2001), Rector & Stocke (2001), Chiaberge, Capetti & Celotti (2002) and Hardcastle, Evans & Croston (2009), it is important to note that the high/low-excitation division does not directly correlate with the FR I–FR II categories established by Fanaroff & Riley (1974), as is often thought. While most low-excitation objects seem to be FR I, there is a population of bona fide FR II LERGs, as well as numerous examples of FR I HERGs (e.g. Laing et al. 1994). This lack of a clear division is most likely caused by the complex underlying relation between fuelling, jet generation and environmental interaction. There seems to be evidence for a difference in the Eddington rate between both populations (see e.g. Hardcastle et al. 2007a; Ho 2009; Lin et al. 2010; Evans et al. 2011; Best & Heckman 2012; Mason et al. 2012; Plotkin et al. 2012; Russell et al. 2013), with LERGs typically accreting at much lower rates (<0.1 Eddington) than HERGs. Estimating the jet kinetic power is also complicated, given that the radio luminosity of a source depends on the environmental density (Hardcastle & Krause 2013; Ineson et al. 2013) and given the apparent difference in the particle content and/or energy distribution for typical FR I and FR II jets and lobes (see e.g. Croston et al. 2008; Godfrey & Shabala 2013).

In terms of their optical classification, HERGs are further split into quasars (QSOs), broad-line radio galaxies (BLRGs) and narrow-line radio galaxies (NLRGs), in consistency with the unified models, and in parallel with their radio-quiet counterparts (respectively, radio-quiet quasars, type 1 and type 2 radio-quiet AGN). We will use the optical classification for HERGs throughout this work.

In this paper, we analyse the X-ray emission from the 2 Jy sample of radio galaxies (Wall & Peacock 1985), with an approach based on that of Hardcastle, Evans & Croston (2006, 2009) used on the 3CRR galaxies. X-ray emission is less ambiguous than other wavelengths for an analysis of a sample such as the 2 Jy, which contains a variety of populations, in that, at these high luminosities, and in the nuclear regions we are considering, it is unequivocally linked to AGN activity. To fully understand the characteristics of this AGN activity, however, a multiwavelength approach is needed.

From works such as those of Hardcastle et al. (2006, 2009), we do know that LERGs follow the correlation of narrow-line galaxies (NLRGs) between soft X-ray and radio emission (Hardcastle & Worrall 1999), reinforcing the hypothesis that in radio-loud objects this X-ray component originates in the jet. One of the crucial points we aim to investigate in this paper is the dissimilarity between the NLRG and LERG populations.

Our aim is to study the correlations between the luminosities of the sources at different wavelengths, to link the emission produced in regions at various distances from the central black hole: from the disc and corona to the torus, the jet and the lobes. In doing so, we will investigate how accretion translates into radiative and kinetic output across the whole radio-loud population.

While many of the sources in the 3CRR catalogue have been observed in great detail, the multiwavelength coverage is not uniform, and the sample is not statistically complete in the X-rays, being more complete for redshifts <0.5. The observations of the 2 Jy sample, however, were taken with the explicit purpose of providing comparable measurements for all the objects in the sample. This consistency provides us with the opportunity to test whether the conclusions reached by Hardcastle et al. can be extrapolated to all radio-loud AGN or are related to the biased redshift distribution of the 3CRR sources.

Although it is well known that some of the physical mechanisms involved in radio-loud emission in AGN are similar to those found in X-ray binaries (see e.g. the review by Körding, Jester & Fender 2006), some caution must be applied, since there are also dissimilarities in the time-scales and fuelling processes involved. In this work, we will focus only on AGN, and the possible impact our results may have on understanding their observational properties, classification, accretion mode and the influence on their hosts.

For this paper, we have used a concordance cosmology with $H_0 = 70$ km s^{-1} Mpc^{-1}, $\Omega_m = 0.3$ and $\Omega_\Lambda = 0.7$.

2 DATA AND ANALYSIS

2.1 The sample

The 2 Jy sample (Wall & Peacock 1985; Tadhunter et al. 1993) is a sample of southern radio galaxies with flux greater than 2 Jy at 2.7 GHz.[1] The subsample we study has consistent, uniform multiwavelength coverage (see Section 2.4 for details) and, since we only include the steep-spectrum sources, it contains only genuinely powerful radio galaxies, while avoiding most of the effects caused by the strong relativistic beaming found in flat-spectrum sources. Other than excluding beamed sources, the radio selection, unlike those done in optical, infrared (IR) or X-ray wavelengths, selects no preferential orientation.

We analyse a statistically complete subsample of the 2 Jy steep-spectrum sources defined by Dicken et al. (2008), containing 45 objects with $\delta < +10^\circ$ and redshifts $0.05 < z < 0.7$. Particle acceleration in the jet causes the radio spectrum to flatten, thus the steep-spectrum ($\alpha > 0.5$, where we use the negative sign convention for α) selection of Dicken et al. (2008) excludes core- and jet-dominated sources. Flat-spectrum sources are typically blazars,

[1] For the most up-to-date version of the catalogue and ancillary data, see http://2Jy.extragalactic.info/

whose nuclear emission is completely dominated by the jet, and, although they are a small fraction of the total population, they appear brighter due to the jet contribution. By excluding these sources we eliminate a possible source of bias. Unlike Dicken et al. (2008), we have not included the flat-spectrum, core-dominated sources 3C 273 and PKS 0521−36 for comparison. The subsample studied here has consistent, uniform multiwavelength coverage, and, being statistically complete, includes all the sources within the flux, sky area, spectral types and redshift ranges defined.

From a radio classification point of view, the sample is dominated by powerful sources, with 6 objects being Fanaroff–Riley type I (FR I), 7 compact sources (CSS) and 32 Fanaroff–Riley type II (FR II; Morganti, Killeen & Tadhunter 1993; Morganti et al. 1999). As for emission-line classification, 10 sources are LERGs, 19 are NLRGs, 12 are BLRGs and 3 are QSOs (Tadhunter et al. 1993, 1998).

We have included in our analysis the 3CRR sources with $z < 1$ studied by Hardcastle et al. (2006, 2009). The 3CRR catalogue of Laing, Riley & Longair (1983) includes all the extragalactic radio sources with a flux greater than 10.9 mJy at 178 MHz and $\delta > +10^{\circ}$. By combining the 3CRR and 2 Jy catalogues, we are effectively selecting a large sample of the most radio-luminous galaxies in the Universe. To further improve the overall statistics, we also include in this work eight new observations of 3CRR sources not covered by Hardcastle et al. (2006, 2009) (see Appendix B for details).

The 2 Jy sample does not spatially overlap with the 3CRR catalogue, due to the different location of the sources (the 3CRR catalogue covers sources in the Northern hemisphere and the 2 Jy sources are in the Southern hemisphere). Some of the brightest sources are included in the original 3C catalogue, as is the case for e.g. the BLRG 3C 18 (PKS 0038+09). Although we have excluded core-dominated sources (to minimize the effects of beaming), the 2 Jy sample was selected at a higher frequency than the 3CRR sample. This higher frequency selection implies that, overall, more beamed sources are selected in the 2 Jy sample than for the 3CRR, which is a possible caveat to the assumption that no preferential AGN orientation is selected. Some of the implications of this fact are discussed in Section 4.

Although the 3CRR catalogue contains a much larger number of sources than the 2 Jy sample, it is not statistically complete in the X-rays, and has better coverage at lower redshifts. The observations of the 2 Jy sample are also more homogeneous. While it may seem that studying a reduced number of sources from the 2 Jy sample does not add much to the existing correlations, the characteristics of the sample and observations allow us to validate our previous results on the 3CRR catalogue, eliminating the low-redshift and inhomogeneous coverage biases. The 2 Jy sample also contributes a large number of NLRGs and LERGs to the overall statistics, which are particularly important to test our scientific goals. The combination of both samples provides a very powerful tool to explore the entire population of radio-powerful AGN.

Throughout this paper, we have kept the existing optical line classifications for the objects in both the 2 Jy and the 3CRR samples, for consistency, but we point out when evidence suggests that the optical classification does not accurately characterize a specific object. For the overall populations, low excitation and high excitation can be used as synonyms for radiatively inefficient and efficient AGN, respectively, but it is important to keep in mind that this does not hold true for some objects. The LERG/HERG classification is observational, based on optical line ratios, and in some cases it is not a good diagnostic for the true nature of the accretion process involved (a radiatively efficient object will be classified as an LERG if its high-excitation lines are not detected, while a radiatively inefficient source may be classified as an HERG if high-excitation lines are observed, even if they are produced by a mechanism that is not related to the AGN, e.g. photoionization by stellar activity).

2.2 X-ray data

There are 46 sources in our sample, with $0.05 < z < 0.7$. All have X-ray observations save for PKS 0117−15 (3C 38), which, unfortunately, was not observed by *XMM–Newton*, and is thus excluded from our analysis. Our sample, therefore, contains 45 2-Jy objects. The list of galaxies in the sample and the *Chandra* and *XMM–Newton* observations is shown in Table 1. Many of the observations were taken specifically for this project; *Chandra* observations were requested for the low-z sources to map any extended emission [jets, hotspots, lobes and any emission from a hot intergalactic medium (IGM) for sources in dense environments]. For the sources with $z > 0.2$, where extended structures cannot be resolved, we requested *XMM* observations instead, to maximize the signal-to-noise ratio of the AGN spectra, so as to allow spectral separation of the unresolved components. The new observations of the 2 Jy sample used in this work are indicated in Table 1. The list of new observations of 3CRR sources is given in Appendix B.

By limiting the redshift range to $z > 0.05$, we exclude both low-power sources and those whose extended emission may not be fully covered by *Chandra*. The extended emission (jets and lobes) in these low-z sources will be studied in detail in our second paper.

We analysed *Chandra* observations for the low-z sources in our sample. When using archival data we only considered ACIS-S and ACIS-I observations without gratings, and discarded calibration or very short observations that did not significantly contribute to the statistics. When more than one spectrum was extracted for a source, we carried out simultaneous fits. We reduced the data using CIAO 4.3 and the latest CALDB. We included the correction for VFAINT mode to minimize the issues with the background for all the sources with a count rate below 0.01 counts s^{-1} and observed in VFAINT mode. For sources with rates above this threshold and below 0.1 counts s^{-1}, the difference made by this correction is barely noticeable. For the brightest sources, the software is not able to properly account for the high count rate, considering some of these events as background, and resulting in dark 'rings appearing in the images, and the loss of a substantial number of counts.

We extracted spectra for all the sources, using extraction regions consistent with those of Hardcastle et al. (2009): a 2.5 pixel (1 pixel = 0.492 arcsec) radius circular region centred in the object as source and an immediately external annulus, with an outer radius of 4 pixels, for the background, to minimize the contamination from any thermal components in the circumnuclear regions. For very bright sources, we had to use larger regions to include most of the point spread function (PSF), namely a 20 pixel radius circle for the source and a 20 to 30 pixel circular annulus for the background. In the cases where pileup was present (PKS 0038+09, 0442−28, 0625−35, 0945−27, 1733−56, 1814−63, 2135−14), we corrected the auxiliary response file (ARF) as described by Hardcastle et al. (2006) and Mingo et al. (2011). We generated an energy versus flux table from an initial model fit, and fed it to ChaRT (the Chandra Ray Tracer; Carter et al. 2003), a tool that generates a PSF from a given model. Next, we fed the results to the tool MARX,[2] which produces an image of the simulated PSF. We then generated a new events file from our original data and an annular extraction region, identical to

[2] See http://space.mit.edu/CXC/MARX/docs.html

Table 1. Objects in the 2 Jy sample observed with *Chandra* (ACIS-S except for PKS 0625−53 and PKS 2135−14, which were taken with the ACIS-I) and *XMM–Newton* (MOS and PN). FR I and FR II stand for Fanaroff–Riley classes I and II, respectively; CSS stands for compact steep-spectrum. LERG, NLRG and BLRG stand, respectively, for low-excitation, narrow-line and broad-line radio galaxy; Q stands for quasar. New observations taken for this survey are indicated with an asterisk after the observation ID.

PKS	FR class	Type	z	Instrument	Obsid	Exp (ks)
0023−26	CSS	NLRG	0.322	*XMM*	0671870601*	19.55
0034−01	FR II	LERG	0.073	*Chandra*	02176	28.18
0035−02	FR II	BLRG	0.220	*Chandra*	09292	8.04
0038+09	FR II	BLRG	0.188	*Chandra*	09293	8.05
0039−44	FR II	NLRG	0.346	*XMM*	0651280901*	20.57
0043−42	FR II	LERG	0.116	*Chandra*	10319*	18.62
0105−16	FR II	NLRG	0.400	*XMM*	0651281001*	21.27
0213−13	FR II	NLRG	0.147	*Chandra*	10320*	20.15
0235−19	FR II	BLRG	0.620	*XMM*	0651281701*	13.67
0252−71	CSS	NLRG	0.566	*XMM*	0651281601*	19.17
0347+05	FR II	LERG	0.339	*XMM*	0651280801*	16.47
0349−27	FR II	NLRG	0.066	*Chandra*	11497*	20.14
0404+03	FR II	NLRG	0.089	*Chandra*	09299	8.18
0409−75	FR II	NLRG	0.693	*XMM*	0651281901*	13.67
0442−28	FR II	NLRG	0.147	*Chandra*	11498*	20.04
0620−52	FR I	LERG	0.051	*Chandra*	11499*	20.05
0625−35	FR I	LERG	0.055	*Chandra*	11500*	20.05
0625−53	FR II	LERG	0.054	*Chandra*	04943	18.69
0806−10	FR II	NLRG	0.110	*Chandra*	11501*	20.04
0859−25	FR II	NLRG	0.305	*XMM*	0651282201*	13.85
0915−11	FR I	LERG	0.054	*Chandra*	04969	98.2
				Chandra	04970	100.13
0945+07	FR II	BLRG	0.086	*Chandra*	06842	30.17
				Chandra	07265	20.11
1136−13	FR II	Q	0.554	*Chandra*	02138	9.82
				Chandra	03973	77.37
1151−34	CSS	Q	0.258	*XMM*	0671870201*	18.67
1306−09	CSS	NLRG	0.464	*XMM*	0671871201*	22.67
1355−41	FR II	Q	0.313	*XMM*	0671870501*	14.97
1547−79	FR II	BLRG	0.483	*XMM*	0651281401*	13.25
1559+02	FR II	NLRG	0.104	*Chandra*	06841	40.18
1602+01	FR II	BLRG	0.462	*XMM*	0651281201*	13.67
1648+05	FR I	LERG	0.154	*Chandra*	05796	48.17
				Chandra	06257	50.17
1733−56	FR II	BLRG	0.098	*Chandra*	11502*	20.12
1814−63	CSS	NLRG	0.063	*Chandra*	11503*	20.13
1839−48	FR I	LERG	0.112	*Chandra*	10321*	20.04
1932−46	FR II	BLRG	0.231	*XMM*	0651280201*	13.18
1934−63	CSS	NLRG	0.183	*Chandra*	11504*	20.05
1938−15	FR II	BLRG	0.452	*XMM*	0651281101*	18.17
1949+02	FR II	NLRG	0.059	*Chandra*	02968	50.13
1954−55	FR I	LERG	0.060	*Chandra*	11505*	20.92
2135−14	FR II	Q	0.200	*Chandra*	01626	15.13
2135−20	CSS	BLRG	0.635	*XMM*	0651281801*	17.57
2211−17	FR II	LERG	0.153	*Chandra*	11506*	20.04
2221−02	FR II	BLRG	0.057	*Chandra*	07869	46.20
2250−41	FR II	NLRG	0.310	*XMM*	0651280501*	13.67
2314+03	FR II	NLRG	0.220	*XMM*	0651280101*	21.67
				Chandra	12734	8.05
2356−61	FR II	NLRG	0.096	*Chandra*	11507*	20.05

the one we used to generate our spectra, but excluding the central few pixels. We used a code to fit a fifth-degree polynomial to the ratio of this events file and the whole simulated events file as a function of energy. The code reads in the ARF generated by CIAO and scales the effective area at each energy, using the polynomial fit, to effectively correct for the missing effective area due to the exclusion of the central pixels. The code then writes a new ARF which can be used to correct for the effects of excluding the central pixels.

For the sources at $0.2 < z < 0.7$, we used *XMM–Newton* observations. We extracted MOS and PN spectra for all of them, using SAS 11.0 and the latest calibration files. We used spatially coincident extraction regions for the three instruments whenever possible, using 30 arcsec source regions and off-source 90 arcsec background regions for the fainter sources, and 60 arcsec and 120 arcsec source and background regions, respectively, for the bright ones. Only a few observations were affected by flaring severe enough to require filtering. The most problematic case was PKS 1547−79, a faint source observed during a period of high flaring. We filtered the most severely affected parts of the observation.

Four low-z sources (PKS 0404+03, 1814−63, 2135−14, 2221−02) have *XMM* observations that we did not use, since the *Chandra* spectra adequately characterized the AGN spectrum and had no contamination from any circumnuclear gas. For PKS 2314+03, however, we used both the *Chandra* and *XMM* observations, given that its spectrum is quite peculiar.

We rebinned all the spectra to 20 counts per bin (after background subtraction) to make them compatible with χ^2 statistics.

2.3 Spectral fitting

For spectral fitting we used XSPEC version 12.5 and followed the same approach as Hardcastle et al. (2006, 2009), as follows. We considered the energy range between 0.4 and 7 keV for the *Chandra* spectra, and 0.3–8 keV for the *XMM* spectra. For the sources observed by *XMM*, the PN, MOS1 and MOS2 spectra were fitted simultaneously. The same approach was taken for those sources with more than one *Chandra* observation (PKS 0915−15, PKS 0945+07, PKS 1136−13, PKS 1648+05) and for PKS 2314+03, which was observed by both *Chandra* and *XMM* (see Table 1).

The typical X-ray spectrum of a radio-loud AGN can be approximated with a phenomenological model consisting of three main components. The accretion-related emission is well modelled with a power law that contributes mostly at energies between 2 and 10 keV, as predicted by accretion models (see e.g. Haardt & Maraschi 1991), and is also found in radio-quiet objects, although the slope of the power law changes. The soft excess in radio-loud objects, however, is not dominated by reflection of the accretion-related emission on to the disc, but is related to the jet (see e.g. Hardcastle & Worrall 1999; Hardcastle et al. 2006, 2009). This soft emission often dominates below 1 keV, and is also well modelled with a power law. When the torus obscures part of the emission, an intrinsic absorption component must be added to the model as well. Some objects also show fluorescence Fe Kα lines around 6.4 keV. When no obscuration is present (in broad-line objects), distinguishing both power-law components is not possible. Given that the jet-related emission in broad-line sources may be further complicated by relativistic beaming, and for consistency with the work of Hardcastle et al. (2006, 2009), we have considered both power-law components as one, when dealing with these sources. We are aware that this overestimates the luminosities (in the sense that the same luminosity may be ascribed to more than one component), and take this fact into account in our plots and correlation analysis.

We approached the fitting process in a systematic manner, by fitting all the sources to a set of three possible models. We first fitted each spectrum to a model consisting of a single power law with fixed Galactic absorption (wabs), for which we used the weighted

average extinction values of Dickey & Lockman (1990); we call this component 'unabsorbed' throughout this work, after Hardcastle et al. (2006, 2009). Secondly, we fitted the same model, adding an intrinsic absorption column (zwabs); we refer to this component as 'accretion-related'. We then fitted a combination of both models, and assessed which of the three provided a best fit to the data. When the photon index of either power law could not be constrained, we fixed the values to Γ=2.0 and 1.7, for the unabsorbed and accretion-related component, respectively [these values are consistent with what is found in most radio-loud AGN, and follow the choices of Hardcastle et al. (2006, 2009)]. When residuals were still present at high energies, we added a redshifted Gaussian profile for the Fe Kα line (zgauss), as required by the data. In the cases where a single power law provided a best fit to the data, we calculated an upper limit on the luminosity of the other component by fixing the parameters of the existing model, and adding the missing component with a fixed photon index. We added a fixed intrinsic absorption column $N_{\rm H} = 10^{23}$ cm^{-2} in the case of the accretion-related power law, a value consistent with what is seen in sources with detected, heavily absorbed components, and in agreement with that chosen by Evans et al. (2006) and Hardcastle et al. (2006, 2009).

While, for consistency, we have used the foreground $N_{\rm H}$ values of Dickey & Lockman (1990) for all the objects in the sample, we note that the Galactic extinction column may be underestimated for PKS 0404+03. *Herschel*/SPIRE observations show unusually bright Galactic cirrus dust emission in this area (Dicken et al., in preparation).

We derived the luminosity for the unabsorbed component, $L_{\rm X_u}$, from the normalization of the unabsorbed power law, and used XSPEC to calculate the 2–10 keV unabsorbed luminosity (corresponding to the accretion-related component, corrected for intrinsic absorption), $L_{\rm X_a}$. These energy ranges were chosen because they also allow direct comparison with the existing literature, and are consistent with our previous work.

We are aware of the fact that the brightest sources are likely to have measurable variations in their luminosity over time, although the most variable sources are excluded by the steep-spectrum selection. Variability is an intrinsic uncertainty characteristic of X-ray AGN studies, unavoidable unless follow-up observations are carried out for each source. We acknowledge that X-ray variability is a systematic effect that introduces scatter in our plots, and estimate the impact of variability and other systematics in Sections 4 and 5.

Some of the sources in our sample observed by *XMM* show signs of inhabiting rich environments, as shown in the optical by Ramos Almeida et al. (2011a, 2013). Our extraction regions may not be able to fully account for this; hence, some contamination of the soft X-ray component can be expected. PKS 0023−26 and PKS 0409−75 (together with PKS 0347+05, which has additional complications, as pointed out in Appendix A11) are the sources where contamination from a thermal component may be most relevant, given that they are relatively faint in the [O III] and mid-IR bands. We tested a model in which one of the power-law components is replaced by a thermal one (apec) in these sources, and obtained worse fits than those with the non-thermal model. We also attempted to quantify the amount of thermal emission by adding a thermal model on top of the two power laws, but the results were inconsistent due to the degeneracy between model components. Given that PKS 0023−26 is not clearly outlying in our plots, we assume that the dominant contribution to the soft X-ray emission is related to the AGN, rather than thermal emission. The case is less clear for PKS 0409−75, whose soft X-ray component is very bright, causing it to be an outlier. Beaming is not likely to be the cause of this excess, since the radio core is undetected at 20 GHz (Dicken et al. 2008), but it is possible that there is a contribution of inverse-Compton emission from the lobes, which are not resolved by *XMM*. In both PKS 0023−26 and PKS 0409−75, an in-depth study of the intracluster medium (ICM) X-ray emission is needed to fully quantify its contribution to the AGN X-ray luminosity.

The results of the spectral fits are displayed in Table 2. The sources where an Fe Kα line was detected are listed in Table 3. Details for each individual source, and references to previous work, are given in Appendix A. For consistency, we have checked our results, both on the derived luminosities and the extended emission (which we will analyse in detail in our second paper) against those obtained by Siebert et al. (1996), based on data from *ROSAT*, and find them in good agreement.

2.4 Other data

As outlined in Section 1, multiwavelength data for the 2 Jy sample were taken in a systematic manner, so that all the objects would have comparable measurements. This also allows us to establish a direct comparison with the existing data and analysis on the 3CRR sources (Hardcastle et al. 2006, 2009).

We used the Very Large Array and Australia Telescope Compact Array (ATCA) data at 5 GHz (both for overall and core luminosities) from Morganti et al. (1993, 1999). Since only some of the 2 Jy sources are covered by the Parkes catalogue (Wright & Otrupcek 1990), we calculated the spectral index from 408 MHz and 1.4 GHz observations (also from the Parkes catalogue) and extrapolated the results to 178 MHz. We used the same spectral index to extrapolate the 151 MHz fluxes, needed to calculate the jet kinetic power (see Section 5.1). The low-frequency fluxes for PKS 1934−63 are upper limits, since the source is self-absorbed in radio.

For the IR, we used 24 μm data taken by *Spitzer*, from Dicken et al. (2008, 2009). All the targets in the 2 Jy sample have deep *Spitzer* and *Herschel* observations at 24, 70, 100 and 160 μm, and ∼90 per cent (including all the targets in the steep-spectrum subsample) have *Spitzer*/IRS mid-IR spectra (Dicken et al. 2012). The 3C sources were observed at 15 μm (rest-frame), a band that is similar enough to *Spitzer*'s 24 μm (after rest-frame correction) to allow direct comparison. We studied the behaviour of a number of sources at both wavelengths, and estimated that the deviation in luminosity caused by the difference between 15 and 24 μm was well below 10 per cent in all cases.

For the optical line classification, we used the complete, deep Gemini GMOS-S data from Tadhunter et al. (1993, 1998). *K*-band magnitudes of the host galaxies were taken from Inskip et al. (2010) and *K*-corrected using the relations given by Glazebrook et al. (1995) and Mannucci et al. (2001). The values presented in the tables are *K*-corrected.

For the 3CRR sources, we used the data from Hardcastle et al. (2006, 2009). In this case, the 178 MHz fluxes were measured as part of the sample definition, but 1.4 GHz and 151 MHz fluxes had to be extrapolated from these measurements and the 178–750 MHz spectral indices.[3] Details of the 3CRR data are given in Appendix B.

3 THE X-RAY 2 JY SAMPLE

In our analysis of the X-ray emission of the 2 Jy objects, we observe trends similar to those observed by Hardcastle et al. (2006, 2009)

[3] For the complete data base, see http://3crr.extragalactic.info/

Table 2. Best-fitting parameters for all the objects in the sample. Errors are calculated at 90 per cent confidence. Where no errors are indicated, the parameters were fixed to that value. Upper limits are indicated with a '<' before the value. When the normalization of one of the powerlaws is an upper limit this component is added after the fit, to assess the contribution of a hypothetical second component. The subindices 1 and 2 refer to the unabsorbed and accretion-related components, respectively. The net (background-subtracted) counts are given for each individual spectrum; thus, for sources observed by *Chandra* only, one value is given (two for the sources with two observations). For those observed by *XMM-Newton*, the three values correspond to the PN, MOS1 and MOS2 spectra, respectively. See Table 1 for details on the individual observations.

PKS	z	Foreground $N_{\rm H}$ ($\times 10^{20}$ cm^{-2})	Intrinsic $N_{\rm H}$ ($\times 10^{22}$ cm^{-2})	Γ_u	Norm 1 (keV^{-1}cm^{-2}s^{-1} @1keV)	Γ_a	Norm 2 (keV^{-1}cm^{-2}s^{-1} @1keV)	Net counts	χ^2/d.o.f.
0023−26	0.322	1.76	$0.16^{+0.11}_{-0.10}$	2.00	$<1.06 \times 10^{-6}$	$1.84^{+0.51}_{-0.19}$	$1.73^{+0.55}_{-0.80} \times 10^{-5}$	336/107/105	20.69/23.00
0034−01	0.073	2.89	$10.07^{+4.84}_{-3.04}$	$1.24^{+0.36}_{-0.34}$	$1.17^{+0.14}_{-0.15} \times 10^{-5}$	1.70	$1.01^{+0.29}_{-0.28} \times 10^{-4}$	490	10.02/20.00
0035−02	0.220	2.85	$3.34^{+1.36}_{-0.97}$	2.00	$1.44^{+0.14}_{-0.13} \times 10^{-4}$	1.70	$2.59^{+0.41}_{-0.43} \times 10^{-4}$	1091	31.12/49.00
0038+09	0.188	5.45	10.00	$0.97^{+0.07}_{-0.07}$	$1.05^{+0.07}_{-0.07} \times 10^{-3}$	1.70	$<4.54 \times 10^{-4}$	1769	84.44/82.00
0039−44	0.346	2.56	$12.40^{+1.82}_{-1.76}$	$2.87^{+0.42}_{-0.18}$	$6.60^{+1.52}_{-1.52} \times 10^{-6}$	$1.39^{+0.09}_{-0.17}$	$1.58^{+0.40}_{-0.51} \times 10^{-4}$	1232/446/423	94.30/92.00
0043−42	0.116	2.70	$13.91^{+5.53}_{-4.08}$	2.00	$2.06^{+0.85}_{-0.86} \times 10^{-6}$	1.70	$1.51^{+0.47}_{-0.40} \times 10^{-4}$	203	6.32/5.00
0105−16	0.400	1.67	$16.13^{+7.34}_{-5.43}$	$1.59^{+0.18}_{-0.20}$	$2.65^{+0.21}_{-0.22} \times 10^{-5}$	$1.50^{+0.41}_{-0.39}$	$1.84^{+2.01}_{-0.40} \times 10^{-4}$	1687/708/661	125.16/137.00
0213−13	0.147	1.89	$18.40^{+4.66}_{-3.40}$	$1.69^{+1.05}_{-1.59}$	$4.62^{+1.23}_{-1.81} \times 10^{-6}$	$1.77^{+0.18}_{-0.22}$	$1.31^{+0.64}_{-0.51} \times 10^{-3}$	1150	45.85/50.00
0235−19	0.620	2.70	0.00	$1.43^{+0.25}_{-0.24}$	$7.30^{+1.07}_{-1.09} \times 10^{-6}$	$1.43^{+0.25}_{-0.24}$	$7.30^{+1.07}_{-1.09} \times 10^{-6}$	146/40/62	10.44/10.00
0252−71	0.566	3.66	$14.90^{+12.67}_{-7.09}$	$2.13^{+0.40}_{-0.33}$	$8.15^{+1.50}_{-2.14} \times 10^{-6}$	1.70	$3.87^{+1.54}_{-1.04} \times 10^{-5}$	373/103/105	20.40/24.00
0347+05	0.339	13.20	$74.85^{+39.25}_{-20.63}$	$1.95^{+0.25}_{-0.25}$	$1.54^{+0.17}_{-0.17} \times 10^{-5}$	1.70	$1.57^{+1.42}_{-0.79} \times 10^{-4}$	352/104/124	16.72/24.00
0349−27	0.066	1.00	$6.40^{+2.00}_{-1.52}$	2.00	$<2.67 \times 10^{-6}$	1.70	$2.55^{+0.49}_{-0.55} \times 10^{-4}$	469	15.98/20.00
0404+03	0.089	12.10	$49.13^{+19.32}_{-15.61}$	2.00	$<1.05 \times 10^{-5}$	1.70	$2.78^{+1.72}_{-1.14} \times 10^{-3}$	226	12.28/8.00
0409−75	0.693	8.71	10.00	$2.02^{+0.06}_{-0.07}$	$8.71^{+0.33}_{-0.35} \times 10^{-5}$	1.70	$<4.64 \times 10^{-6}$	638/527/533	137.62/107.00
0442−28	0.147	2.32	$0.85^{+0.33}_{-0.31}$	2.00	$5.49^{+5.45}_{-5.30} \times 10^{-5}$	$1.13^{+0.24}_{-0.17}$	$1.18^{+0.44}_{-0.30} \times 10^{-3}$	2992	119.53/134.00
0620−52	0.051	5.32	10.00	$2.40^{+0.10}_{-0.10}$	$9.51^{+0.52}_{-0.52} \times 10^{-5}$	1.70	$<1.27 \times 10^{-5}$	1070	39.24/47.00
0625−35	0.055	7.51	$5.99^{+2.56}_{-1.64}$	2.00	$1.11^{+0.09}_{-0.09} \times 10^{-3}$	1.70	$2.74^{+0.57}_{-0.45} \times 10^{-3}$	3940	221.05/173.00
0625−53	0.054	5.51	10.00	2.00	$<1.15 \times 10^{-5}$	1.70	$<8.51 \times 10^{-10}$	20	1.00/1.00
0806−10	0.110	7.65	$21.19^{+8.22}_{-6.18}$	$3.00^{+1.04}_{-1.37}$	$1.08^{+0.34}_{-0.43} \times 10^{-5}$	1.70	$4.63^{+2.33}_{-1.52} \times 10^{-4}$	449	18.17/18.00
0859−25	0.305	10.80	$38.25^{+21.16}_{-23.79}$	$1.61^{+0.41}_{-0.44}$	$9.13^{+1.53}_{-0.84} \times 10^{-6}$	$1.67^{+0.39}_{-0.75}$	$1.81^{+31.00}_{-1.13} \times 10^{-4}$	392/146/122	24.73/24.00
0915−11	0.054	4.94	$2.39^{+1.90}_{-1.35}$	2.00	$<2.11 \times 10^{-6}$	$1.35^{+0.60}_{-0.63}$	$2.49^{+4.58}_{-1.55} \times 10^{-5}$	709/547	71.33/57.00
0945+07	0.086	3.01	$1.44^{+0.20}_{-0.18}$	$3.01^{+0.62}_{-0.57}$	$8.30^{+2.62}_{-2.52} \times 10^{-5}$	$0.73^{+0.09}_{-0.09}$	$1.24^{+0.18}_{-0.14} \times 10^{-3}$	5890/3778	468.26/434.00
1136−13	0.554	3.59	$6.06^{+4.33}_{-2.77}$	$2.00^{+0.09}_{-0.08}$	$3.22^{+0.08}_{-0.14} \times 10^{-4}$	$1.48^{+0.44}_{-0.29}$	$1.38^{+0.22}_{-0.53} \times 10^{-4}$	2970/17514	705.38/619.00
1151−34	0.258	7.70	$52.76^{+52.42}_{-28.83}$	$1.86^{+0.07}_{-0.07}$	$8.02^{+0.26}_{-0.28} \times 10^{-5}$	1.70	$1.28^{+2.40}_{-0.90} \times 10^{-4}$	2190/754/829	160.27/163.00
1306−09	0.464	3.03	$0.11^{+0.04}_{-0.04}$	2.00	$<2.24 \times 10^{-6}$	$1.77^{+0.09}_{-0.09}$	$7.25^{+0.62}_{-0.54} \times 10^{-5}$	2317/823/806	163.12/169.00
1355−41	0.313	5.61	$0.27^{+0.24}_{+0.18}$	2.00	$1.11^{+0.39}_{-0.38} \times 10^{-5}$	1.70	$2.84^{+8.48}_{-2.45} \times 10^{-4}$	33 250/11 524/11 095	843.39/722.00
1547−79	0.483	9.69	$99.28^{+594.53}_{-46.51}$	2.00	$1.60^{+0.18}_{-0.70} \times 10^{-5}$	1.70	$2.51^{+1.86}_{-1.38} \times 10^{-4}$	252/126/83	17.89/18.00
1559+02	0.104	6.42	$6.02^{+3.85}_{-2.89}$	$3.37^{+0.30}_{-0.25}$	$2.12^{+0.22}_{-0.26} \times 10^{-5}$	1.70	$3.26^{+1.32}_{-0.97} \times 10^{-5}$	635	19.22/23.00
1602+01	0.462	6.59	0.00	$1.68^{+0.03}_{-0.03}$	$2.79^{+0.06}_{-0.06} \times 10^{-4}$	$1.68^{+0.03}_{-0.03}$	$2.79^{+0.06}_{-0.06} \times 10^{-4}$	5052/2141/2063	396.19/362.00
1648+05	0.154	6.40	10.00	$0.80^{+1.34}_{-1.61}$	$5.01^{+1.85}_{-1.91} \times 10^{-6}$	1.70	$<1.45 \times 10^{-3}$	31/80/	6.53/4.00
1733−56	0.098	8.89	10.00	$1.54^{+0.05}_{-0.05}$	$1.06^{+0.04}_{-0.04} \times 10^{-3}$	1.70	$<1.67 \times 10^{-4}$	2991	142.22/133.00
1814−63	0.063	7.76	$2.00^{+0.28}_{-0.28}$	2.00	$2.03^{+1.35}_{-1.40} \times 10^{-5}$	$1.26^{+0.18}_{-0.17}$	$1.90^{+0.23}_{-0.25} \times 10^{-3}$	2795	119.13/126.00
1839−48	0.112	5.70	10.00	$1.35^{+0.23}_{-0.22}$	$1.17^{+0.21}_{-0.21} \times 10^{-5}$	1.70	$<8.82 \times 10^{-6}$	183	6.98/8.00

Table 2 – (*Continued.*)

PKS	z	Foreground $N_{\rm H}$ ($\times 10^{20}$ cm^{-2})	Intrinsic $N_{\rm H}$ ($\times 10^{22}$ cm^{-2})	Γ_u	Norm 1 (keV^{-1}cm^{-2}s^{-1} @1keV)	Γ_a	Norm 2 (keV^{-1}cm^{-2}s^{-1} @1keV)	Net counts	χ^2/d.o.f.
1932−46	0.231	5.01	0.00	$1.82^{+0.08}_{-0.07}$	$6.20^{+0.29}_{-0.27} \times 10^{-5}$	$1.82^{+0.08}_{-0.07}$	$6.20^{+0.29}_{-0.27} \times 10^{-5}$	927/366/369	52.79/74.00
1934−63	0.183	6.15	10.00	$1.36^{+0.18}_{-0.18}$	$2.44^{+0.28}_{-0.28} \times 10^{-5}$	1.70	$<1.88 \times 10^{-5}$	348	14.91/15.00
1938−15	0.452	9.66	$0.37^{+0.15}_{-0.12}$	2.00	$4.28^{+0.77}_{-1.89} \times 10^{-5}$	$1.51^{+0.06}_{-0.08}$	$8.92^{+1.00}_{-0.63} \times 10^{-5}$	2549/959/986	189.19/194.00
1949+02	0.059	14.80	$42.69^{+8.26}_{-3.06}$	$2.05^{+0.30}_{-0.29}$	$1.50^{+0.17}_{-0.17} \times 10^{-5}$	$1.41^{+0.10}_{-0.14}$	$1.24^{+0.39}_{-0.49} \times 10^{-3}$	1847	78.24/81.00
1954−55	0.060	4.61	10.00	$0.97^{+0.37}_{-0.38}$	$4.00^{+1.43}_{-1.38} \times 10^{-6}$	1.70	$<7.34 \times 10^{-6}$	82	1.78/2.00
2135−14	0.200	4.73	$18.38^{+11.73}_{-7.97}$	$1.90^{+0.17}_{-0.12}$	$8.26^{+0.39}_{-0.39} \times 10^{-4}$	1.70	$1.79^{+0.68}_{-0.41} \times 10^{-3}$	2225	120.06/96.00
2135−20	0.635	3.38	$64.52^{+44.68}_{-24.56}$	2.00	$4.75^{+0.97}_{-1.01} \times 10^{-6}$	1.70	$4.63^{+4.04}_{-2.60} \times 10^{-5}$	167/31/46	12.24/14.00
2211−17	0.153	2.51	10.00	2.00	$<4.74 \times 10^{-6}$	1.70	$<4.87 \times 10^{-9}$	16	1.00/1.00
2221−02	0.057	5.01	$19.69^{+3.12}_{-1.97}$	$0.82^{+0.26}_{-0.29}$	$5.17^{+0.47}_{-0.50} \times 10^{-5}$	1.70	$2.21^{+0.27}_{-0.17} \times 10^{-3}$	3305	169.28/144.00
2250−41	0.310	1.48	10.00	$1.93^{+1.69}_{-1.16}$	$4.62^{+2.55}_{-2.77} \times 10^{-6}$	1.70	$4.08^{+1640.00}_{-4.08} \times 10^{-8}$	190/61/21	13.49/8.00
2314+03	0.220	5.22	$9.58^{+7.88}_{-4.17}$	$2.16^{+0.21}_{-0.19}$	$1.55^{+0.13}_{-0.17} \times 10^{-5}$	1.70	$3.23^{+1.47}_{-0.79} \times 10^{-5}$	586/195/209	67.19/46.00
2356−61	0.096	2.34	$14.68^{+1.50}_{-1.29}$	$3.08^{+0.57}_{-0.88}$	$8.43^{+2.02}_{-2.15} \times 10^{-6}$	1.70	$9.82^{+0.98}_{-0.92} \times 10^{-4}$	1107	47.84/47.00

Table 3. Objects for which an Fe Kα emission line was detected. Errors are calculated at 90 per cent confidence. Where no errors are quoted, the parameter had to be fixed for the overall model fit. For PKS 1151−34, the line energy had to be fixed after exploring the statistical space with the XSPEC command *steppar*, since the program was not able to automatically find the best fit.

Source name	Rest-frame energy (keV)	Eq. width (keV)
0039−44	$6.32^{+0.68}_{-0.18}$	0.06
0043−42	$6.48^{+0.32}_{-0.05}$	0.88
0105−16	$6.22^{+0.78}_{-0.22}$	0.09
0409−75	$6.68^{+0.09}_{-0.15}$	0.44
0859−25	$6.51^{+0.47}_{-0.10}$	0.28
1151−34	6.34	0.10
1559+02	$6.44^{+0.05}_{-0.05}$	4.00
1814−63	$6.40^{+0.09}_{-0.07}$	0.15
1938−15	$6.51^{+0.07}_{-0.06}$	0.16
2221−02	$6.37^{+0.05}_{-0.05}$	0.17
2356−61	$6.30^{+0.08}_{-0.07}$	0.14

for the 3CRR sources. The luminosity distribution of the sources versus redshift is as expected, with a large number of low-luminosity sources at low z, and mostly brighter objects detected at high z (see Fig. 1). This effect is, at least in part, caused by the detection limits and sample selection criteria, but also by the well-known evolution of the AGN population with redshift.

It is important to keep in mind that the luminosities we derive for the X-ray components may suffer from contamination from each other. This effect is particularly evident in the broad-line and quasar-like objects. In these objects, there is little or no intrinsic absorption to allow us to distinguish both components; thus, we adopt the same value for $L_{\rm X_u}$ and $L_{\rm X_a}$. This effect can be seen in both panels of Figs 1 and 2, where a few BLRGs and QSOs seem to have systematically higher luminosities than the rest of their populations.

These plots show a distinct separation between the different emission-line populations. Low-excitation objects have much lower accretion-related X-ray emission than any of the other groups. This is consistent with the hypothesis in which LERGs lack the traditional radiatively efficient accretion features characteristic of the high-excitation population (see e.g. Hardcastle et al. 2007a). The separation between narrow-line (NLRG) and broad-line (BLRG) objects is more striking in the bottom panel of Fig. 1 due to both the possible contamination by jet emission in broad-line objects and the influence of relativistic beaming, which 'boosts' the soft X-ray emission in objects whose jets are viewed at small inclination angles.

The four LERGs that fall in the NLRG parameter space in the top panel of Fig. 1 (having high, well-constrained $L_{\rm X_a}$) may be, in fact, radiatively efficient objects. 3C 15 (PKS 0034−01) is very luminous and has a relatively well constrained, obscured, hard component (see Appendix A2). Although we do not detect unequivocal signs of a radiatively efficient accretion disc, in the form of an emission Fe Kα line, this could be due to the low statistics, rather than the absence of the line itself. PKS 0043−42 does have an Fe Kα line, and Ramos Almeida et al. (2011b) find IR evidence for a torus (see

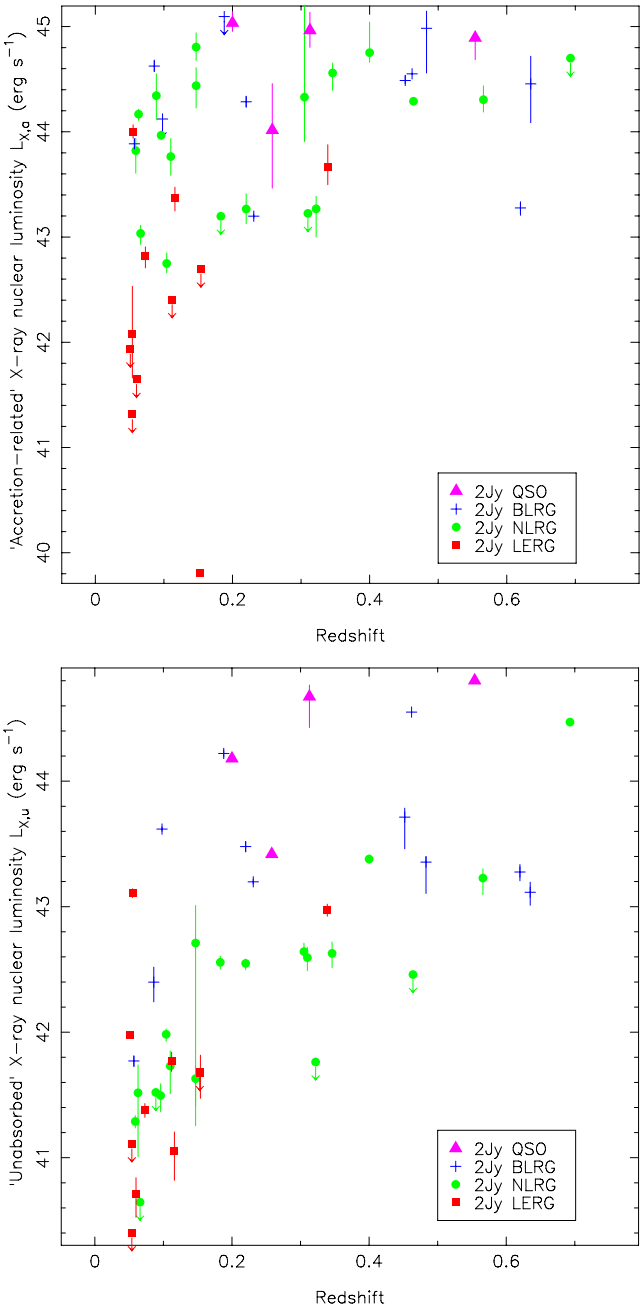

Figure 1. X-ray luminosities for the 2 Jy sources. Top: X-ray luminosity for the accretion-related component L_{X_a} against redshift. Bottom: X-ray luminosity for the unabsorbed component L_{X_u} against redshift. Red squares represent LERGs, green circles NLRGs, blue crosses BLRGs and purple triangles QSOs. Arrows indicate upper limits.

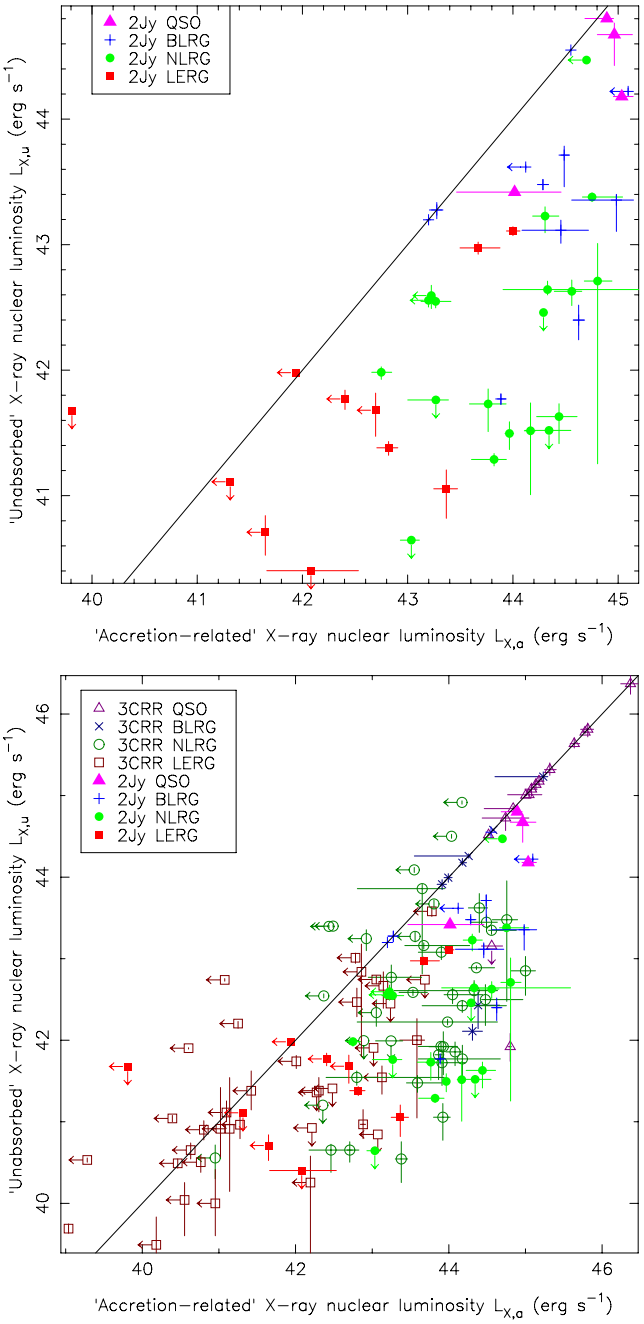

Figure 2. X-ray luminosity for the unabsorbed component L_{X_u} against X-ray luminosity for the 'accretion-related' component L_{X_a}. Top: only the 2 Jy sources are plotted. Bottom: both the 2 Jy and the 3CRR sources are plotted. Arrows indicate upper limits. Colours and symbols as in Fig. 1. A $y = x$ line has been plotted as visual aid for the reader; this line does not represent a correlation.

also Appendix A6). PKS 0625−35 (Appendix A17) is extremely bright and is suspected to be a BL-Lac (Wills et al. 2004). In this case, it is difficult to tell whether there is any contamination from the jet emission on the accretion-related component, causing us to overestimate its luminosity, or whether this object is radiatively efficient in nature.

A special mention should be made of PKS 0347+05. This object was originally classified as a BLRG, but recent evidence suggests that this is, in fact, a double system, with an LERG and a radio-quiet Seyfert 1 in close interaction (see Appendix A11). We have decided to keep this object in our plots and classify it as an LERG based on its optical spectrum (Tadhunter et al. 2012), for consistency with the rest of our analysis, though it is a clear outlier in most of our plots.

The top panel of Fig. 2 shows the distribution of 2 Jy sources according to the relation between their unabsorbed and accretion-related X-ray luminosities. Each population occupies a different area in the parameter space, with a certain degree of overlap between the brighter NLRGs and fainter BLRGs, as can be expected from unification models. For the same reason, there is some overlap

Table 4. Luminosities for the sources in the 2 Jy sample, following the format of Hardcastle et al. (2009). The values are given as the logarithm of the luminosity in erg s^{-1}; upper limits are indicated with a '<' before the value. The columns represent, from left to right, the object name, classification, redshift and luminosities at 178 MHz, 5 GHz (core), soft (jet-related) and hard (accretion-related) X-rays (followed by their respective 90 per cent confidence lower and upper bounds), mid-IR and [O III]. The X-ray accretion-related luminosities have been corrected for intrinsic absorption. We have converted the radio and IR luminosity densities into νL_ν to allow for direct comparison between the magnitudes in different bands. The errors for the radio, IR and [O III] luminosities can be found in the original papers, listed in Section 2.4. Where measurements could not be obtained, their absence is indicated with an en dash. The object types from Table 1 have been abbreviated as follows: E stands for LERG, N for NLRG, B for BLRG and Q for quasar.

PKS	Type	z	L_{178}	L_5	L_{X_u}	$L_{X_u}+$	$L_{X_u}-$	L_{X_a}	$L_{X_a}+$	$L_{X_a}-$	L_{IR}	$L_{[O\,III]}$
0023−26	N	0.322	43.16	–	<41.76	–	–	43.27	43.00	43.39	44.008	42.18
0034−01	E	0.073	41.60	41.25	41.38	41.32	41.43	42.82	42.71	42.91	43.079	40.49
0035−02	B	0.220	42.84	42.55	43.48	43.44	43.52	44.29	44.23	44.34	44.299	42.08
0038+09	B	0.188	42.55	41.54	44.22	44.19	44.25	<45.10	–	–	44.505	42.18
0039−44	N	0.346	43.13	40.65	42.63	42.51	42.72	44.56	44.39	44.66	45.219	43.04
0043−42	E	0.116	42.16	40.97	41.06	40.82	41.21	43.37	43.25	43.47	43.678	40.70
0105−16	N	0.400	43.49	40.61	43.38	43.34	43.41	44.75	44.66	45.04	44.835	42.40
0213−13	N	0.147	42.33	–	41.63	41.41	41.73	44.44	44.23	44.61	43.903	42.11
0235−19	B	0.620	43.88	–	43.28	43.21	43.34	43.28	43.21	43.34	45.350	43.28
0252−71	N	0.566	43.76	–	43.23	43.10	43.30	44.31	44.19	44.44	44.671	42.15
0347+05	B	0.339	42.93	40.33	42.97	42.92	43.02	43.67	43.50	43.88	44.224	40.96
0349−27	N	0.066	41.79	39.80	<40.65	–	–	43.03	42.93	43.11	43.056	41.08
0404+03	N	0.089	41.68	40.10	<41.52	–	–	44.34	44.11	44.55	43.878	41.46
0409−75	N	0.693	44.38	41.27	44.47	44.45	44.49	<44.70	–	–	44.599	42.11
0442−28	N	0.147	42.69	40.98	42.71	41.25	43.01	44.81	44.68	44.94	44.205	41.84
0620−52	E	0.051	41.29	40.89	41.98	41.96	42.00	<41.94	–	–	42.548	<39.41
0625−35	E	0.055	41.18	41.31	43.11	43.07	43.14	44.00	43.94	44.07	43.349	<40.48
0625−53	E	0.054	41.72	40.14	<41.11	–	–	<41.31	–	–	42.173	<40.04
0806−10	N	0.110	42.24	40.89	41.73	41.51	41.85	43.77	43.59	43.94	45.000	42.77
0859−25	N	0.305	43.26	42.08	42.64	42.60	42.71	44.33	43.91	45.59	44.542	41.98
0915−11	E	0.054	42.53	40.89	<40.40	–	–	42.08	41.66	42.53	42.920	40.46
0945+07	B	0.086	42.19	40.44	42.40	42.24	42.52	44.62	44.57	44.68	44.051	41.90
1136−13	Q	0.554	43.60	–	44.80	44.78	44.81	44.89	44.68	44.96	45.326	43.73
1151−34	Q	0.258	42.71	–	43.42	43.40	43.43	44.02	43.46	44.46	44.622	42.45
1306−09	N	0.464	43.14	–	<42.46	–	–	44.29	44.26	44.33	44.664	42.15
1355−41	Q	0.313	42.96	41.65	44.67	44.43	44.77	44.96	44.80	45.14	45.325	42.89
1547−79	B	0.483	43.46	40.95	43.36	43.11	43.40	44.98	44.56	45.15	44.941	43.43
1559+02	N	0.104	42.06	40.55	41.98	41.93	42.03	42.75	42.66	42.85	44.932	42.26
1602+01	B	0.462	43.70	42.25	44.55	44.54	44.56	44.55	44.54	44.56	44.884	42.81
1648+05	E	0.154	43.63	40.41	41.68	41.47	41.82	<42.69	–	–	43.174	40.65
1733−56	B	0.098	41.89	41.88	43.62	43.60	43.64	<44.12	–	–	43.952	41.81
1814−63	N	0.063	42.12	–	41.52	41.01	41.74	44.17	44.11	44.22	43.885	40.63
1839−48	E	0.112	41.97	41.36	41.77	41.69	41.84	<42.40	–	–	43.086	<39.36
1932−46	B	0.231	43.38	41.59	43.20	43.18	43.22	43.20	43.18	43.22	43.696	42.38
1934−63	N	0.183	<43.39	–	42.56	42.50	42.60	<43.20	–	–	44.302	42.08
1938−15	B	0.452	43.52	41.32	43.71	43.46	43.79	44.49	44.46	44.53	44.807	42.88
1949+02	N	0.059	41.55	39.58	41.29	41.24	41.34	43.82	43.61	43.94	44.290	41.86
1954−55	E	0.060	41.57	40.27	40.71	40.53	40.84	<41.65	–	–	42.429	<39.00
2135−14	Q	0.200	42.49	41.76	44.18	44.16	44.20	45.03	44.95	45.14	45.176	43.11
2135−20	B	0.635	43.71	–	43.12	43.01	43.20	44.46	44.09	44.72	45.020	43.15
2211−17	E	0.153	42.86	39.74	<41.68	–	–	<39.81	–	–	42.593	40.38
2221−02	B	0.057	41.74	40.46	41.77	41.73	41.81	43.89	43.85	43.93	44.315	42.23
2250−41	N	0.310	43.22	40.55	42.59	42.49	42.68	<43.22	–	–	44.654	42.70
2314+03	N	0.220	42.99	42.82	42.55	42.50	42.58	43.27	43.13	43.41	44.948	42.20
2356−61	N	0.096	42.64	40.57	41.50	41.37	41.59	43.97	43.92	44.01	44.075	41.95

between the fainter NLRGs and the brighter LERGs. However, it is evident from Fig. 2 that LERGs have a much lower L_{X_a}/L_{X_u} ratio than any of the other populations. The relative faintness of L_{X_a} in LERGs reinforces the conclusions from the previous paragraph about the nature of accretion in LERGs. Adding the 3CRR objects makes this even more evident, as can be seen in the equivalent plot by Hardcastle et al. (2009). As in the top panel of Fig. 1, the four 'efficient' LERGs seem to fall in the parameter space occupied by NLRGs.

4 CORRELATIONS

As described in Section 2.3, from the analysis of the X-ray cores we derived the luminosity of the unabsorbed (L_{X_u}) and accretion-related components (L_{X_a}). For our analysis, we compared these luminosities with those derived from the 178 MHz, 5 GHz (core), 24 μm and [O III] fluxes, all of which are displayed in Table 4. As in the case of the 3CRR objects (Hardcastle et al. 2009), the 2 Jy sample is a flux-limited sample; thus, correlations are expected

Table 5. Results of partial correlation analysis described in Section 4. The number of objects for each correlation is given in column 4, and it includes all the objects in the corresponding subsample given in column 3. The last column indicates the strength of the partial correlation between the quantities in columns 1 and 2 in the presence of redshift. We consider the correlation significant if $\tau/\sigma > 3$.

x	y	Subsample	n	τ	σ	τ/σ
L_{178}	L_{X_u}	2 Jy+3CRR NLRG	106	0.214	0.045	4.726
		2 Jy NLRG	19	0.243	0.141	1.727
L_{178}	L_{X_a}	All	147	0.112	0.028	3.947
		2 Jy+3CRR HERG	99	0.113	0.038	2.969
		2 Jy+3CRR LERG	47	0.013	0.031	0.423
L_5	L_{X_u}	All	137	0.436	0.043	10.043
		2 Jy HERG+LERG	35	0.412	0.091	4.525
		2 Jy+3CRR, QSOs excluded	120	0.379	0.047	8.047
		2 Jy, QSOs excluded	33	0.395	0.102	3.886
L_5	L_{X_a}	All	137	0.252	0.046	5.531
		2 Jy+3CRR, QSOs excluded	120	0.143	0.046	3.090
		2 Jy+3CRR LERG	47	0.146	0.055	2.648
L_{IR}	L_{X_u}	All	117	0.338	0.054	6.297
		2 Jy+3CRR HERG	80	0.243	0.072	3.394
L_{IR}	L_{X_a}	All	117	0.476	0.046	10.440
		2 Jy+3CRR HERG	80	0.384	0.063	6.132
$L_{[O\,III]}$	L_{X_a}	All	122	0.412	0.044	9.319
		2 Jy+3CRR HERG	86	0.323	0.057	5.665
L_{178}	L_{IR}	All	139	0.186	0.036	5.141
		2 Jy+3CRR HERG	102	0.195	0.047	4.172
		2 Jy+3CRR NLRG	59	0.168	0.060	2.782
		2 Jy+3CRR LERG	37	0.093	0.075	1.241
L_{178}	$L_{[O\,III]}$	All	133	0.182	0.034	5.290
		2 Jy+3CRR HERG	96	0.188	0.044	4.242
		2 Jy+3CRR NLRG	53	0.138	0.056	2.474
		2 Jy+3CRR LERG	37	0.113	0.065	1.741
L_{IR}	$L_{[O\,III]}$	All	111	0.586	0.064	9.126
		2 Jy HERG+LERG	45	0.660	0.101	6.504
		2 Jy+3CRR HERG	79	0.514	0.068	7.614
		2 Jy HERG	35	0.579	0.100	5.776
$L_{[O\,III]}$	Q	2 Jy+3CRR HERG	87	0.136	0.048	2.824
		2 Jy+3CRR NLRG	45	0.079	0.064	1.235
L_{IR}	Q	2 Jy+3CRR HERG	87	0.154	0.050	3.063
		2 Jy+3CRR NLRG	45	0.143	0.079	1.813
Q	L_{edd}	All	102	0.274	0.096	2.851
		2 Jy+3CRR HERG	62	0.243	0.148	1.644
		2 Jy+3CRR NLRG	52	0.350	0.183	1.916
		2 Jy+3CRR LERG	40	0.213	0.109	1.955

in luminosity–luminosity plots. We tested for partial correlation in the presence of redshift to account for this, following the method and code described by Akritas & Siebert (1996), which takes into account upper limits in the data. In this method, τ is equivalent to Kendall's τ, and σ represents the dispersion of the data; we therefore consider the τ/σ ratio to assess the significance of the correlation. The results of the partial correlation analysis are given in Table 5. We have only added to the table results that add scientifically relevant information to those presented by Hardcastle et al. (2009), rather than the full analysis.

While the relations between these luminosities can provide some insight into the physical processes going on in each source, it is important to keep in mind that there are several intrinsic effects that limit this insight, orientation, beaming, variability and environmental interference being perhaps the most relevant. These effects are also the most likely cause of scatter in the plots that we present in the following sections. In this paper, we therefore describe the correlations between these luminosities without reference to any particular model, merely attempting to establish the physical scenarios and measurement systematics that may cause these correlations to arise.

To allow direct comparison with the results of Hardcastle et al. (2009), we have plotted both the 2 Jy and the 3CRR objects in our figures. The bottom panel of Fig. 2 summarizes the X-ray characteristics of both populations. In terms of sample size, we have multiwavelength luminosities for 45 2 Jy objects and 135 3CRR sources (although in the latter the data are less complete, see the tables in Appendix B), more than doubling the number of objects studied by Hardcastle et al. (2009).

The differences between the LERGs and HERGs observed in the top panel of Fig. 2 are highlighted by the addition of the 3CRR objects (bottom panel), though it is also clearer that there is an overlap in the parameter space between BLRGs and NLRGs. M87, 3C 326 and 3C 338, originally listed as NLRGs by Hardcastle et al. (2006, 2009), have since been re-classified as LERGs (Buttiglione et al. 2009). The LERG 3C 123 is probably more appropriately

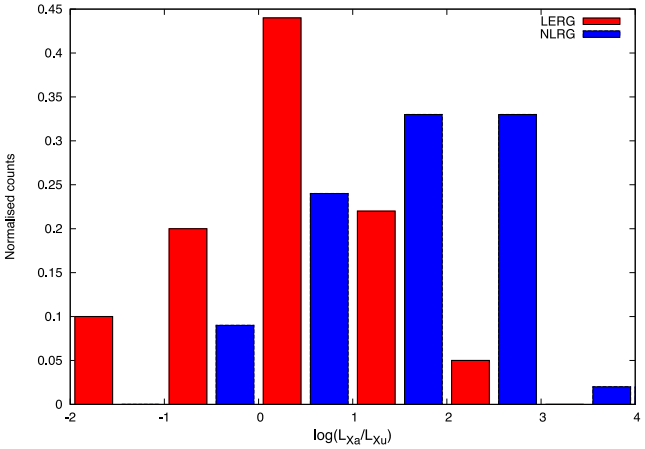

Figure 3. Histogram of the L_{X_a}/L_{X_u} for the 2 Jy and 3CRR LERGs and NLRGs. Broad-line objects are excluded to avoid contamination. The ratios for LERGs are upper limits.

classified as a reddened NLRG, and the X-ray spectrum of 3C 200 is compatible with that of a radiatively efficient AGN, despite its LERG classification (see appendix of Hardcastle et al. 2006).

Fig. 3 shows the ratio between L_{X_a} and L_{X_u} for the 2 Jy and 3CRR LERGs and NLRGs. We have not included the broad-line objects in the plot because, even in the case where both components can be distinguished, contamination from each other and beaming may be an issue. It is quite clear in this plot that NLRGs have a systematically higher L_{X_a}/L_{X_u}, which is even more relevant when we consider the fact that for the vast majority of the LERGs we only have upper limits for L_{X_a}. This histogram already hints at the different nature of accretion and energy output in LERGs and HERGs. To fully separate the accretion-related contribution from the jet component, however, and to interpret these results, further analysis is needed. We address this issue in detail in Section 5.1.

There are also some differences between the 2 Jy and 3CRR populations, which can be partly attributed to the slightly different selection criteria used in both samples, and which may cause the 2 Jy sample to have more beamed objects (as discussed in Section 2.1), as well as issues with sample completeness in the latter sample (the 3CRR sample is nearly complete in X-rays for low-z objects, but not so for $z > 0.5$). While we consider that these effects do not invalidate our results, it is essential to keep in mind that any selection criteria for an AGN sample introduce a certain bias. We will discuss other possible sources of bias in Section 5.

4.1 X-ray/radio correlations

The 178 MHz luminosity is not only an indicator of the time-averaged jet power, but also of the age of the source, and is related to the properties of the external environment (Hardcastle & Krause 2013). By adding the 2 Jy sources to the L_{178}/L_{X_u} plot (top panel of Fig. 4), a correlation between these quantities for the NLRGs is more readily apparent than it was for Hardcastle et al. (2009), despite the scatter, and is significant in the partial correlation analysis (Table 5). Although the 2 Jy objects on their own do not show a significant correlation, the larger number of objects with respect to those of Hardcastle et al. (2009) enhances the significance of the correlation. Because of the fact that the 2 Jy sample is statistically complete, this also allows us to rule out that the results previously obtained for the 3CRR sources are biased, as well as adding to the overall statistics.

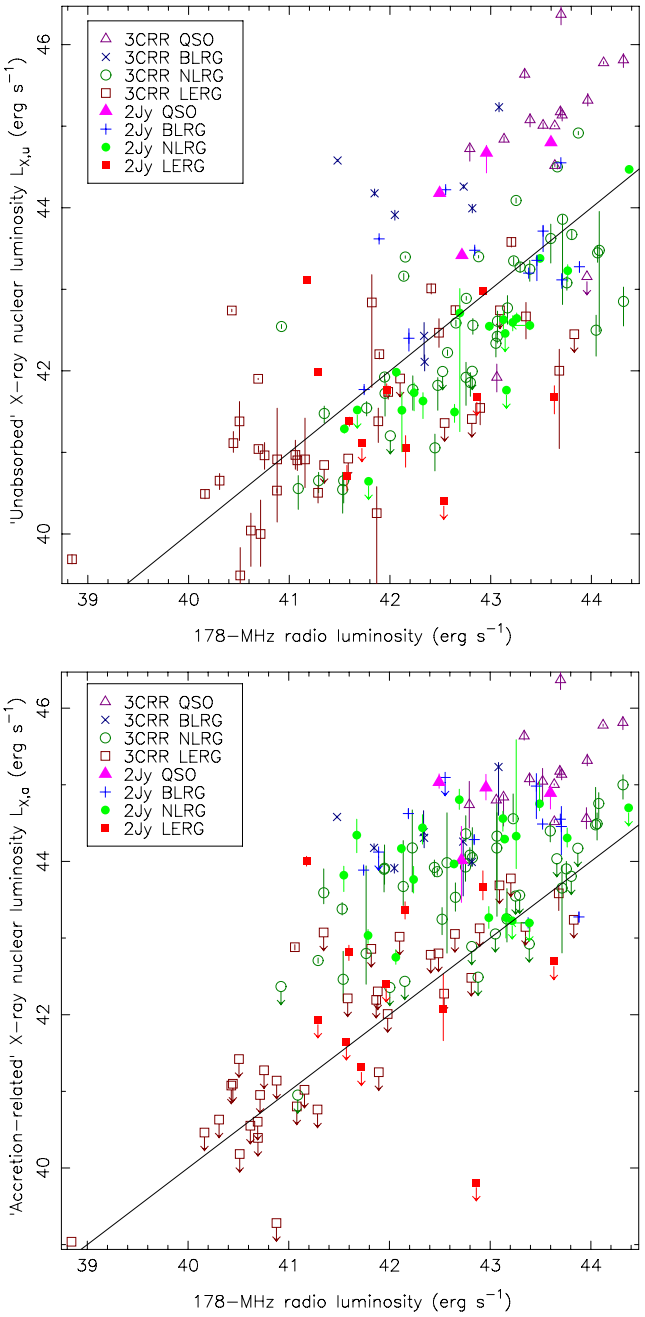

Figure 4. Top: X-ray luminosity for the unabsorbed component L_{X_u} as a function of 178 MHz total radio luminosity. Bottom: X-ray luminosity for the 'accretion-related' component L_{X_a} as a function of the 178 MHz total radio luminosity. Both the 2 Jy and the 3CRR sources are plotted. Arrows indicate upper limits. Colours and symbols as in Fig. 1. Line as in Fig. 2.

The situation is not so clear for the BLRGs and QSOs, most likely due to the contamination from the accretion-related component. In the case of the LERGs, the scatter is expected due to the fact that there are no selection effects on orientation. All of this suggests that there may be a weak physical link between the unabsorbed X-ray power (prior to beaming correction) and the overall radio power (related to the time-averaged AGN power).

There is no apparent correlation between L_{178}/L_{X_u} if only the 2 Jy sources are considered (see Table 5). This is most likely due to the large scatter in the jet-related quantities, and L_{X_u} in particular,

caused by the presence of beamed objects in the 2 Jy sample, a consequence of the selection criteria, as well as the low number of sources. In fact, the value of τ in the L_{178}/L_{X_u} correlation when only the 2 Jy sources are considered is larger than it is for the combined 2 Jy and 3CRR samples, but the scatter (indicated by σ) is much larger in the former case, resulting in $\tau/\sigma < 3$.

By contrast, and as already pointed out by Hardcastle et al. (2009), there seems to be a strong correlation between L_{178}/L_{X_a} for all the populations excluding the LERGs, which seem to lie mostly below the correlation (see the bottom panel of Fig. 4 and Table 5). The BLRGs and QSOs are not clearly outlying in this plot, despite the contamination from the jet-related X-ray component.

The top panel of Fig. 5 shows the relation between the 5 GHz core luminosity and the unabsorbed X-ray component. The correlation between these quantities is strong, despite the scatter, due to the fact that both quantities are subject to beaming. The fact that the LERGs lie in the same correlation as the NLRGs is evidence for the jet-related nature of the soft X-ray component in radio-loud sources (see e.g. Worrall et al. 1987; Hardcastle et al. 2009, and references within). The soft component observed in radio-quiet AGN (either caused by reflection of the hard component on the accretion disc in the radiatively efficient AGN or Comptonization in the radiatively inefficient sources) must still exist in radio-loud objects; in the latter, however, the jet-related emission dominates in the soft X-ray regime.

The bottom panel of Fig. 5 shows the relation between the 5 GHz core luminosity and the accretion-related X-ray component. In this plot, it becomes apparent that the LERGs show a distinct behaviour, completely apart from the high-excitation population, and consistent with the hypothesis that these objects have a different accretion mechanism. The correlation between these two quantities is less strong than between $L_{5\,\mathrm{GHz,\,core}}$ and L_{X_u} (Table 5), and all but disappears if the QSOs are removed.

Correlations between both X-ray luminosities and the 5 GHz radio core luminosity are expected due to their mutual dependence on redshift. If the X-ray luminosity were simply related to the time-averaged AGN power, and independent from orientation and beaming, it would not be strongly correlated to the 5 GHz core luminosity (although there is a jet–disc connection relating both quantities, the scatter is larger than for purely jet-related components, weakening the correlation; see also Section 5.3). As argued by e.g. Hardcastle & Worrall (1999), Doppler beaming can introduce up to three orders of magnitude of scatter in these correlations, given its strong influence on $L_{5\,\mathrm{GHz,\,core}}$. The correlation we observe between $L_{5\,\mathrm{GHz,\,core}}$ and L_{X_u}, in particular, reinforces the hypothesis that the soft X-ray flux is related to jet emission in radio-loud sources.

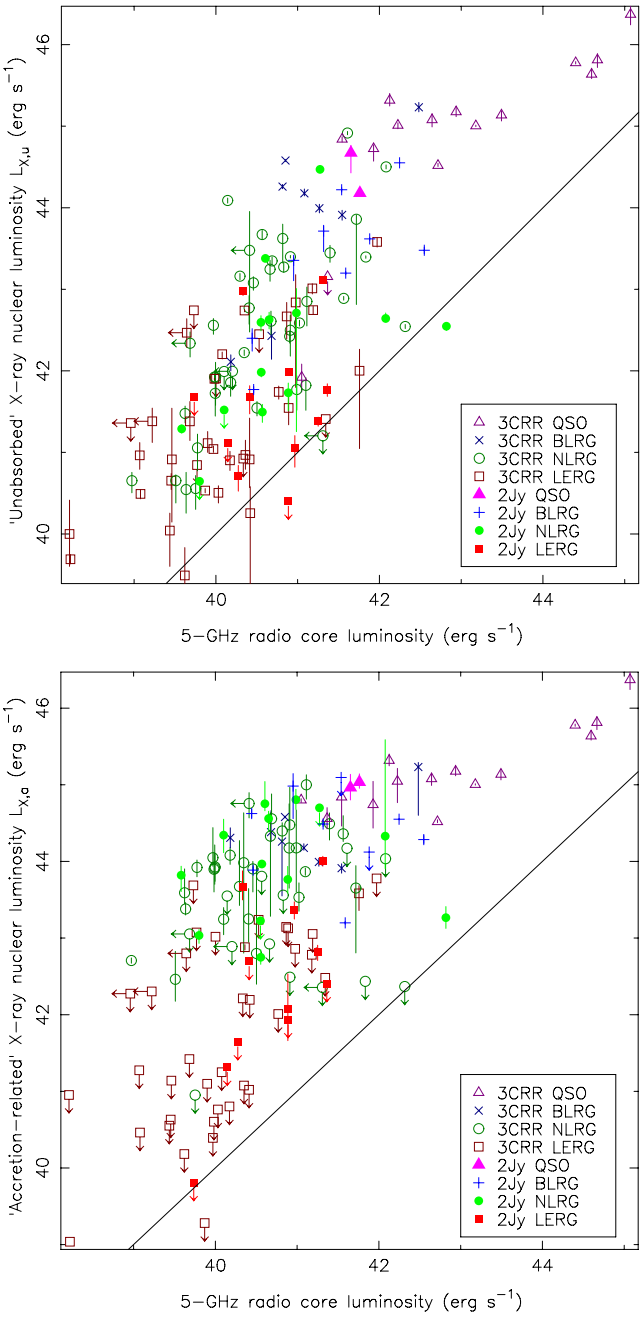

Figure 5. Top: X-ray luminosity for the unabsorbed component L_{X_u} as a function of 5 GHz radio core luminosity. Bottom: X-ray luminosity for the 'accretion-related' component L_{X_a} as a function of the 5 GHz radio core luminosity. Both the 2 Jy and the 3CRR sources are plotted. Arrows indicate upper limits. Colours and symbols as in Fig. 1. Line as in Fig. 2.

4.2 X-ray/IR correlations

The main source of uncertainty in L_{IR} comes from the dependence with the orientation of the dusty torus, which is believed to introduce a large uncertainty (see e.g. Hardcastle, Evans & Croston 2009; Runnoe, Brotherton & Shang 2012, and references therein). It is possible that some of the broad-line objects have some contamination from non-thermal (synchrotron) emission from the jet, although the dominant contribution to the mid-IR is dust-reprocessed emission from the torus. We discuss this point further later in this section.

Despite the large scatter, there is an evident overall correlation between L_{IR} and L_{X_u} (top panel of Fig. 6), which was already visible in the plots of Hardcastle et al. (2009) (see Table 5). The 2 Jy sources fill some of the gaps left by the 3CRR sources in the parameter space. The correlation disappears for individual populations, however. In the broad-line objects, it is possible that L_{X_u} is affected by beaming.

The correlation between L_{IR} and L_{X_a} is very strong (bottom panel of Fig. 6 and Table 5). The correlation is expected, since both luminosities are indicators of the overall power of the accretion disc. Some of the scatter in this correlation is likely to come from the fact that L_{IR} is more dependent on orientation than L_{X_a} and the way in which the latter is affected by obscuration (objects with a much larger L_{IR} than L_{X_a} are likely to be Compton thick). The correlation between L_{IR} and L_{X_a} holds for radio-quiet objects at all

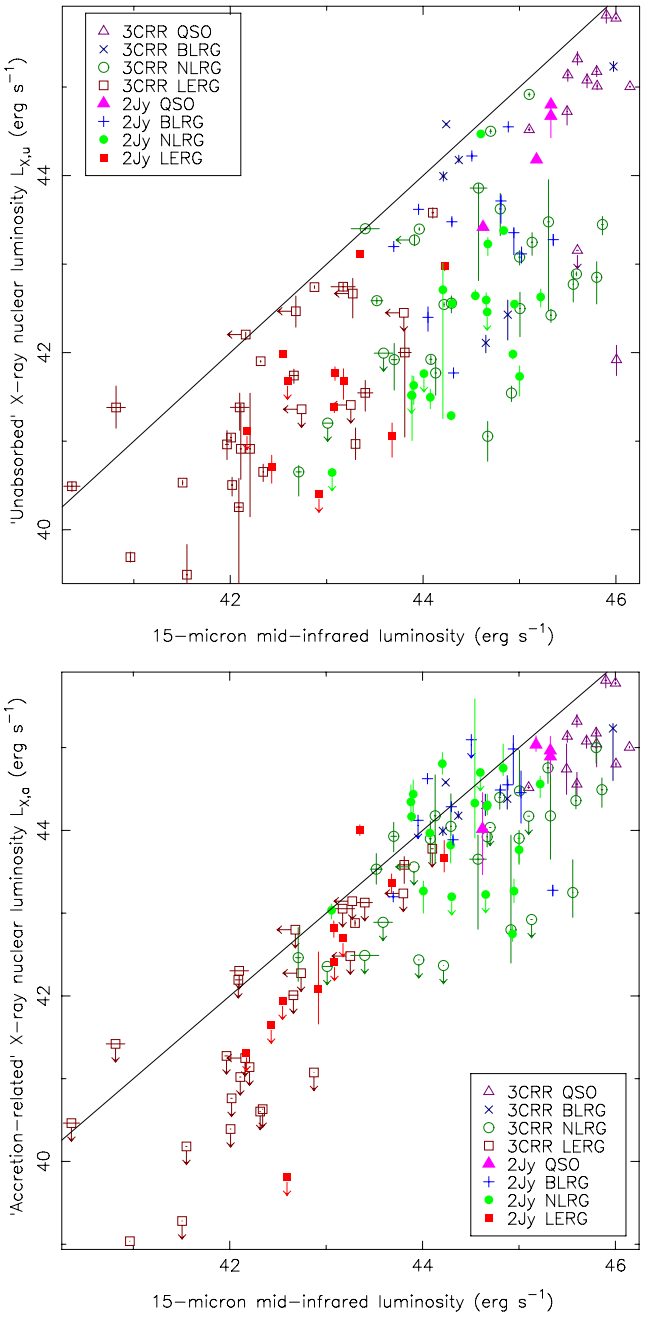

Figure 6. Top: X-ray luminosity for the unabsorbed component L_{X_u} as a function of the total IR (24 μm for the 2 Jy sources, 15 μm for the 3CRR sources) luminosity. Bottom: X-ray luminosity for the 'accretion-related' component L_{X_a} as a function of the total IR (24 μm for the 2 Jy sources, 15 μm for the 3CRR sources) luminosity. Both the 2 Jy and the 3CRR sources are plotted. Arrows indicate upper limits. Colours and symbols as in Fig. 1. Line as in Fig. 2.

orientations (see e.g. the results of Gandhi et al. 2009; Asmus et al. 2011, on local Seyferts), which suggests that non-thermal emission from the jet is either not affecting the quantities involved in the correlation or is equally boosting both, as may be the case for some of the broad-line objects with strong radio cores in our sample.

Some of the NLRGs in our sample are quite heavily obscured, and we could only constrain an upper limit to their absorption column and accretion-related X-ray luminosity. These objects are probably Compton thick, and lie to the lower right of the correlation in this plot. The most extreme example of such behaviour is PKS 2250−41. PKS 1559+02 shows the largest departure from the correlation among the NLRGs, having a very small L_{X_a} component when compared to L_{IR}, and is probably Compton thick. The BLRG PKS 0235−19 is also very underluminous in X-rays, and a clear outlier in the bottom panel of Fig. 6, which is not expected for a broad-line object.

The behaviour of the LERGs in this figure is most significant, reinforcing the idea that LERGs cannot be explained as heavily obscured, 'traditional', radiatively efficient AGN. LERGs are underluminous in X-rays, and lie below the correlation for HERGs. Adding an intrinsic absorption column $N_H = 10^{24}$ cm^{-2} is still insufficient to boost the X-ray luminosity of most of these objects enough to situate them on the correlation. The overlap between the populations happens mostly for objects whose emission-line classification is inconsistent with our best estimate of the accretion mode (the radiatively efficient LERGs mentioned in Section 3), and because of the large scatter caused by systematics.

The origin of the IR emission in 'inefficient' LERGs should be questioned. We know from the cases like M87 that no accretion-related component is detected on small scales (see section 4.1 in Hardcastle et al. 2009), although IR emission is measured with *Spitzer*. It is very likely that in these LERGs, the IR emission is associated with the jet and the old stellar population, and is therefore not reliable as an estimator of accretion.

4.3 X-ray/[O III] correlations

The relation between the [O III] and jet-related X-ray luminosity is shown in the top panel of Fig. 7. This plot is surprising in that it separates the populations quite clearly. This separation is not expected a priori, since [O III] traces the photoionizing power of the AGN, which is directly related to accretion and not directly dependent on jet power, which is traced by L_{X_u}. The NLRG PKS 0409−75 is an outlier in the plot, having a much higher L_{X_u} ($>10^{44}$ erg s^{-1}) than is expected from its $L_{[O\,III]}$. As detailed in Sections 2.3 and A14, it is possible that the soft X-ray component in this source suffers from contamination from inverse-Compton emission from the radio lobes, since this object is in a dense environment.

The LERGs are underluminous in [O III], as expected, and show a great deal of scatter due to the effect of the random orientation on their X-ray emission. Broad-line objects have boosted X-ray luminosities both due to beaming and due to contamination from the accretion-related component, and lie towards the top-right corner of the plot. The relative faintness in [O III] of some objects can be explained by obscuration, as suggested by Jackson & Browne (1990). Obscuration, and the presence or absence of contamination from the accretion-related component in some broad-line objects, introduces scatter in this plot, and separates the BLRGs and QSOs from the NLRGs.

As pointed out by Hardcastle et al. (2009), there is a strong correlation between $L_{[O\,III]}$ and L_{X_a} (Table 5 and the bottom panel of Fig. 7), given that both quantities directly trace accretion (see also Dicken et al. 2009, and Dicken et al. 2014, submitted). As in the case of the correlation between L_{IR} and L_{X_a}, the LERGs fall below the correlation expected for high-excitation objects (excepting the few 'efficient' LERGs mentioned before). The scatter in this plot is much higher than that seen in the bottom panel of Fig. 6. IR emission is a better indicator of accretion than [O III], since it is less contaminated by the jet and stellar processes, as well as easier to measure (see also e.g. Dicken et al. 2009).

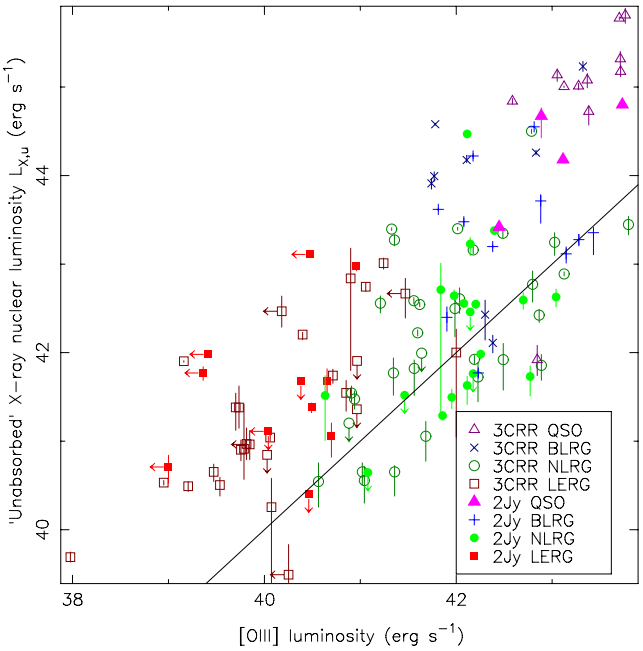

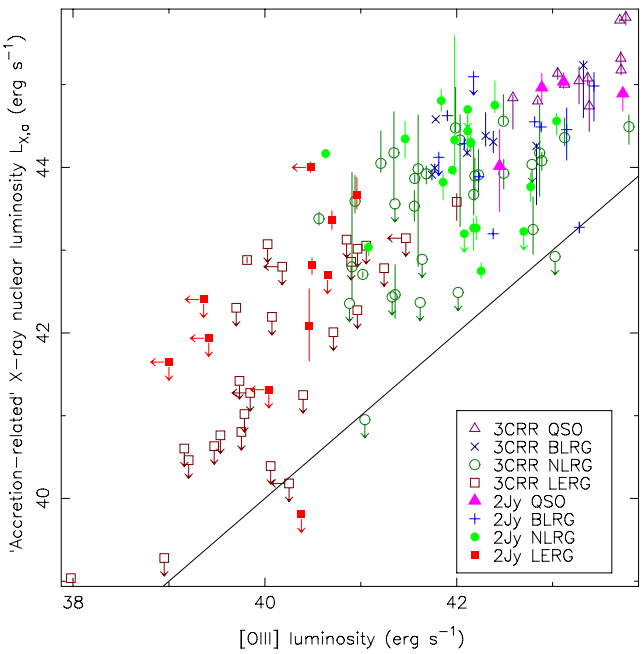

Figure 7. Top: X-ray luminosity for the unabsorbed component L_{X_u} against the [O III] emission-line luminosity. Bottom: X-ray luminosity for the 'accretion-related' component L_{X_a} against the [O III] emission-line luminosity. Both the 2 Jy and the 3CRR sources are plotted. Arrows indicate upper limits. Colours and symbols as in Fig. 1. Line as in Fig. 2.

As for the case of the bottom panel of Fig. 6, PKS 1559+02 and PKS 2250−41 also fall below the correlation in the bottom panel of Fig. 7, reinforcing the hypothesis that these objects are Compton thick. PKS 0235+05 is also an outlier in this plot, with a much lower L_{X_a} than is expected for a BLRG.

4.4 Radio/IR/[O III] correlations

Hardcastle et al. (2009) found correlations between the overall radio luminosity and the IR and [O III] luminosities. We observe the same in our plots and correlation analysis (Figs 8 and 9, and Table 5),

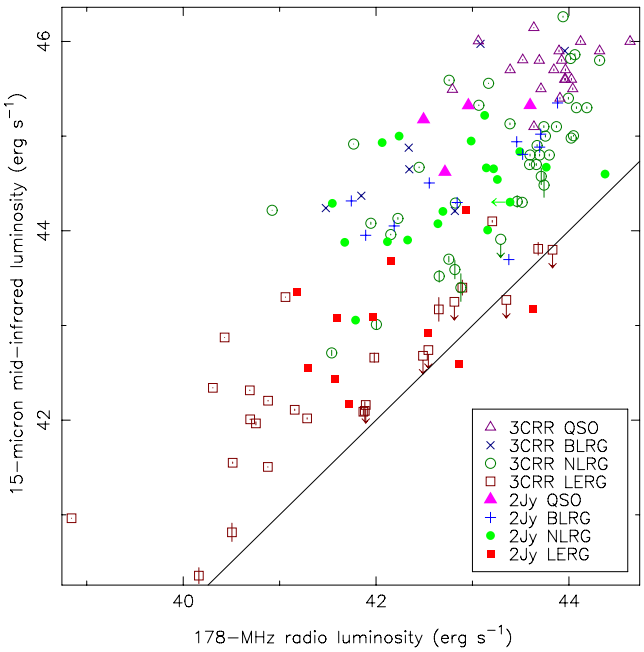

Figure 8. Total IR (24 μm for the 2 Jy sources, 15 μm for the 3C sources) luminosity against the 178 MHz total radio luminosity. Arrows indicate upper limits. Colours and symbols as in Fig. 1. Line as in Fig. 2.

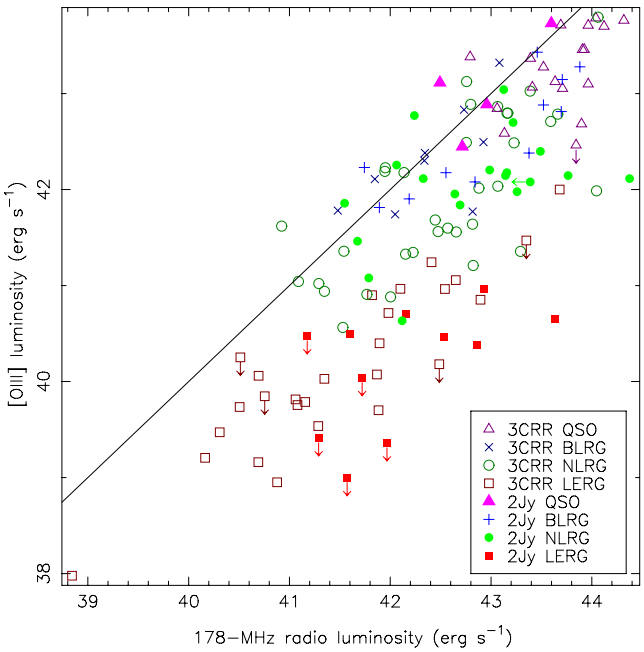

Figure 9. [O III] emission-line luminosity against the 178 MHz total radio luminosity. Arrows indicate upper limits. Colours and symbols as in Fig. 1. Line as in Fig. 2.

with the 2 Jy sources filling some of the gaps in the parameter space. The LERGs have higher (relative) radio luminosities than the other populations, as expected. Beaming is likely to introduce scatter in the radio luminosity in both plots, while orientation is likely to influence the scatter in IR luminosities. For the 3CRR objects, it can be seen that the broad-line objects have systematically higher [O III] luminosities than narrow-line objects for the same luminosity (see figs 9 and 11 of Hardcastle et al. 2009), but the situation is not so clear for the 2 Jy sources alone, due to their redshift distribution.

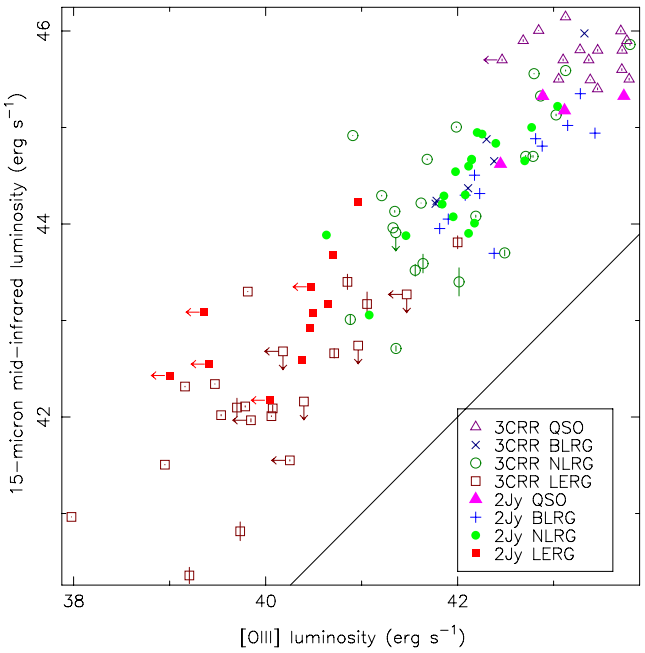

Figure 10. Total IR (24 μm for the 2 Jy sources, 15 μm for the 3C sources) luminosity against the [O III] emission-line luminosity. Arrows indicate upper limits. Colours and symbols as in Fig. 1. Line as in Fig. 2.

By contrast, and as observed by Hardcastle et al. (2009), the radio core luminosity is not well correlated with either $L_{\rm IR}$ or $L_{[\rm O\,III]}$. The QSOs have radio cores that are far more luminous than those of the other classes. All the populations, in fact, seem to be in different regions of the parameter space, with the broad-line objects having more luminous radio cores than the narrow-line objects for the same $L_{\rm IR}$ and $L_{[\rm O\,III]}$ due to beaming, and LERGs being fainter in both plots, but also more radio luminous, in proportion, than NLRGs.

The correlation between $L_{\rm IR}$ and $L_{[\rm O\,III]}$ is very strong (Fig. 10 and Table 5), and made much clearer by the addition of the 2 Jy objects. The recent results of Dicken et al. (2014, submitted) suggest that both quantities are affected to the same degree by orientation/extinction effects. Moreover, neither quantity is likely to be affected by beaming (unless non-thermal contamination is substantial), which greatly reduces the scatter. Contamination from the jet is also likely to favour both quantities, mostly the IR emission, by the addition of a non-thermal component, but if shock ionization is involved [O III] emission may be boosted as well. Although the contributions from either mechanism are likely to be very different, and change for individual objects, they must be kept in mind. While expected, it is interesting to note that the scatter is much smaller when considering $L_{\rm IR}$ and $L_{[\rm O\,III]}$, rather than the X-ray luminosities, where variability is much larger due to the shorter time-scales involved.

5 JET POWER AND EDDINGTON RATES

One of the hypotheses that have gained more strength in recent years over the mechanisms underlying accretion in LERGs postulates that there is an accretion rate switch between these objects and the high-excitation population at about 1–10 per cent of the Eddington rate (see e.g. Best & Heckman 2012; Russell et al. 2013, and references therein). In this section, we aim to test this hypothesis, taking into account not just the radiative power from the AGN, but also the kinetic power of the jet, denoted by Q throughout this section, after the definition of Willott et al. (1999).

5.1 Jet power estimations

To estimate the jet kinetic power, we considered two possible correlations: that of Cavagnolo et al. (2010), which relies on 1.4- GHz measurements, and of Willott et al. (1999), which is derived from 151 MHz fluxes, with a correction factor $f = 15$ (see discussion in Hardcastle et al. 2009). Cavagnolo et al. (2010) derived their correlation from X-ray cavity measurements; this method, as pointed out by Russell et al. (2013), is subject to uncertainties in the volume estimations and on how much of the accretion-derived AGN power is actually transferred to the interstellar medium/IGM. Given that the objects in our samples are far more powerful than the ones considered by Cavagnolo et al. (2010), it is possible that their correlation underestimates the jet powers in our case, but it is the best estimate based on actual data. Willott et al. (1999) derived their correlation from minimum energy synchrotron estimates and [O II] emission-line measurements, which make the slope of the correlation somewhat uncertain, as well as introducing an additional uncertainty (in form of the factor f) in the normalization.

As suggested by Croston et al. (2008), the particle content and energy distributions in FR I and FR II systems are probably very different (but see also Godfrey & Shabala 2013), and we know that there is a dependence of the jet luminosity with the environment (jets are more luminous in denser environments; see e.g. Hardcastle & Krause 2013); it is very likely that, a priori, a single correlation cannot be used across the entire population of radio-loud objects. However, Godfrey & Shabala find that such a correlation does work, and conclude that environmental factors and spectral ageing 'conspire' to reduce the radiative efficiency of FR II sources, effectively situating them on the same $Q_{\rm jet}-L_{151}$ correlation as the low-power FR I galaxies. This effect makes the use of these correlations qualitatively inaccurate, but quantitatively correct, within the assumptions, as approximations to the jet kinetic power.

We have repeated the luminosity versus jet power plots of Godfrey & Shabala (2013) for our sources, using both the Cavagnolo et al. (2010) and Willott et al. (1999) correlations, and we find them to agree very well, with slight divergences at the high and low ends of the distribution due to the different shapes of both correlations. For our analysis, we have used the relation of Willott et al. (1999), both for consistency with the analysis of Hardcastle et al. (2006, 2009) and because of the relatively higher reliability of low-frequency measurements. As a further check, we have compared the jet power we obtained for PKS 2211−17 with that obtained independently by Croston et al. (2011), and have found them to agree within the uncertainties.

We thus derive the jet kinetic power, Q, from the relation shown in equation 12 of Willott et al. (1999):

$$Q = 3 \times 10^{38} L_{151}^{6/7}\,\mathrm{W}, \qquad (1)$$

where L_{151} is the luminosity at 151 MHz, in units of 10^{28} W Hz^{-1} sr^{-1}.

5.2 Black hole masses, bolometric corrections and Eddington rates

We calculated the black hole masses for the objects in our sample from the K_s-band magnitudes of Inskip et al. (2010) and a slight variation of the well-known correlation between these quantities and the black hole mass (Graham 2007). We cross-tested the results

with the black hole masses obtained from the r'-band magnitudes of Ramos Almeida et al. (2011a) [using the conversions to the B band and the corrections of Fukugita, Shimasaku & Ichikawa (1995)] and the relations from Graham (2007), and found them to be mostly consistent, save for an overall effect that might be related to the different apertures used (the B-band-derived masses tend to be smaller).

15 of our objects are missing from the work of Inskip et al. (2010). We obtained 2MASS magnitudes for some of them, so 11 sources do not have K-band measurements and are thus missing from the following tables and plots. Of these, three are QSOs, four BLRGs, three NLRGs and one LERG. Given that the black hole masses derived from K-band magnitudes for broad-line objects and QSOs are not reliable, we can assume that our sample is adequately covered. A further source of uncertainty for the $M_{\rm BH}$–L_K correlation originates from the fact that black hole masses in clusters are expected to be systematically higher (see e.g. Volonteri & Ciotti 2013). This is particularly important for LERGs inhabiting rich environments, a point we return to in the next section.

When cross-checking United Kingdom Infrared Telescope and 2MASS observations for the 3CRR sources, we found five objects where differences greater than 0.4 mag (after aperture and K-corrections) were present between both instruments. After checking these discrepancies carefully, we have relied on 2MASS measurements whenever possible. It is important to keep in mind not only the limitations of the available data, but also the large degree of scatter present in the correlation of Graham (2007).

The black hole masses for the 2 Jy and 3CRR sources are given in Tables 6 and B2, respectively. We have plotted the histogram distribution of black hole masses in Fig. 11, to illustrate the range of masses covered and to investigate any systematic differences between LERGs and HERGs. We can see that the NLRGs tend to have slightly larger $M_{\rm BH}$ than the LERGs, though there is no clear cut between the two populations. As mentioned earlier, this could be partly due to observational biases, and the fact that we are probably underestimating black hole masses for systems embedded in rich clusters, where most of the LERGs lie. The range of black hole masses could be contributing to the scatter in our plots.

We derived the bolometric luminosity from the different bands, and studied their consistency. We used the correlations of Marconi et al. (2004, equation 21) for the X-ray 2–10 keV luminosity ($L_{\rm X_a}$):

$$\log(L/L_{2-10\,\rm keV}) = 1.54 + 0.24\mathcal{L} + 0.012\mathcal{L}^2 - 0.0015\mathcal{L}^3, \qquad (2)$$

where $\mathcal{L} = (\log(L) - 12)$ and L is the bolometric luminosity in units of $\rm L_\odot$. We used the simple relation of Heckman et al. (2004) for the [O III] luminosity ($L_{\rm bol} = 3500L_{\rm [O\,III]}$) and the relation of Runnoe et al. (2012, equation 8) for the IR luminosity at 24 μm:

$$\log(L_{\rm iso}) = (15.035 \pm 4.766) + (0.688 \pm 0.106)\log(\lambda L_\lambda), \qquad (3)$$

where $L_{\rm iso}$ assumes an isotropic bolometric luminosity (Runnoe et al. recommend that a correction be made to account for orientation effects, so that $L_{\rm bol} \sim 0.75L_{\rm iso}$, but we do not apply this correction). These bolometric luminosities obtained for the different bands are shown in Table 6.

It is worth noting that all these relations are a subject of debate. The $L_{\rm X,2-10\,keV}$–$L_{\rm bol}$ relation was initially postulated for bright quasars (Elvis et al. 1994), and although more complex relations such as that of Marconi et al. (2004) agree with the initial results, they cannot be fully applied to low-luminosity and low-excitation sources (see e.g. Ho 2009). The mid-IR luminosity seems to be a very reliable estimator of the bolometric luminosity of an AGN, despite issues with non-thermal contamination where a jet is present (see e.g. Fernández-Ontiveros et al. 2012), and a minor contribution from star formation. The main issue with this correlation lies in the dependence on orientation, which can introduce a bias of up to 40 per cent (see e.g. Runnoe et al. 2012). [O III] has been widely used to assess the bolometric luminosity, given that the conversion factor between the two is just a constant, but it is not reliable when there are other sources of photoionization; it is known to underestimate the bolometric luminosity in low-excitation sources (see e.g. Netzer 2009), and is also orientation dependent (Jackson & Browne 1990; Dicken et al. 2009).

Jet power versus radiative luminosity plots can be enlightening in discerning the relative contributions of both components for each population. The top panel of Fig. 12 shows $L_{\rm bol,\,[X]}/L_{\rm Edd}$ versus $Q/L_{\rm Edd}$ for the 2 Jy and the 3CRR sources, where Q is the jet power as defined by Willott et al. (1999). The middle and bottom panels of Fig. 12 show the same plot for [O III] and IR-derived bolometric luminosities, respectively. The latter panel of Fig. 12 is the one with the best correlation (see Table 5). Reassuringly, in all the plots adding the contributions from the radiative output and the jet kinetic energy still results in sub-Eddington accretion, even in the brightest sources.

The X-ray-derived Eddington rates show the greatest degree of uncertainty on individual measurements, two orders of magnitude for some sources, and even higher for the ('inefficient') LERGs. The top panel of Fig. 12 illustrates this fact clearly: the X-ray-derived $L_{\rm bol}/L_{\rm Edd}$ spans two orders of magnitude more than that derived from the [O III] and IR measurements (middle and bottom panels). This effect is most likely intrinsic to the nature of X-ray measurements of AGNs, where source variability, intrinsic absorption and beaming contribute to the scatter. LERGs seem to have systematically lower (by over three orders of magnitude in some cases) radiative Eddington rates in X-rays than they do when these rates are derived from IR or [O III] measurements. Even assuming a much higher obscuration ($N_{\rm H} = 10^{24}$ cm^{-2}), their radiative Eddington rates would be far lower than those of the HERGs, which makes it unlikely that LERGs are simply Compton-thick HERGs.

Estimating $L/L_{\rm Edd}$ is very challenging, particularly for radiatively inefficient sources, where models predict very little radiative emission. Can we, therefore, find a reliable probe for the accretion-related, radiative luminosity in LERGs? While IR measurements are most reliable to determine accretion in high-excitation sources, they appear to overestimate this component in LERGs. Most IR points in Fig. 12 are detections, not upper limits, which is not consistent with the model predictions. As pointed out in Section 4.3, it is likely that in these objects the IR emission is associated with the jet and the old stellar population, rather than accretion. For the same reason, [O III] measurements are also likely to be an overestimation, since shock ionization by the jet can boost such emission. We conclude that for LERGs the Eddington rate is best derived from X-ray measurements, since we know that, once the possible contamination by $L_{\rm X_u}$ is accounted for, any remaining radiative output must come from $L_{\rm X_a}$.

In all these plots, a division between high- and low-excitation sources is clearly visible. A trend between jet power and radiative luminosity can be observed for the LERGs. We can assume that a certain degree of contamination from jet emission is present in the radiative component in the three plots, and is probably causing this apparent trend.

Finally, we note that for the HERGs we do not see a decrease in jet power at high radiative luminosities, which indicates that, even if there is a switch between radiatively inefficient and efficient accretion (discussed below, Section 5.4), jet generation is not switched

Table 6. *K*-band magnitudes, *K*-corrections (calculated using the relations of Glazebrook et al. 1995; Mannucci et al. 2001), absolute magnitudes, black hole masses, Eddington luminosities, X-ray, [O III] and IR-derived Eddington ratios and jet Eddington ratios for the sources in the 2 Jy sample. The *K*-band magnitudes from Inskip et al. (2010) are marked as I10 in the reference column; the magnitudes taken directly from the 2MASS catalogue are marked as 2M. The errors quoted for $L_{\rm X,rad}/L_{\rm X,Edd}$ are derived from both the errors in the X-ray power-law normalization and the errors in the intrinsic $N_{\rm H}$, to show the maximum possible uncertainty. Where $N_{\rm H}$ was fixed to 10^{23} cm^{-2}, the upper and lower values of the X-ray luminosity were calculated for $N_{\rm H} = 0$ and 10^{24} cm^{-2}, respectively. E stands for LERG, N for NLRG, B for BLRG and Q for quasar.

PKS	Type	Ref	z	mag K_s	K-corr	Mag K_s	$M_{\rm BH}$ ($\times10^9$ M$_\odot$)	$L_{\rm Edd}$ ($\times10^{40}$ W)	$L_{\rm X,rad}/L_{\rm X,Edd}$	$L_{\rm [O\,III],rad}/L_{\rm [O\,III],Edd}$	$L_{\rm IR,rad}/L_{\rm IR,Edd}$	$Q/L_{\rm Edd}$
0023−26	N	I10	0.322	15.036	−0.604	−26.70	1.67	2.17	$1.76^{+0.10}_{-0.11}\times10^{-3}$	2.42×10^{-2}	1.15×10^{-2}	9.10×10^{-2}
0034−01	E	I10	0.073	12.569	−0.183	−25.21	0.53	0.69	$1.50^{+0.28}_{-0.28}\times10^{-3}$	1.56×10^{-3}	8.28×10^{-3}	1.23×10^{-2}
0035−02	B	I10	0.220	14.107	−0.482	−26.47	1.40	1.81	$4.41^{+0.54}_{-0.47}\times10^{-2}$	2.32×10^{-2}	2.17×10^{-2}	5.25×10^{-2}
0038+09	B	I10	0.188	14.299	−0.428	−25.94	0.93	1.21	$8.14^{+0.08}_{-0.56}\times10^{-1}$	4.34×10^{-2}	4.57×10^{-2}	4.82×10^{-2}
0039−44	N	I10	0.346	15.411	−0.622	−26.53	1.46	1.89	$9.81^{+1.97}_{-1.84}\times10^{-2}$	2.03×10^{-1}	8.99×10^{-2}	9.79×10^{-2}
0043−42	E	I10	0.116	12.999	−0.283	−25.94	0.94	1.22	$4.18^{+0.82}_{-0.65}\times10^{-3}$	1.44×10^{-3}	1.22×10^{-2}	2.29×10^{-2}
0105−16	N	I10	0.400	15.419	−0.649	−26.91	1.96	2.55	$1.33^{+0.64}_{-0.39}\times10^{-1}$	3.44×10^{-2}	3.64×10^{-2}	1.38×10^{-1}
0213−13	N	I10	0.147	13.502	−0.349	−26.07	1.03	1.33	$9.57^{+3.05}_{-2.85}\times10^{-2}$	3.41×10^{-2}	1.59×10^{-2}	2.98×10^{-2}
0347+05	B	I10	0.339	14.286	−0.617	−27.59	3.28	4.27	$2.31^{+1.66}_{-0.66}\times10^{-2}$	7.46×10^{-4}	8.21×10^{-3}	2.72×10^{-2}
0349−27	E	I10	0.066	12.853	−0.166	−24.68	0.36	0.46	$4.16^{+0.56}_{-0.55}\times10^{-3}$	9.04×10^{-3}	1.20×10^{-2}	1.23×10^{-2}
0404+03	N	I10	0.089	13.417	−0.221	−24.85	0.41	0.53	$1.80^{+0.83}_{-0.62}\times10^{-1}$	1.91×10^{-2}	3.84×10^{-2}	1.88×10^{-2}
0442−28	N	I10	0.147	13.160	−0.349	−26.41	1.33	1.73	$2.30^{+0.10}_{-0.09}\times10^{-1}$	1.40×10^{-2}	1.96×10^{-2}	3.52×10^{-2}
0620−52	E	2M	0.051	9.801	−0.129	−27.11	2.27	2.95	$3.06^{+9.80}_{-3.06}\times10^{-5}$	3.09×10^{-5}	8.18×10^{-4}	1.09×10^{-3}
0625−35	E	I10	0.055	10.724	−0.139	−26.36	1.29	1.68	$2.00^{+0.23}_{-0.18}\times10^{-2}$	6.27×10^{-4}	5.19×10^{-3}	2.13×10^{-3}
0625−53	E	I10	0.054	10.042	−0.137	−27.00	2.09	2.72	$6.41^{+0.02}_{-6.41}\times10^{-6}$	1.41×10^{-4}	4.91×10^{-4}	4.24×10^{-3}
0806−10	N	I10	0.110	12.137	−0.269	−26.67	1.62	2.11	$7.84^{+2.01}_{-1.69}\times10^{-3}$	9.78×10^{-2}	5.71×10^{-2}	8.91×10^{-3}
0859−25	N	I10	0.305	14.758	−0.589	−26.83	1.83	2.38	$3.84^{+3.72}_{-2.05}\times10^{-2}$	1.39×10^{-2}	2.44×10^{-2}	1.01×10^{-1}
0915−11	E	I10	0.054	10.868	−0.137	−26.18	1.12	1.45	$9.17^{+1.23}_{-0.62}\times10^{-5}$	6.98×10^{-4}	2.88×10^{-3}	3.79×10^{-2}
0945+07	B	I10	0.086	12.376	−0.214	−25.81	0.84	1.10	$2.08^{+0.10}_{-0.07}\times10^{-1}$	2.56×10^{-2}	2.39×10^{-2}	1.54×10^{-2}
1151−34	Q	2M	0.258	14.040	−0.537	−27.08	2.22	2.88	$1.23^{+1.53}_{-0.15}\times10^{-2}$	3.40×10^{-2}	2.29×10^{-2}	2.77×10^{-2}
1306−09	N	I10	0.464	15.120	−0.666	−27.61	3.33	4.33	$1.88^{+0.02}_{-0.04}\times10^{-2}$	1.13×10^{-2}	1.63×10^{-2}	4.35×10^{-2}
1355−41	Q	I10	0.313	12.744	−0.597	−28.91	8.95	11.63	$5.60^{+1.69}_{-0.12}\times10^{-2}$	2.32×10^{-2}	1.73×10^{-2}	1.10×10^{-2}
1547−79	B	I10	0.483	15.185	−0.669	−27.66	3.44	4.47	$1.51^{+44.55}_{-0.91}\times10^{-1}$	2.11×10^{-1}	2.45×10^{-2}	7.76×10^{-2}
1559+02	N	I10	0.104	12.205	−0.256	−26.46	1.38	1.80	$4.75^{+0.14}_{-1.67}\times10^{-4}$	3.50×10^{-2}	5.90×10^{-2}	1.34×10^{-2}
1648+05	E	2M	0.154	12.550	−0.363	−27.14	2.33	3.03	$2.42^{+554.08}_{-2.42}\times10^{-4}$	5.21×10^{-4}	2.18×10^{-3}	1.61×10^{-1}
1733−56	B	I10	0.098	12.485	−0.242	−26.03	1.00	1.30	$3.75^{+1.53}_{-0.03}\times10^{-2}$	1.76×10^{-2}	1.74×10^{-2}	1.54×10^{-2}
1814−63	N	I10	0.063	11.896	−0.159	−25.52	0.68	0.88	$6.34^{+0.22}_{-0.46}\times10^{-2}$	1.71×10^{-3}	2.23×10^{-2}	2.64×10^{-2}
1839−48	E	2M	0.112	11.841	−0.274	−27.01	2.11	2.74	$1.19^{+1.35}_{-1.19}\times10^{-4}$	2.94×10^{-5}	2.14×10^{-3}	6.66×10^{-3}
1932−46	B	I10	0.231	14.971	−0.499	−25.84	0.86	1.12	$6.90^{+0.09}_{-0.18}\times10^{-3}$	7.49×10^{-2}	1.35×10^{-2}	2.72×10^{-1}
1934−63	N	I10	0.183	14.023	−0.419	−26.14	1.09	1.41	$2.20^{+12.07}_{-2.20}\times10^{-3}$	2.98×10^{-2}	2.86×10^{-2}	2.73×10^{-2}
1949+02	N	I10	0.059	11.333	−0.149	−25.92	0.92	1.20	$1.63^{+0.81}_{-0.43}\times10^{-2}$	2.10×10^{-2}	3.32×10^{-2}	6.30×10^{-3}
2135−14	Q	2M	0.200	12.404	−0.449	−28.00	4.47	5.81	$1.40^{+0.38}_{-1.40}\times10^{-1}$	7.82×10^{-2}	2.74×10^{-2}	8.54×10^{-3}
2211−17	E	I10	0.153	13.422	−0.361	−26.25	1.18	1.54	$2.81^{+0.16}_{-2.81}\times10^{-7}$	5.46×10^{-4}	1.72×10^{-3}	7.27×10^{-2}
2221−02	B	I10	0.057	11.448	−0.144	−25.73	0.79	1.03	$2.31^{+0.25}_{-0.22}\times10^{-2}$	5.77×10^{-2}	4.17×10^{-2}	3.20×10^{-3}
2250−41	N	I10	0.310	15.508	−0.594	−26.12	1.07	1.40	$4.35^{+28.50}_{-4.35}\times10^{-4}$	1.25×10^{-1}	4.97×10^{-2}	1.56×10^{-1}
2356−61	N	I10	0.096	12.559	−0.237	−25.90	0.91	1.18	$2.58^{+0.19}_{-0.22}\times10^{-2}$	2.68×10^{-2}	2.35×10^{-2}	3.24×10^{-2}

off when radiatively efficient accretion takes over. There are several NLRGs, in fact, where the contribution from the jet kinetic luminosity is higher than that of the radiative luminosity (see also Punsly & Zhang 2011).

5.3 Radiative luminosity and jet power: is there a correlation?

While we know that the empirical relation between low-frequency radio emission and jet kinetic power shows a large scatter, and that environmental factors play a fundamental role in this relation, past work has suggested that there is a direct correlation between radiative luminosity and jet power in radio-loud AGN (see e.g. fig. 1 in Rawlings & Saunders 1991, who find $Q = L_{\rm NLR}^{0.9\pm0.2}$). According to this scenario, the radiative output of the AGN corresponds to a fraction of its accretion power (which holds true for radio-quiet sources), and so does the jet power, so that both magnitudes are correlated. However, our results in Fig. 12 show that there is substantial scatter in this relationship even for the HERGs; when considering the HERG population only, there is no obvious correlation between the luminosity (in terms of Eddington) in the jet and in radiative

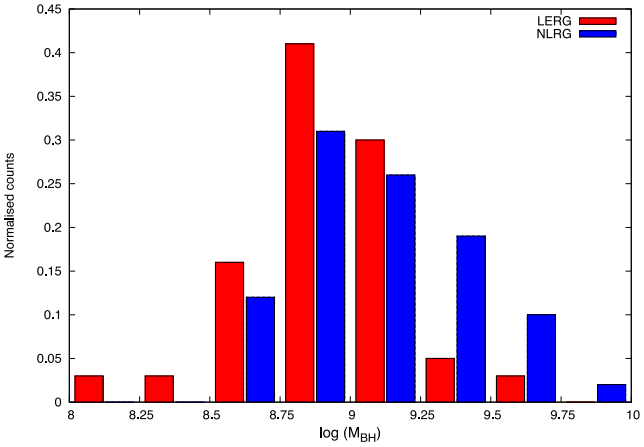

Figure 11. Histogram of black hole masses for the 2 Jy and 3CRR LERGs and NLRGs. Only narrow-line HERGs are included, to allow comparison between both samples and avoid issues with the unreliability of *K*-band-derived black hole masses in broad-line objects.

output, and, while excluding the LERGs limits the dynamic range, they cannot be considered in the same terms, due to their different accretion properties. Therefore, we must ask: is there any evidence for a physical relation between Q and $L_{\rm rad}$, beyond the fact that they are both linked to accretion?

We begin by noting that the interpretation of all these plots is complicated by the fact that that the radiative luminosity is essentially an instantaneous measurement, while the jet power is estimated from the large-scale radio lobes and so is a weighted average over the whole radio-loud lifetime of the source. This will certainly give rise to some of the scatter that we see, but it is not clear that it can account for the roughly one order of magnitude in dispersion about any relationship between radiative and kinetic luminosity.

We carried out tests for partial correlation between Q and $L_{\rm bol,[O\,III]}$ for the HERGs, in the presence of their common dependence on redshift, and also looked at the relationship between Q and $L_{\rm bol,\,IR}$ (Table 5). In the first case, which corresponds to the analysis of Rawlings & Saunders, we cannot reject the null hypothesis at a 3σ level; in the second there is a weak correlation for the overall sample, which disappears when the broad-line objects are removed. Our sample size is larger than that of Rawlings & Saunders: the crucial difference between our work and theirs is that we are not considering LERGs, which (because of their low jet powers and low emission-line/IR luminosities) would artificially strengthen any such correlation.

If there is no real physical correlation between the jet power and emission-line power, why are there positive correlations between related quantities such as $L_{\rm X_a}$ and L_{178} (Table 5)? We propose that these quantities are largely the result of selection bias. Any object classified as a narrow-line radio galaxy or a quasar – in other words, a classical AGN – has a radiative luminosity that cannot fall much below $0.01L_{\rm Edd}$ (see further below, Section 5.4) and cannot greatly exceed $L_{\rm Edd}$. By selecting the most luminous radio galaxies in the Universe, the 3CRR and 2 Jy samples, we are selecting for objects that have the highest possible jet powers – but these must also be limited by the accretion rate and so cannot greatly exceed $L_{\rm Edd}$. Thus, the most radio-loud objects in the universe should always populate the top right of plots like Fig. 12. However, crucially, this picture makes a prediction for less luminous samples of radio galaxies or radio-loud quasars that differs from that of the Rawlings & Saunders model. Classical AGN selected at lower radio powers

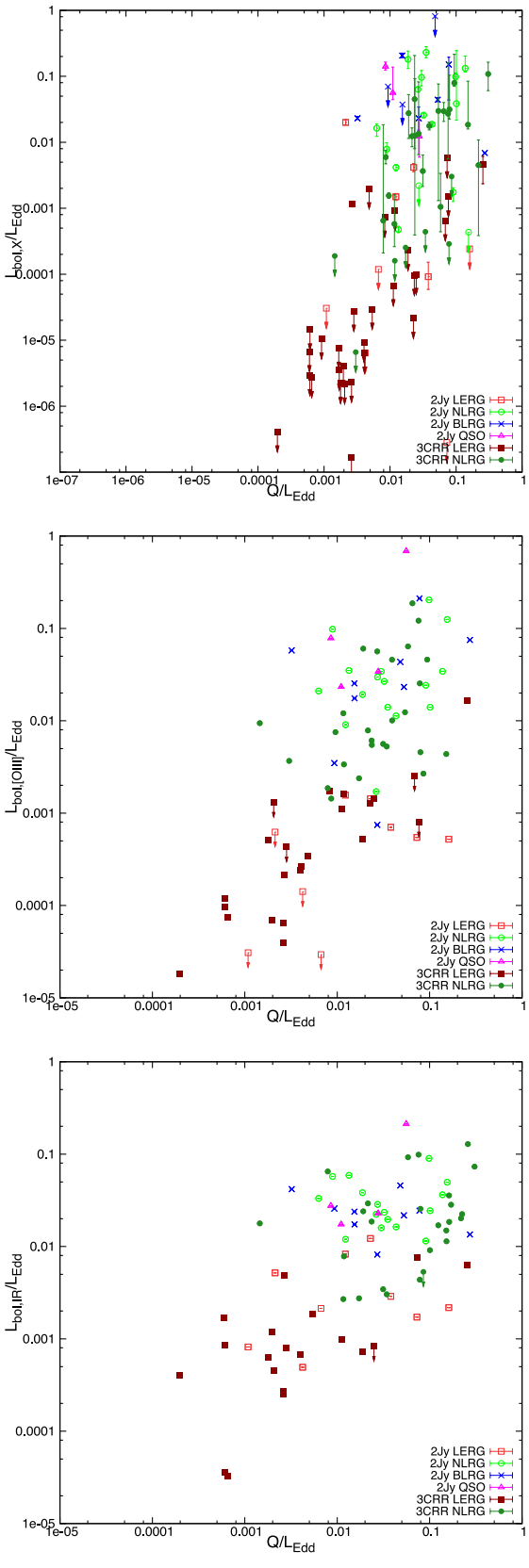

Figure 12. $L_{\rm bol}/L_{\rm Edd}$ versus $Q/L_{\rm Edd}$ for the 2 Jy and the 3CRR sources. Top: $L_{\rm bol,\,X}/L_{\rm Edd}$ versus $Q/L_{\rm Edd}$. Middle: $L_{\rm bol,[O\,III]}/L_{\rm Edd}$ versus $Q/L_{\rm Edd}$. Bottom: $L_{\rm bol,\,IR}/L_{\rm Edd}$ versus $Q/L_{\rm Edd}$. Error bars reflect the uncertainties in the accretion-related luminosity, but not systematics such as the uncertainty in absorption or intrinsic variability. Arrows indicate upper limits.

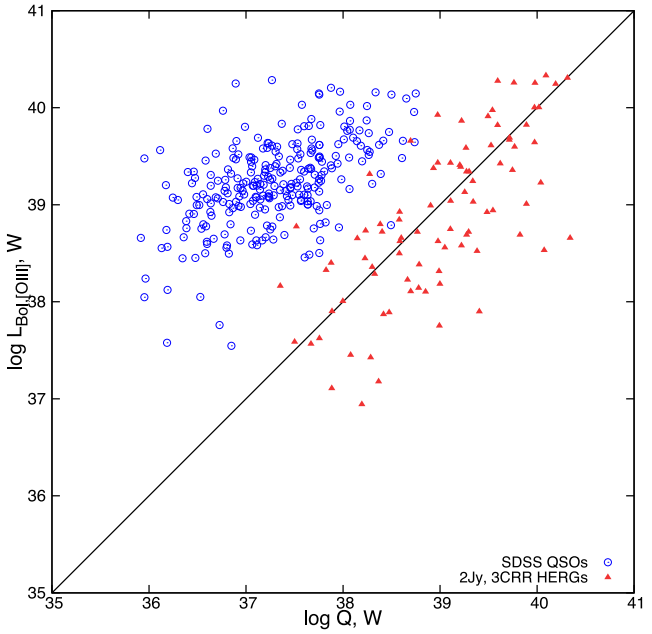

Figure 13. $L_{\mathrm{bol,[O\,III]}}$ versus Q for the 2 Jy and the 3CRR high-excitation objects and the SDSS quasars from Punsly & Zhang (2011). The line represents a 1:1 relation between both quantities.

are free to populate parts of the luminosity–luminosity plots to the left of the 3CRR/2 Jy objects in Fig. 12.

To test this picture, we have plotted HERGs in our 2 Jy and 3CRR samples next to the Sloan-selected quasars of Punsly & Zhang (2011). We have tested this comparison sample for several reasons: (i) it is quite large, (ii) as it is not radio selected, it samples objects with a range of radio outputs (which are also lower than those of the 2 Jy and 3CRR samples), and (iii) it contains [O III] and Q measures that we can directly compare to our own. Fig. 13 shows $L_{\mathrm{bol,[O\,III]}}$ versus Q for the objects in the Punsly & Zhang (2011) sample. As predicted, the SDSS QSOs lie well to the left of the 3CRR objects: for a given radiative power, they generally have much lower jet powers than the 3CRR/2 Jy objects. In the simple Rawlings & Saunders model, these objects (with lower radio powers) would be expected to lie two to three orders of magnitude lower in radiative power as well. This reinforces the conclusions of Punsly & Zhang (2011), who pointed out that there is no reason to expect $L_{\mathrm{bol,[O\,III]}}$ and Q to be correlated beyond the scaling with the central black hole. The picture also holds up for other samples for which jet power (or total radio power) has been correlated with $L_{\mathrm{[O\,III]}}$, including the 7C sources of Willott et al. (1999) and the SDSS QSOs from McLure & Jarvis (2004), which also lie systematically to the left of the line of equality in plots such as that in Fig. 13. The limiting case is provided by studies of very low luminosity radio-loud AGN such as that of Kauffmann, Heckman & Best (2008), where a very wide range of radio luminosities are necessarily sampled and where there is no apparent correlation between Q and L_{rad} at all.

We can thus conclude that, for radiatively efficient accretion, the same mechanism that powers radiative emission also powers the jet. But while the fraction of accretion power that is converted to radiative luminosity lies in a relatively narrow range, that which is converted to jet power can vary much more widely, presumably through some yet to be determined controlling parameter such as black hole spin: through selection biases, this fraction of the total accretion power reaches a maximum of ∼20 per cent Eddington in the 3CRR and 2 Jy samples that are the subject of this paper.

5.4 An Eddington switch?

We now explore the transition between HERGs and LERGs. Are both classes part of a continuous population? Is there a clear Eddington switch that makes an object efficient or inefficient, or is the LERG/HERG difference controlled partly or wholly by other factors, as in the models of Hardcastle et al. (2007a)? And how are environmental and observational effects affecting the distribution?

We plotted histograms of the total Eddington luminosity $[(L_{\mathrm{rad}} + Q_{\mathrm{jet}})/L_{\mathrm{Edd}}]$ for the three bands and the high/low-excitation populations. In all cases, we found the distribution to be clearly bimodal, with HERGs having systematically higher Eddington rates (peaking at ∼20 per cent Eddington) than LERGs (peaking at ∼1 per cent Eddington). The narrowest distribution is that obtained from the IR data (Fig. 14), but those derived from X-ray and [O III] measurements have coincident peaks and outliers.

Despite the fact that they have no influence on the result, we decided to remove the broad-line objects from the histograms to allow direct comparison between the 2 Jy and 3CRR samples (we have no K-band measurements for 3CRR BLRGs and QSOs), and to remove the bias derived from black hole masses that are, at best, uncertain for these objects.

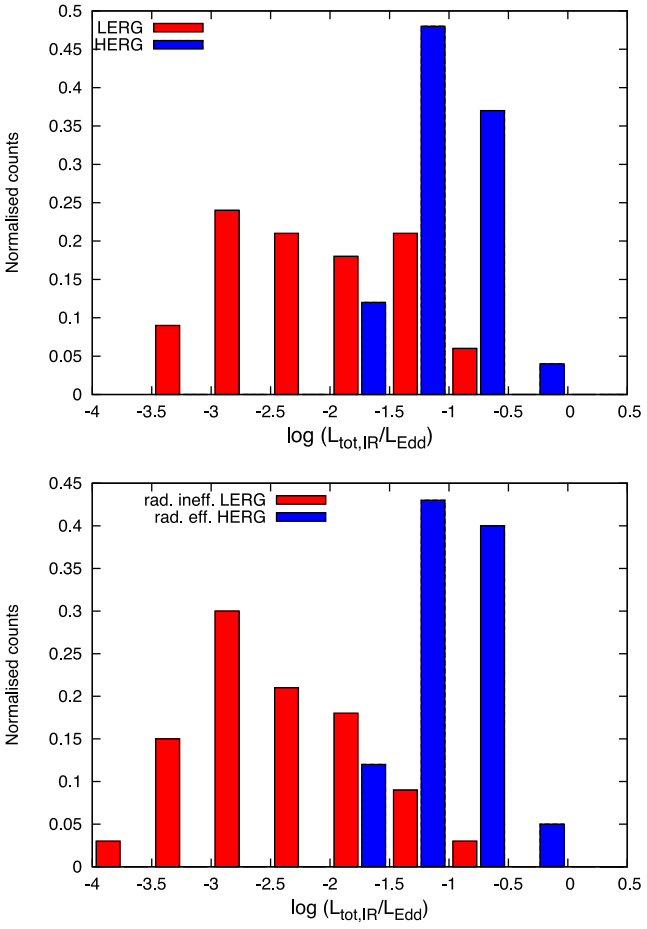

Figure 14. Histograms of total Eddington rate $[(L_{\mathrm{bol,\,IR}} + Q)/L_{\mathrm{Edd}}]$ distribution for the 2 Jy and the 3CRR sources. Broad-line objects are excluded from the HERGs to allow direct comparison between both samples. Top: all objects with available data are considered. Bottom: only radiatively inefficient LERGs and radiatively efficient HERGs are considered, and for the radiatively inefficient objects only Q is considered for the total luminosity.

Before any conclusions can be drawn on the existence of an Eddington switch between LERGs and HERGs, it is important to consider the nature of outliers (i.e. high Eddington LERGs). The LERGs with high Eddington rates fall into two categories: 'efficient' LERGs and cluster-embedded objects. To the former category belong PKS 0034−01 (3C 15), PKS 0043−42, PKS 0347+05, PKS 0625−35, 3C 123 and 3C 200 (see Hardcastle et al. 2006), all of which show signs of radiatively efficient accretion (bright accretion-related emission in X-rays, bright mid-IR emission and, in some cases, an Fe Kα line, see also Appendix A for details). To the latter category belong PKS 2211−17, PKS 1648+05 (Hercules A), PKS 0915−11 (Hydra A) and 3C 438. All these objects (save perhaps for Hydra A, which has a peculiar spectrum) are bona fide radiatively inefficient LERGs embedded in very dense clusters. It is possible that a boost of the jet luminosity due to the dense environment and an underestimation of the black hole mass (Volonteri & Ciotti 2013) are combining to produce this effect.

To test this effect, we have redone the histogram assuming that the LERGs have no measurable radiative contribution from radiatively efficient accretion (that is, taking into account only Q for these objects), and excluding all the sources for which the optical classification is inconsistent with our conclusions on the accretion mode (i.e. the 'efficient' LERGs). We have also excluded 3C 319, since our preliminary results on new X-ray data show that this source may not be a radiatively inefficient AGN, but an efficient one that has recently switched off. The histogram is shown in the bottom panel of Fig. 14.

After removing the outliers and the radiative contribution for the LERGs, we find that all our LERGs have $L/L_{\rm Edd} < 16$ per cent. 94 per cent of them have $L/L_{\rm Edd} < 10$ per cent, with 91 per cent of them having $L/L_{\rm Edd} < 3$ per cent. All the HERGs have $L/L_{\rm Edd} > 1$ per cent, with 88 per cent of the HERGs having $L/L_{\rm Edd} > 3$ per cent and 45 per cent of them having $L/L_{\rm Edd} > 10$ per cent.

Although the separation between the two populations is now clearer, there is still some overlap. The remaining LERGs with $\log(Q/L_{\rm Edd}) > -1.5$ are the cluster-embedded objects mentioned above. While it is difficult to assess by how much the black hole mass is underestimated in these galaxies, some of the plots of Volonteri & Ciotti (2013) show that these masses could be off by over half an order of magnitude. Hardcastle & Krause (2013) show that there is almost an order of magnitude scatter on the radio luminosity in their simulations for objects with the same jet powers, caused by the range of environmental densities tested. Therefore, the combination of these two effects could be enough to account for the high values of Q in cluster-embedded objects, and the reason behind the overlap between the two populations. If this were the case, our results would be compatible with a simple switch.

6 SUMMARY AND CONCLUSIONS

It is now clear that a classification that is based purely on morphological features, as that of Fanaroff & Riley (1974), emission-line properties, or orientation, as predicted by the simplest versions of models such as those described by Antonucci (1993) and Urry & Padovani (1995), cannot account for the underlying variety within the AGN population. As suggested by e.g. Hardcastle et al. (2007a), Lin et al. (2010), Antonucci (2012) and Best & Heckman (2012), we need a classification that encompasses both the physical properties and the observational properties of AGNs. This is particularly important for the LERG/HERG case, since there is an underlying physical difference between the two overall populations, but there are cases in which the observational, optical line classification belies the true nature of the accretion mode.

Although recent studies are beginning to take into account this intrinsic difference between the two populations, and progress is being made towards understanding the properties of LERGs, most samples still use restrictive selection criteria, employ only one or two energy bands to characterize the populations, contain objects which are misclassified and use bolometric corrections that do not accurately describe the less powerful sources. In our work, we present consistent results that question the accuracy of some of these assumptions, and prove that further, more careful analysis is needed to understand the relationship between radiative output and jet production in the overall AGN population.

Throughout this work, we have shown that the best way to reliably classify AGN populations is through a multiwavelength approach, which we use on our sample of 45 2 Jy and 135 3CRR sources [more than double the size of that studied by Hardcastle et al. (2009)]. We show that several objects classified as LERGs based on their optical spectra (PKS 0034−01, PKS 0043−42, PKS 0625−35, 3C 123, 3C 200 and more recently PKS 0347+05) are most likely radiatively efficient sources.

We find the same strong correlations between hard (2–10 keV) X-ray, mid-IR and [O III] emission as Hardcastle et al. (2006, 2009), confirming that these quantities are all related to radiatively efficient accretion. We confirm the jet-related nature of the soft X-ray emission, as suggested by Hardcastle & Worrall (1999). We also show that selection criteria must be taken into account when studying correlations between these quantities: relativistic beaming can introduce a large scatter in the plots, resulting in poorer partial correlations. We find that all the correlations of Hardcastle et al. (2009) become stronger by the addition of the 2 Jy objects.

By comparing the accretion-related correlations, we show that mid-IR measurements are best to constrain the accretion properties of high-excitation objects, while for the low-excitation population X-rays are the best band to set an upper limit on radiatively efficient accretion, given that X-rays are less subject to contamination from stellar processes and the presence of a jet (this is taken into account by the soft X-ray component, whose jet-related nature we confirm). Radio measurements are essential to establish the extent of radiatively inefficient accretion and the amount of AGN power invested in the jet.

We emphasize the fact that bolometric corrections, $M_{\rm BH}/L$ correlations and jet power estimations only give an overall indication of AGN behaviour, and may be inaccurate for individual sources, given the vast range of environments and nuclear powers involved. Further studies of individual spectral energy distributions (SEDs) and jet–environment interaction simulations are needed to establish how reliable these correlations are, in particular for the case of LERGs.

Despite these intrinsic limitations, we find very strong evidence of the radiatively inefficient nature of the LERGs, as well as confirmation for the fact that these objects accrete at very low Eddington rates (<10 per cent in all cases but one, with the distribution peaking at ∼1 per cent), as expected from the theoretical models (e.g. Narayan & Yi 1995). We find that the HERGs in our sample are narrowly distributed around 10 per cent Eddington rates, with roughly half of the objects having greater values. However, we find an overlap between both populations, which at first sight is not consistent with a simple switch at a given value of $L/L_{\rm Edd}$. Even after discarding the objects whose classification belies the intrinsic accretion properties (i.e. plotting what we know are unequivocally radiatively efficient HERGs and radiatively inefficient LERGs), we find that

LERGs embedded in very rich clusters have higher $L/L_{\rm Edd}$. For these sources, the central back hole masses may be underestimated and the lobe luminosity may be higher (Hardcastle & Krause 2013). These two factors can account for the order of magnitude in $L/L_{\rm Edd}$ that makes these objects overlap with the HERGs, in which case a simple switch between the two populations would be feasible.

We do not see signs in our plots for radiatively efficient accretion completely taking over from jet production. In fact, we find several NLRGs in which the dominant energetic contribution from the AGN stems from the jet, rather than radiative luminosity. Selection on radio flux selects for the objects with the largest values of Q at any given epoch. We find that jet kinetic power and radiative luminosity seem to have a common underlying mechanism, but are not correlated in radiatively efficient objects, confirming the conclusions of Punsly & Zhang (2011). While a better understanding of the time-scales and the addition of radio-quiet objects to the plots are necessary to fully understand whether these quantities are truly uncorrelated, our plots and correlation analysis seem to indicate that they are.

As part of our in-depth study of the 2 Jy sample, in our second paper we will analyse the non-thermal, extended X-ray emission of the low-redshift sources observed by *Chandra*, to characterize the properties of their jets, hotspots and lobes. This will be the first time a systematic study of this nature will have been carried out on a complete sample of radio galaxies, and it will allow us to gain further insight on the particle content and the effects of beaming across the entire radio-loud population. A third paper will study the environments of the 2 Jy and 3CRR samples, focusing on the extended, thermal X-ray emission.

ACKNOWLEDGEMENTS

BM thanks the University of Hertfordshire for a PhD studentship. This work is based on observations obtained with *XMM–Newton*, an ESA science mission with instruments and contributions directly funded by ESA Member States and NASA. It has also made use of new and archival data from *Chandra* and software provided by the Chandra X-ray Center (CXC) in the application package CIAO. We thank Dr B. Punsly for giving us access to his data for Fig. 13. We also thank the anonymous referee for the useful comments.

REFERENCES

Akritas M. G., Siebert J., 1996, MNRAS, 278, 919
Antognini J., Bird J., Martini P., 2012, ApJ, 756, 116
Antonucci R., 1993, ARA&A, 31, 473
Antonucci R., 2012, Astron. Astrophys. Trans., 27, 557
Asmus D., Gandhi P., Smette A., Hönig S. F., Duschl W. J., 2011, A&A, 536, A36
Balmaverde B., Baldi R. D., Capetti A., 2008, A&A, 486, 119
Best P. N., Heckman T. M., 2012, MNRAS, 421, 1569
Best P. N., Longair M. S., Roettgering H. J. A., 1998, MNRAS, 295, 549
Best P. N., Kauffmann G., Heckman T. M., Brinchmann J., Charlot S., Ivezić Ž., White S. D. M., 2005, MNRAS, 362, 25
Blundell K. M., Rawlings S., 2001, ApJ, 562, L5
Bower R. G., Benson A. J., Malbon R., Helly J. C., Frenk C. S., Baugh C. M., Cole S., Lacey C. G., 2006, MNRAS, 370, 645
Buttiglione S., Capetti A., Celotti A., Axon D. J., Chiaberge M., Macchetto F. D., Sparks W. B., 2009, A&A, 495, 1033
Carter C., Karovska M., Jerius D., Glotfelty K., Beikman S., 2003, in Payne H. E., Jedrzejewski R. I., Hook R. N., eds, ASP Conf. Ser. Vol. 295, Astronomical Data Analysis Software and Systems XII. Astron. Soc. Pac., San Francisco, p. 477
Cattaneo A. et al., 2009, Nature, 460, 213
Cavagnolo K. W., McNamara B. R., Nulsen P. E. J., Carilli C. L., Jones C., Bîrzan L., 2010, ApJ, 720, 1066
Chiaberge M., Capetti A., Celotti A., 2002, A&A, 394, 791
Croston J. H., Hardcastle M. J., Birkinshaw M., Worrall D. M., Laing R. A., 2008, MNRAS, 386, 1709
Croston J. H., Hardcastle M. J., Mingo B., Evans D. A., Dicken D., Morganti R., Tadhunter C. N., 2011, ApJ, 734, L28
Croton D. J. et al., 2006, MNRAS, 365, 11
Danziger I. J., Fosbury R. A. E., Boksenberg A., Goss W. M., Bland J., 1984, MNRAS, 208, 589
de Vries W. H., O'Dea C. P., Perlman E., Baum S. A., Lehnert M. D., Stocke J., Rector T., Elston R., 1998, ApJ, 503, 138
Dicken D., Tadhunter C., Morganti R., Buchanan C., Oosterloo T., Axon D., 2008, ApJ, 678, 712
Dicken D., Tadhunter C., Axon D., Morganti R., Inskip K. J., Holt J., González Delgado R., Groves B., 2009, ApJ, 694, 268
Dicken D. et al., 2012, ApJ, 745, 172
Dickey J. M., Lockman F. J., 1990, ARA&A, 28, 215
Elvis M. et al., 1994, ApJS, 95, 1
Evans D. A., Worrall D. M., Hardcastle M. J., Kraft R. P., Birkinshaw M., 2006, ApJ, 642, 96
Evans D. A., Summers A. C., Hardcastle M. J., Kraft R. P., Gandhi P., Croston J. H., Lee J. C., 2011, ApJ, 741, L4
Fanaroff B. L., Riley J. M., 1974, MNRAS, 167, 31p
Fernández-Ontiveros J. A., Prieto M. A., Acosta-Pulido J. A., Montes M., 2012, J. Phys.: Conf. Ser., 372, 012006
Fukugita M., Shimasaku K., Ichikawa T., 1995, PASP, 107, 945
Gandhi P., Horst H., Smette A., Hönig S., Comastri A., Gilli R., Vignali C., Duschl W., 2009, A&A, 502, 457
Glazebrook K., Peacock J. A., Miller L., Collins C. A., 1995, MNRAS, 275, 169
Godfrey L. E. H., Shabala S. S., 2013, ApJ, 767, 12
Graham A. W., 2007, MNRAS, 379, 711
Haardt F., Maraschi L., 1991, ApJ, 380, L51
Hardcastle M. J., Worrall D. M., 1999, MNRAS, 309, 969
Hardcastle M. J., Krause M. G. H., 2013, MNRAS, 430, 174
Hardcastle M. J., Evans D. A., Croston J. H., 2006, MNRAS, 370, 1893
Hardcastle M. J., Evans D. A., Croston J. H., 2007a, MNRAS, 376, 1849
Hardcastle M. J., Croston J. H., Kraft R. P., 2007b, ApJ, 669, 893
Hardcastle M. J., Evans D. A., Croston J. H., 2009, MNRAS, 396, 1929
Heckman T. M., Kauffmann G., Brinchmann J., Charlot S., Tremonti C., White S. D. M., 2004, ApJ, 613, 109
Hine R. G., Longair M. S., 1979, MNRAS, 188, 111
Ho L. C., 2009, ApJ, 699, 626
Holt J., Tadhunter C. N., Morganti R., 2008, MNRAS, 387, 639
Holt J., Tadhunter C. N., Morganti R., 2009, MNRAS, 400, 589
Hopkins P. F., 2012, MNRAS, 420, L8
Ineson J., Croston J. H., Hardcastle M. J., Kraft R. P., Evans D. A., Jarvis M., 2013, ApJ, 770, 136
Inskip K. J., Tadhunter C. N., Dicken D., Holt J., Villar-Martín M., Morganti R., 2007, MNRAS, 382, 95
Inskip K. J., Tadhunter C. N., Morganti R., Holt J., Ramos Almeida C., Dicken D., 2010, MNRAS, 407, 1739
Jackson N., Browne I. W. A., 1990, Nature, 343, 43
Janssen R. M. J., Röttgering H. J. A., Best P. N., Brinchmann J., 2012, A&A, 541, A62
Kauffmann G., Heckman T. M., Best P. N., 2008, MNRAS, 384, 953
Körding E. G., Jester S., Fender R., 2006, MNRAS, 372, 1366
Kraft R. P., Vázquez S. E., Forman W. R., Jones C., Murray S. S., Hardcastle M. J., Worrall D. M., Churazov E., 2003, ApJ, 592, 129
Kraft R. P., Hardcastle M. J., Worrall D. M., Murray S. S., 2005, ApJ, 622, 149
Laing R. A., Riley J. M., Longair M. S., 1983, MNRAS, 204, 151
Laing R. A., Jenkins C. R., Wall J. V., Unger S. W., 1994, in Bicknell G. V., Dopita M. A., Quinn P. J., eds, ASP Conf. Ser. Vol. 54, The Physics of Active Galaxies. Astron. Soc. Pac., San Francisco, p. 201

Lane W. M., Clarke T. E., Taylor G. B., Perley R. A., Kassim N. E., 2004, AJ, 127, 48
Lilly S. J., Longair M. S., 1984, MNRAS, 211, 833
Lin Y.-T., Shen Y., Strauss M. A., Richards G. T., Lunnan R., 2010, ApJ, 723, 1119
Magorrian J. et al., 1998, AJ, 115, 2285
Mannucci F., Basile F., Poggianti B. M., Cimatti A., Daddi E., Pozzetti L., Vanzi L., 2001, MNRAS, 326, 745
Marconi A., Risaliti G., Gilli R., Hunt L. K., Maiolino R., Salvati M., 2004, MNRAS, 351, 169
Martel A. R. et al., 1999, ApJS, 122, 81
Mason R. E. et al., 2012, AJ, 144, 11
McLure R. J., Jarvis M. J., 2004, MNRAS, 353, L45
McNamara B. R., Nulsen P. E. J., 2007, ARA&A, 45, 117
Mingo B., Hardcastle M. J., Croston J. H., Evans D. A., Hota A., Kharb P., Kraft R. P., 2011, ApJ, 731, 21
Morganti R., Killeen N. E. B., Tadhunter C. N., 1993, MNRAS, 263, 1023
Morganti R., Oosterloo T., Tadhunter C. N., Aiudi R., Jones P., Villar-Martin M., 1999, A&AS, 140, 355
Morganti R., Holt J., Tadhunter C., Ramos Almeida C., Dicken D., Inskip K., Oosterloo T., Tzioumis T., 2011, A&A, 535, A97
Narayan R., Yi I., 1995, ApJ, 452, 710
Netzer H., 2009, MNRAS, 399, 1907
Ojha R., Fey A. L., Johnston K. J., Jauncey D. L., Tzioumis A. K., Reynolds J. E., 2004, AJ, 127, 1977
Plotkin R. M., Anderson S. F., Brandt W. N., Markoff S., Shemmer O., Wu J., 2012, ApJ, 745, L27
Prieto M. A., Walsh J. R., Fosbury R. A. E., di Serego Alighieri S., 1993, MNRAS, 263, 10
Punsly B., Zhang S., 2011, ApJ, 735, L3
Quataert E., 2003, Astron. Nachr. Suppl., 324, 435
Ramos Almeida C., Tadhunter C. N., Inskip K. J., Morganti R., Holt J., Dicken D., 2011a, MNRAS, 410, 1550
Ramos Almeida C., Dicken D., Tadhunter C., Asensio Ramos A., Inskip K. J., Hardcastle M. J., Mingo B., 2011b, MNRAS, 413, 2358
Ramos Almeida C., Rodríguez Espinosa J. M., Acosta-Pulido J. A., Alonso-Herrero A., Pérez García A. M., Rodríguez-Eugenio N., 2013, MNRAS, 429, 3449
Rawlings S., Saunders R., 1991, Nature, 349, 138
Rector T. A., Stocke J. T., 2001, AJ, 122, 565
Rinn A. S., Sambruna R. M., Gliozzi M., 2005, ApJ, 621, 167
Risaliti G., Woltjer L., Salvati M., 2003, A&A, 401, 895
Runnoe J. C., Brotherton M. S., Shang Z., 2012, MNRAS, 422, 478
Russell H. R., McNamara B. R., Edge A. C., Hogan M. T., Main R. A., Vantyghem A. N., 2013, MNRAS, 432, 530
Saikia D. J., Jamrozy M., 2009, Bull. Astron. Soc. India, 37, 63
Sambruna R. M., Chartas G., Eracleous M., Mushotzky R. F., Nousek J. A., 2000, ApJ, 532, L91
Sambruna R. M., Gliozzi M., Tavecchio F., Maraschi L., Foschini L., 2006, ApJ, 652, 146
Shakura N. I., Sunyaev R. A., 1973, A&A, 24, 337
Siebert J., Brinkmann W., Morganti R., Tadhunter C. N., Danziger I. J., Fosbury R. A. E., di Serego Alighieri S., 1996, MNRAS, 279, 1331
Silk J., Rees M. J., 1998, A&A, 331, L1
Simpson C., Ward M., Wall J. V., 2000, MNRAS, 319, 963
Tadhunter C. N., Morganti R., di Serego-Alighieri S., Fosbury R. A. E., Danziger I. J., 1993, MNRAS, 263, 999
Tadhunter C. N., Morganti R., Robinson A., Dickson R., Villar-Martin M., Fosbury R. A. E., 1998, MNRAS, 298, 1035
Tadhunter C., Dickson R., Morganti R., Robinson T. G., Wills K., Villar-Martin M., Hughes M., 2002, MNRAS, 330, 977
Tadhunter C. N., Ramos Almeida C., Morganti R., Holt J., Rose M., Dicken D., Inskip K., 2012, MNRAS, 427, 1603
Uchiyama Y. et al., 2007, ApJ, 661, 719
Urry C. M., Padovani P., 1995, PASP, 107, 803
van der Wolk G., Barthel P. D., Peletier R. F., Pel J. W., 2010, A&A, 511, A64
Volonteri M., Ciotti L., 2013, ApJ, 768, 29
Wall J. V., Peacock J. A., 1985, MNRAS, 216, 173
Willott C. J., Rawlings S., Blundell K. M., Lacy M., 1999, MNRAS, 309, 1017
Wills K. A., Morganti R., Tadhunter C. N., Robinson T. G., Villar-Martin M., 2004, MNRAS, 347, 771
Worrall D. M., Tananbaum H., Giommi P., Zamorani G., 1987, ApJ, 313, 596
Wright A., Otrupcek R., 1990, Parkes Catalog, 1990, Australia telescope national facility, ATNF, Sydney

APPENDIX A: NOTES ON INDIVIDUAL OBJECTS

A1 PKS 0023−26

PKS 0023−26 has a young stellar population (Dicken et al. 2012) and redshifted H I emission consistent with infalling gas (Holt, Tadhunter & Morganti 2008). Its X-ray spectrum is quite atypical for what is expected in NLRGs, with a dominating jet-related component and low intrinsic absorption.

A2 PKS 0034−01 (3C 15)

PKS 0034−01 has a radio morphology that is intermediate between that of an FR I and an FR II. The host galaxy has a dust lane (Martel et al. 1999). Although this object is classified as an LERG, in our plots it is near the luminosity break between LERGs and NLRGs ($L_{\rm X,2-10\,keV} = 6.6 \times 10^{42}$ erg s^{-1}, see Table 2). Its spectrum is relatively obscured ($N_{\rm H} \sim 10^{23}$ cm^{-2}), and requires two power-law components. We do not detect an Fe Kα line, as we did for PKS 0043−42. It is unclear whether PKS 0034−01 is a 'true' (albeit somewhat atypical) LERG, a low-luminosity NLRG or an intermediate case. The absence of a torus (van der Wolk et al. 2010) seems to point towards the first possibility, though its poor environment makes it difficult to explain where the hot gas for a radiatively inefficient accretion scenario might come from.

A3 PKS 0035−02 (3C 17)

The optical spectrum of PKS 0035−02 shows double-peaked Balmer lines. Its X-ray spectrum shows two distinct components and some intrinsic absorption, which is not overly frequent in broad-line objects due to orientation.

A4 PKS 0038+09 (3C 18)

The X-ray spectrum of this BLRG is bright (we had to correct it for pileup), and is well described with a single power-law component, with no traces of intrinsic absorption, as is expected for most broad-line objects.

A5 PKS 0039−44

The optical nucleus of this NLRG seems to be dusty, and it is believed to have two components (Ramos Almeida et al. 2011a), which are not resolved in our *XMM* images. Its X-ray spectrum is bright, with two distinct components, some intrinsic absorption and a prominent Fe Kα line.

A6 PKS 0043−42

PKS 0043−42 has a very extended radio morphology and no detectable radio core (Morganti et al. 1999). Although it is classified

as an LERG, PKS 0043−42 is most likely a high-excitation object where the strong emission lines are simply not detected. Ramos Almeida et al. (2011a) find distinct evidence for a clumpy torus in their *Spitzer* data, and its X-ray spectrum shows clear signatures of radiatively efficient accretion, in the form of a bright hard component and an Fe Kα emission line. Its high luminosity situates this object in the parameter space occupied by the fainter NLRGs in our plots.

A7 PKS 0105−16 (3C 32)

The spectrum we extracted from the *XMM* images is quite typical for an NLRG, with two components, intrinsic absorption and a noticeable Fe Kα line.

A8 PKS 0213−13 (3C 62)

The spectrum of PKS 0213−13 is dominated by the hard component, with the soft, jet-related component being very faint.

A9 PKS 0235−19

The X-ray spectrum of the BLRG PKS 0235−19 is not very bright, and is best modelled with a single power law with foreground absorption. This faintness is unexpected, given that this source is very bright in the [O III] and mid-IR bands, making it a clear outlier in our plots (see the bottom panels of Figs 6 and 7).

A10 PKS 0252−71

PKS 0252−71 has a compact radio morphology. Its X-ray spectrum is quite faint, it features two distinct components (the jet-related one being brighter) and some absorption.

A11 PKS 0347+05

This object was previously classified as a BLRG, but a recent study by Tadhunter et al. (2012) suggests that this is in fact a double system with a radio-loud object and a Seyfert 1 radio-quiet AGN. It was already known that this was an interacting system (Inskip et al. 2010; Ramos Almeida et al. 2011a), but given these recent results it is very possible that we are measuring data from both objects, given that the galaxies are only 5 arcsec apart, and we are thus unable to resolve them. The optical spectra analysed by Tadhunter et al. (2012) suggest that the broad lines previously attributed to the radio source belong instead to the Seyfert, and the line ratios seem to indicate that the radio galaxy is an LERG. They suggest that the latter source is just a relic, having recently switched off, since they do not detect the radio core. The *XMM* images show that the emission is centred between both sources, with more emission coming from the region associated with the radio source. The spectrum we analyse has a relatively bright soft component and a much brighter, though heavily absorbed hard component, although the $N_{\rm H}$ column is not very well constrained. This is not compatible with the spectrum of a Seyfert 1 galaxy; we therefore assume that the radio-loud AGN is still active (in contrast to the suggestion of Tadhunter et al. 2012), and is indeed the main contributor to the X-ray spectrum, which is more consistent with that of an NLRG. We have decided to use the optical LERG classification for this source, although that makes it an outlier in most of our plots, due to its brightness. The X-ray excess (as compared to other LERGs) could be attributed to the contribution from the Seyfert core, and the IR excess to the presence of star formation (Dicken et al. 2012), but in any case the true nature of this source remains uncertain. To further complicate the scenario, the rich ICM could also be contributing to the soft X-ray emission, although our data do not allow us to quantify this effect.

A12 PKS 0349−27

This well-known FR II galaxy has some remarkable optical features, including a spectacular extended emission-line nebulosity (Danziger et al. 1984). The X-ray spectrum shows very little absorption and is completely dominated by the hard component; we were only able to obtain an upper limit on the jet-related power law (see Table 2).

A13 PKS 0404+03 (3C 105)

The host of PKS 0404+03 has been studied in detail in the optical and IR (see Inskip et al. 2010, and references therein), despite the presence of a nearby star and the high foreground $N_{\rm H}$ column. The *Chandra* spectrum is somewhat atypical, with high intrinsic absorption, very faint soft emission ($\sim$20 photon counts between 0.4 and 3 keV) and a bright accretion-related component. It is possible that the high intrinsic absorption we estimate is a consequence of an underestimation in the foreground extinction (see Section 2.3).

A14 PKS 0409−75

This FR II has the highest redshift in our sample, and is one of the brightest radio sources in the Southern hemisphere (Morganti et al. 1999). It has a young stellar population (Dicken et al. 2012) and it seems to have a double optical nucleus (Ramos Almeida et al. 2011a). Its X-ray spectrum is also very bright, and atypical, with the jet-related component clearly dominant, no detectable intrinsic absorption and only an upper limit on the accretion-related component, which, however, has a detectable Fe Kα line. As pointed out in Section 2.3, this object is an outlier in most of the plots, having a much brighter soft X-ray luminosity than would be expected from the correlations. Given that it lies in a relatively dense cluster environment, it is possible that some of the soft X-ray excess may be caused by inverse-Compton emission from the radio lobes, which are not resolved by *XMM*. This would be consistent with the fact that PKS 0409−75 is also an outlier in the top panel of Fig. 5. A detailed study of the X-ray emission from the ICM is needed to assess its contribution to the soft X-ray luminosity of this NLRG.

A15 PKS 0442−28

The spectrum of this source is very bright, with low intrinsic absorption (atypical for an NLRG) and a strong accretion-related component. There seems to be some excess emission around 5–6 keV, indicating the possible presence of an Fe Kα line, but adding a Gaussian component to the best-fitting model did not improve the statistics.

A16 PKS 0620−52

This LERG has the lowest redshift in our sample, and shows evidence for a young stellar population (Dicken et al. 2012). Its spectrum is quite faint; we were able to detect and fit the soft component, but obtained only an upper limit on the accretion-related emission.

A17 PKS 0625−35

This object is suspected to be a BL Lac (Wills et al. 2004). Although optically classified as an LERG, it is clear from our data that this is not a 'standard' low-excitation object. The *Chandra* image shows a large streak and is piled up. The spectrum is very bright, with some intrinsic absorption and two power-law components. In our plots, PKS 0625−35 sits near the low-luminosity end of the NLRGs, its accretion-related luminosity being only below that of PKS 0043−42 and PKS 0034−01, which are both 'dubious' LERGs. Beaming might account for the enhanced luminosity.

A18 PKS 0625−53

This LERG is hosted by a dumbbell galaxy, which is also the brightest member in Abell 3391. It has an FR I radio morphology with a wide-angled tail (Morganti et al. 1999) and a deflected jet. A strong nuclear component is not detected in the IR (Inskip et al. 2010), consistent with the classification as a low-excitation object. The *Chandra* image shows a very faint nucleus; our spectrum only has one bin, which allows us to constrain an upper limit to the luminosity.

A19 PKS 0806−10 (3C 195)

Our *Chandra* spectrum is bright, with a strong accretion-related component and some intrinsic absorption. Although its accretion-related luminosity is somewhat smaller than expected (this is the most luminous object in the 2 Jy sample at $z < 2$ in the [O III] and mid-IR bands), it falls within the overall correlations in the bottom panels of Figs 6 and 7; thus, it is not likely to be Compton thick.

A20 PKS 0859−25

This NLRG seems to have a double nucleus (Ramos Almeida et al. 2011a). Its *XMM* spectrum is remarkable in that it shows a very prominent Fe Kα line.

A21 PKS 0915−11 (3C 218, Hydra A)

Hydra A is a very well-studied galaxy. It sits in the centre of a rich cluster and is one of the most powerful local radio sources (see e.g. Lane et al. 2004, and references therein). The optical emission lines are very weak, and the *K*-band imaging does not show a nuclear point source (Inskip et al. 2010). It also shows evidence for recent star formation (Dicken et al. 2012), which is not common in cluster-centre galaxies, but can be attributed to a recent merger [Ramos Almeida et al. (2011a) report the presence of a dust lane]. The AGN is very faint in X-rays, and its spectrum has a rather peculiar shape (Sambruna et al. 2000; Rinn, Sambruna & Gliozzi 2005), possibly because of contamination from thermal emission that our region selection cannot fully correct for. This situates Hydra A slightly apart from the bulk of the LERG population in our diagrams, relatively close to the LERG/HERG divide. The intrinsic $N_{\rm H}$ and the soft emission are rather well constrained, but the error in the normalization of the hard power-law component is quite large, which is reflected in the large error bars in our plots.

A22 PKS 0945+07 (3C 227)

This is a well-known BLRG, with a very extended optical emission-line region (Prieto et al. 1993). The *Chandra* spectrum is very bright, and requires pileup correction and some care when selecting the extraction region (there is a faint streak in the image). It is well modelled with two power laws and low, but well-constrained, intrinsic absorption (Hardcastle, Croston & Kraft 2007b).

A23 PKS 1136−13

This QSO has a very prominent jet which is visible in optical (Ramos Almeida et al. 2011a) and IR (Uchiyama et al. 2007), and extremely bright in the *Chandra* image, which also shows a prominent streak (Sambruna et al. 2006). The spectrum had to be corrected for pileup, and is modelled well with two components (the soft emission being dominant) and low intrinsic absorption.

A24 PKS 1151−34

This QSO seems to be interacting with a nearby spiral galaxy (Ramos Almeida et al. 2011a). Although the polycyclic aromatic hydrocarbon features in the *Spitzer* observations seem to indicate a young stellar population, this is not confirmed by the far-IR observations (Dicken et al. 2012). This source has double-peaked Balmer lines, and it is clearly radiatively efficient: the *XMM* spectrum is rather bright, and well modelled with two power laws (the hard component being much brighter than the soft one), a surprisingly high absorption column (which is also not very well constrained, see Table 2) and an Fe Kα emission line.

A25 PKS 1306−09

PKS 1306−09 has a double optical nucleus (Inskip et al. 2010; Ramos Almeida et al. 2011a). Its *XMM* spectrum shows no signs of a jet-related component and requires some intrinsic absorption.

A26 PKS 1355−41

The *XMM* spectrum requires two power-law components and very low intrinsic absorption.

A27 PKS 1547−79

PKS 1547−79 shows a double nucleus both in the optical (Ramos Almeida et al. 2011a) and IR images (Inskip et al. 2010). Its *XMM* spectrum is rather peculiar, and not very bright, probably due to the high redshift. There may be signs of thermal contamination in the soft emission, and heavy intrinsic absorption is required for a good fit, but is very poorly constrained. This is very atypical for a BLRG, and possibly an effect of the poor spectral quality (the observation suffers from rather heavy flare contamination for about 70 per cent of the exposure time), but careful flare filtering and rebinning of the data resulted in no improvements in the fits.

A28 PKS 1559+02 (3C 327)

The host galaxy of this NLRG is very massive, and seems to have a bifurcated dust lane (Inskip et al. 2010; Ramos Almeida et al. 2011a), which crosses the nucleus. van der Wolk et al. (2010) report a large IR excess that extends beyond what is expected for a torus. The *Chandra* image shows a very bright nucleus, which is close to the edge of the S3 chip. The spectrum is best fitted with two components and low intrinsic absorption, and an Fe Kα emission line, which is not very well constrained (Hardcastle et al. 2007b). As for PKS 0409−75 (Appendix A14), it is remarkable that the Fe line

is detected despite the faintness of the accretion-related component. As pointed out in Section 4, it is very likely that this object is Compton thick, given that its accretion-related X-ray luminosity is much fainter than what should be expected from its [O III] and IR luminosities.

A29 PKS 1602+01 (3C 327.1)

The host galaxy seems to have a double optical nucleus (Ramos Almeida et al. 2011a) and perhaps an extended emission-line region (Morganti et al. 1999). The *XMM* spectrum has two bright components, with no intrinsic absorption.

A30 PKS 1648+05 (3C 348, Hercules A)

Hercules A is a cluster-embedded LERG with some unusual radio properties (Morganti et al. 1993). Dust features are detected in the optical images (Ramos Almeida et al. 2011a). Its nuclear X-ray spectrum is very faint, with soft emission being the main contributor. We were only able to constrain an upper limit for the hard component.

A31 PKS 1733−56

The host galaxy of PKS 1733−56 shows clear evidence of recent star formation (Dicken et al. 2012) and a disturbed optical morphology (Inskip et al. 2010; Ramos Almeida et al. 2011a). The *Chandra* spectrum is very bright, and had to be corrected for pileup. It is also quite typical of a BLRG, with low intrinsic absorption which does not allow us to distinguish clearly between both components. There is a faint excess ∼6 keV which could be related to an Fe Kα emission line, but adding an extra component does not improve the fit.

A32 PKS 1814−63

PKS 1814−63 shows clear traces of an optical disc and a dust lane (Inskip et al. 2010; Ramos Almeida et al. 2011a), which is atypical for a system with this radio luminosity (Morganti et al. 2011). It also shows evidence for starburst activity (Dicken et al. 2012) and has an extended emission-line region (Holt, Tadhunter & Morganti 2008, 2009). Its *Chandra* spectrum is bright and dominated by a relatively unobscured hard component, as typical for NLRGs. It also has an Fe Kα emission line.

A33 PKS 1839−48

This FR I is another example of a cluster-embedded LERG (Ramos Almeida et al. 2011a). van der Wolk et al. (2010) report no detection of a dusty torus, which is consistent with the classification of this object as low excitation. Its X-ray spectrum has a relatively bright soft component, but no traces of accretion-related emission, for which we were only able to constrain an upper limit.

A34 PKS 1932−46

The host of this BLRG shows signs of ongoing star formation (Dicken et al. 2012), has an extended emission-line region (Inskip et al. 2007) and its core seems to be relatively faint in the *K* band (Inskip et al. 2010); its IR luminosity is also rather low in our plots, while it is quite bright in [O III]. The X-ray spectrum is not very bright, and is best modelled with a single, unobscured component, which does not allow us to distinguish between jet- and accretion-related emission. This is consistent with the interpretation of Inskip et al. (2007), who suggest that the nucleus has switched off, but such a short time ago that this information has not yet the extended narrow-line region.

A35 PKS 1934−63

This source has a compact double radio morphology (Ojha et al. 2004) and is optically very blue (Ramos Almeida et al. 2011a). It also shows evidence for infalling gas (Holt et al. 2008, 2009). Its radio spectrum is prototypical for a gigahertz-peaked source, and is self-absorbed; thus, we could only derive an upper limit to its 178 and 151 MHz fluxes. Its X-ray spectrum is dominated by the soft component, and we are not able to disentangle the obscuring column from the hard component, nor do we detect the Fe Kα reported by Risaliti, Woltjer & Salvati (2003) from their *Beppo-SAX* observations. It is possible that this object is heavily obscured, although we do not see an excess in IR emission to support this.

A36 PKS 1938−15

The spectrum of this BLRG has two components and a low intrinsic $N_{\rm H}$ column. It has an excess compatible with an Fe Kα emission line; adding this component improves the fit slightly.

A37 PKS 1949+02 (3C 403)

PKS 1949+02 is an NLRG with an X-shaped radio morphology, and as such it has been studied in some detail (see Ramos Almeida et al. 2011a, and references therein). Its X-ray spectrum has also been studied in detail (Kraft et al. 2005; Balmaverde, Baldi & Capetti 2008), it is dominated by the hard component, rather obscured, and it has a very prominent Fe Kα emission line.

A38 PKS 1954−55

The spectrum of this LERG is rather faint, and only a soft component is detected.

A39 PKS 2135−14

The spectrum of this QSO is bright, and had to be corrected for pileup. It has two distinct components and some intrinsic obscuration. There is some excess above 5 keV which we have not been able to model.

A40 PKS 2135−20

The host of this BLRG shows evidence for star formation (Dicken et al. 2012), and is classified as an ultraluminous infrared galaxy (ULIRG). Although the quality of the spectrum is rather poor, given the low luminosity of the source (for a BLRG) and the high redshift, we detect two components, heavy (although not very well constrained) intrinsic absorption, and some excess that could be compatible with an Fe Kα emission line, although it is unclear due to our low statistics.

A41 PKS 2211−17 (3C 444)

PKS 2211−17 is another example of a cluster-embedded LERG (Croston et al. 2011). Its nuclear spectrum is very faint, with

Table B1. Observational details for the 3CRR sources with new *XMM–Newton* data. Post-filtering lifetimes are given for MOS1, MOS2 and PN.

Source	Observation ID	Lifetimes (s)
3C 19	0600450701	13 143, 13 848, 7786
3C 42	0600450301	18 181, 17 841, 15 165
3C 46	0600450501	7716, 7677, 4343
3C 67	0600450801	9319, 9832, 8719
4C 14.27	0600450401	14 390, 14 351, 11 203
3C 314.1	0600450101	17 949, 18 645, 12 092
3C 319	0600450201	7470, 7062, 4979
3C 341	0600450601	16 659, 16 624, 12 995

only ∼20 counts in the 0.4–7 keV energy range. We could only derive upper limits for both X-ray components.

A42 PKS 2221−02 (3C 445)

This object is a relatively well known BLRG. It has a very bright nucleus in the *K* band (Inskip et al. 2010) and an extended emission-line region (Balmaverde et al. 2008). The *Chandra* spectrum is bright, but not heavily piled up. The hard component dominates, and we detect a rather prominent Fe Kα emission line.

A43 PKS 2250−41

This source has a rather bright extended [O III] line emission (Tadhunter et al. 2002). Its *XMM* spectrum has a very faint accretion-related component, for which we were only able to derive an upper limit, although this is clearly a high-excitation object. As for PKS 1559+02, it is very likely that this object is Compton thick.

A44 PKS 2314+03 (3C 459)

The host galaxy of this NLRG is classified as a ULIRG due to its intense star formation activity (Dicken et al. 2012; Tadhunter et al. 2002), and it also has a strong radio core (Morganti et al. 1999), which offsets it slightly from the rest of the NLRG population in our 5 GHz plots. The X-ray spectrum has two distinct components and some intrinsic absorption, with some excess in the soft energy range.

A45 PKS 2356−61

This NLRG has a spectrum clearly dominated by the accretion-related component, with a noticeable Fe Kα emission line.

APPENDIX B: 3CRR TABLES

The X-ray properties of the 3CRR sources are largely taken from Hardcastle et al. (2009). They differ from the results presented in that paper in two ways: first, we make use of complete *Chandra* observations of the 3CRR sample with $z < 0.1$, which will be presented by Evans et al. (in prep.); secondly, we have used *XMM–Newton* observations taken with the aim of completing the X-ray observations of the 3CRR sample at $z < 0.5$, which are listed in Table B1. These were a uniform set of observations with a nominal on-source time of 15 ks, but some were badly affected by flaring. They were all analysed in the manner described by Hardcastle et al. (2009) and in the text.

In Table B2, we give the *K*-band magnitudes and derived quantities for the 3CRR sources discussed in the text, and Table B3 gives a complete list of the 3CRR luminosities and emission-line classifications, an update of the table presented by Hardcastle et al. (2009).

Table B2. *K*-band magnitudes, *K*-corrections (calculated using the relations of Glazebrook et al. 1995; Mannucci et al. 2001), absolute magnitudes, black hole masses, Eddington luminosities, X-ray, [O III] and IR-derived Eddington ratios and jet Eddington ratios for the sources in the 3CRR sample. The errors quoted for $L_{\rm X,\,rad}/L_{\rm X,\,Edd}$ are derived from the errors in the X-ray power-law normalization. Values preceded by a '<' indicate upper limits. E stands for LERG, N for NLRG, B for BLRG and Q for quasar. The *K* magnitudes given correspond to the following references: L – Lilly & Longair (1984), S – Simpson, Ward & Wall (2000), V – de Vries et al. (1998), B – Best, Longair & Roettgering (1998). 2M stands for sources where the measurements were taken directly from 2MASS.

PKS	Type	Ref	z	mag K_s	K-corr	Mag K_s	$M_{\rm BH}$ ($\times10^9$ M$_\odot$)	$L_{\rm Edd}$ ($\times10^{40}$ W)	$L_{\rm X,rad}/L_{\rm X,Edd}$	$L_{\rm [O\,III],rad}/L_{\rm [O\,III],Edd}$	$L_{\rm IR,rad}/L_{\rm IR,Edd}$	$Q/L_{\rm Edd}$
4C 12.03	E	L	0.156	13.130	−0.367	−26.60	1.54	2.00	$<9.20\times10^{-4}$	1.62×10^{-3}	–	1.18×10^{-2}
3C 20	N	L	0.174	14.060	−0.403	−25.96	0.95	1.24	$3.16^{+7.29}_{-0.90}\times10^{-2}$	4.58×10^{-3}	2.57×10^{-2}	7.98×10^{-2}
3C 28	E	L	0.195	13.570	−0.441	−26.77	1.75	2.27	$<9.97\times10^{-5}$	1.42×10^{-3}	8.27×10^{-4}	2.49×10^{-2}
3C 31	E	2M	0.017	8.481	−0.043	−25.77	0.82	1.07	$<2.92\times10^{-6}$	9.72×10^{-5}	8.55×10^{-4}	6.12×10^{-4}
3C 33	N	S	0.060	11.720	−0.150	−25.54	0.69	0.90	$2.75^{+2.54}_{-1.62}\times10^{-2}$	6.04×10^{-2}	2.41×10^{-2}	1.91×10^{-2}
3C 35	E	L	0.068	11.770	−0.170	−25.80	0.84	1.09	$<1.98\times10^{-3}$	3.43×10^{-4}	–	4.82×10^{-3}
3C 42	N	S	0.395	15.140	−0.648	−27.16	2.36	3.07	$2.99^{+4.67}_{-2.86}\times10^{-2}$	1.24×10^{-2}	–	5.42×10^{-2}
3C 46	N	V	0.437	14.830	−0.660	−27.74	3.67	4.78	–	4.59×10^{-2}	–	3.92×10^{-2}
3C 55	N	L	0.735	16.540	−0.763	−27.50	3.05	3.97	–	–	1.29×10^{-1}	2.59×10^{-1}
3C 66B	E	2M	0.022	9.500	−0.055	−25.36	0.60	0.78	$<2.22\times10^{-6}$	5.14×10^{-4}	6.37×10^{-4}	1.78×10^{-3}
3C 76.1	E	2M	0.032	10.870	−0.083	−24.95	0.44	0.57	$<2.76\times10^{-5}$	4.30×10^{-4}	8.04×10^{-4}	2.83×10^{-3}
3C 79	N	S	0.256	14.420	−0.534	−26.67	1.62	2.11	$2.71^{+13.20}_{-2.15}\times10^{-2}$	1.22×10^{-1}	9.85×10^{-2}	7.58×10^{-2}
3C 83.1B	E	2M	0.026	10.850	−0.065	−24.41	0.29	0.38	$<2.95\times10^{-5}$	–	1.88×10^{-3}	5.38×10^{-3}
3C 84	N	2M	0.018	8.126	−0.045	−26.26	1.19	1.55	$<1.90\times10^{-4}$	9.41×10^{-3}	1.79×10^{-2}	1.46×10^{-3}
3C 98	N	2M	0.031	10.930	−0.078	−24.74	0.38	0.49	$1.56^{+0.15}_{-0.15}\times10^{-3}$	7.52×10^{-3}	–	9.57×10^{-3}
3C 123	E	L	0.218	13.960	−0.479	−26.67	1.63	2.12	$4.54^{+1.58}_{-2.20}\times10^{-3}$	1.65×10^{-2}	6.21×10^{-3}	2.55×10^{-1}
3C 153	N	S	0.277	14.220	−0.560	−27.09	2.24	2.91	$<4.39\times10^{-4}$	5.25×10^{-3}	3.04×10^{-3}	3.43×10^{-2}
3C 171	N	S	0.238	14.720	−0.510	−26.17	1.11	1.45	$2.96^{+1.05}_{-0.89}\times10^{-2}$	1.87×10^{-1}	–	6.53×10^{-2}
DA 240	E	2M	0.036	10.724	−0.091	−25.30	0.58	0.75	$<1.17\times10^{-5}$	2.66×10^{-4}	–	4.81×10^{-1}
3C 172	N	L	0.519	15.670	−0.675	−27.36	2.75	3.58	–	–	9.14×10^{-3}	8.61×10^{-4}
3C 192	N	S	0.060	12.120	−0.151	−25.14	0.51	0.66	$5.78^{+10.30}_{-3.16}\times10^{-4}$	1.21×10^{-2}	2.69×10^{-3}	1.16×10^{-2}

Table B2 – (*Continued.*)

PKS	Type	Ref	z	mag K_s	K-corr	Mag K_s	$M_{\rm BH}$ ($\times 10^9$ M$_\odot$)	$L_{\rm Edd}$ ($\times 10^{40}$ W)	$L_{\rm X,rad}/L_{\rm X,Edd}$	$L_{\rm [O\,III],rad}/L_{\rm [O\,III],Edd}$	$L_{\rm IR,rad}/L_{\rm IR,Edd}$	$Q/L_{\rm Edd}$
3C 200	E	V	0.458	15.590	−0.665	−27.11	2.27	2.95	$<5.85 \times 10^{-3}$	–	7.58×10^{-3}	7.32×10^{-2}
3C 223	N	S	0.137	13.770	−0.328	−25.59	0.72	0.93	$1.35^{+6.90}_{-0.70} \times 10^{-2}$	5.64×10^{-2}	–	2.71×10^{-2}
3C 228	N	L	0.552	16.250	−0.682	−26.95	2.02	2.62	$4.51^{+6.33}_{-4.13} \times 10^{-3}$	–	2.02×10^{-2}	2.18×10^{-1}
3C 236	E	L	0.099	12.220	−0.244	−26.29	1.22	1.59	$<7.36 \times 10^{-4}$	1.75×10^{-3}	–	8.32×10^{-3}
3C 263.1	N	L	0.824	16.610	−0.818	−27.79	3.81	4.95	–	–	2.24×10^{-2}	2.24×10^{-1}
3C 264	E	2M	0.021	9.489	−0.053	−25.26	0.56	0.73	$<4.01 \times 10^{-6}$	6.97×10^{-5}	1.20×10^{-3}	1.96×10^{-3}
3C 272.1	E	2M	0.003	6.222	−0.007	−23.46	0.14	0.18	$<4.09 \times 10^{-7}$	1.80×10^{-5}	4.04×10^{-4}	1.96×10^{-4}
3C 274	E	2M	0.004	5.812	−0.011	−25.38	0.61	0.79	$<1.64 \times 10^{-7}$	3.95×10^{-5}	2.52×10^{-4}	2.61×10^{-3}
3C 274.1	N	L	0.422	15.360	−0.657	−27.12	2.29	2.97	$<3.02 \times 10^{-3}$	2.67×10^{-3}	5.32×10^{-3}	8.56×10^{-2}
3C 280	N	B	0.996	16.800	−0.902	−28.19	5.17	6.72	$1.09^{+0.55}_{-0.48} \times 10^{-1}$	–	7.33×10^{-2}	3.06×10^{-1}
3C 284	N	L	0.239	13.990	−0.512	−26.91	1.96	2.54	$1.26^{+7.94}_{-1.22} \times 10^{-2}$	5.45×10^{-3}	–	2.37×10^{-2}
3C 285	N	L	0.079	12.440	−0.198	−25.53	0.68	0.89	$5.94^{+1.63}_{-1.23} \times 10^{-3}$	1.44×10^{-3}	–	8.61×10^{-3}
3C 288	E	L	0.246	13.420	−0.521	−27.56	3.21	4.17	$<9.65 \times 10^{-5}$	–	1.14×10^{-3}	2.34×10^{-2}
3C 289	N	B	0.967	16.720	−0.891	−28.18	5.13	6.67	–	–	3.57×10^{-2}	1.62×10^{-1}
3C 293	E	2M	0.045	10.841	−0.115	−25.77	0.82	1.07	$1.16^{+0.12}_{-0.11} \times 10^{-3}$	2.14×10^{-4}	4.87×10^{-3}	2.69×10^{-3}
3C 295	N	L	0.461	14.330	−0.665	−28.39	5.99	7.79	$1.85^{+6.61}_{-0.26} \times 10^{-2}$	4.36×10^{-3}	1.49×10^{-2}	1.52×10^{-1}
3C 296	E	2M	0.024	8.764	−0.061	−26.30	1.23	1.60	$<1.44 \times 10^{-5}$	1.19×10^{-4}	3.55×10^{-5}	6.12×10^{-4}
3C 300	N	L	0.272	15.110	−0.554	−26.16	1.10	1.43	$<2.88 \times 10^{-4}$	2.54×10^{-2}	4.37×10^{-3}	7.83×10^{-2}
3C 305	N	2M	0.042	10.643	−0.106	−25.75	0.81	1.05	$<6.56 \times 10^{-6}$	3.67×10^{-3}	–	3.01×10^{-3}
3C 310	E	L	0.054	11.660	−0.137	−25.39	0.61	0.80	–	2.29×10^{-4}	7.24×10^{-4}	1.87×10^{-2}
3C 315	N	L	0.108	12.920	−0.266	−25.84	0.87	1.12	$<2.53 \times 10^{-4}$	2.37×10^{-3}	2.73×10^{-3}	1.71×10^{-2}
3C 319	E	L	0.192	14.910	−0.436	−25.15	0.51	0.66	$<1.49 \times 10^{-3}$	7.99×10^{-4}	2.54×10^{-3}	7.65×10^{-2}
3C 321	N	L	0.096	12.220	−0.237	−26.24	1.17	1.52	$6.48^{+172.00}_{-4.38} \times 10^{-4}$	1.86×10^{-3}	6.48×10^{-2}	7.88×10^{-3}
3C 326	E	L	0.090	13.070	−0.222	−25.20	0.53	0.69	–	2.14×10^{-5}	9.48×10^{-4}	2.26×10^{-2}
NGC 6109	E	2M	0.030	10.325	−0.076	−25.27	0.56	0.73	$<3.51 \times 10^{-6}$	–	–	1.70×10^{-3}
3C 337	N	B	0.635	16.550	−0.709	−27.05	2.17	2.82	–	–	1.14×10^{-2}	1.52×10^{-1}
3C 338	E	2M	0.030	9.170	−0.077	−26.50	1.43	1.86	$<2.32 \times 10^{-6}$	6.47×10^{-5}	2.72×10^{-4}	2.61×10^{-3}
3C 340	N	B	0.775	16.920	−0.788	−27.29	2.60	3.38	–	–	2.84×10^{-2}	1.71×10^{-1}
3C 341	N	L	0.448	15.330	−0.663	−27.31	2.64	3.43	$1.05^{+2.32}_{-0.61} \times 10^{-3}$	6.38×10^{-2}	9.22×10^{-2}	5.81×10^{-2}
NGC 6251	E	2M	0.024	9.026	−0.062	−26.14	1.08	1.41	$<6.72 \times 10^{-6}$	–	1.70×10^{-3}	6.01×10^{-4}
3C 346	N	L	0.162	13.100	−0.379	−26.73	1.70	2.21	$<1.60 \times 10^{-4}$	3.36×10^{-3}	7.84×10^{-3}	1.18×10^{-2}
3C 349	N	L	0.205	14.470	−0.458	−26.00	0.98	1.27	$1.76^{+0.26}_{-0.24} \times 10^{-2}$	1.00×10^{-2}	–	3.91×10^{-2}
3C 352	N	B	0.806	16.720	−0.807	−27.61	3.32	4.32	–	–	1.85×10^{-2}	1.63×10^{-1}
3C 386	E	2M	0.018	9.673	−0.045	−24.71	0.37	0.48	$<2.19 \times 10^{-6}$	1.31×10^{-3}	4.53×10^{-4}	2.05×10^{-3}
3C 388	E	L	0.091	11.960	−0.225	−26.34	1.26	1.64	$<6.68 \times 10^{-5}$	1.10×10^{-3}	9.90×10^{-4}	1.12×10^{-2}
3C 433	N	L	0.102	11.900	−0.250	−26.69	1.65	2.15	$1.24^{+0.42}_{-0.38} \times 10^{-2}$	7.86×10^{-3}	2.94×10^{-2}	2.15×10^{-2}
3C 436	N	L	0.215	13.840	−0.474	−26.76	1.73	2.26	$3.67^{+2.75}_{-1.52} \times 10^{-3}$	5.62×10^{-3}	3.45×10^{-3}	3.15×10^{-2}
3C 438	E	L	0.290	13.900	−0.574	−27.54	3.16	4.11	$<6.48 \times 10^{-4}$	2.51×10^{-3}	1.20×10^{-3}	6.87×10^{-2}
3C 441	N	B	0.708	16.200	−0.747	−27.72	3.62	4.71	–	–	1.70×10^{-2}	1.24×10^{-1}
3C 442A	E	2M	0.027	9.860	−0.069	−25.57	0.70	0.92	$<7.58 \times 10^{-6}$	–	–	1.67×10^{-3}
3C 449	E	2M	0.017	9.070	−0.044	−25.31	0.58	0.75	$<2.73 \times 10^{-6}$	7.45×10^{-5}	3.27×10^{-5}	6.51×10^{-4}
3C 452	N	L	0.081	12.030	−0.202	−26.00	0.98	1.27	$4.50^{+16.20}_{-3.70} \times 10^{-2}$	6.09×10^{-3}	1.85×10^{-2}	2.35×10^{-2}
NGC 7385	E	2M	0.024	9.540	−0.062	−25.62	0.73	0.95	$<1.05 \times 10^{-5}$	–	–	9.18×10^{-4}
3C 457	N	L	0.428	15.720	−0.658	−26.80	1.79	2.33	$7.93^{+13.70}_{-0.89} \times 10^{-2}$	4.61×10^{-2}	–	9.42×10^{-2}
3C 465	E	2M	0.029	10.070	−0.075	−25.52	0.68	0.88	$<9.31 \times 10^{-6}$	2.42×10^{-4}	6.75×10^{-4}	4.04×10^{-3}

Table B3. Luminosities for the sources in the 3CRR sample, following the format of Hardcastle et al. (2006, 2009) (see also Table 4). The values are given as the logarithm of the luminosity in erg s^{-1}; upper limits are indicated with a '<' sign before the value. We have converted the radio and IR luminosity densities into νL_ν to allow for direct comparison between the magnitudes in different bands. Where measurements could not be obtained, their absence is indicated with an en dash. E stands for LERG, N for NLRG, B for BLRG and Q for quasar.

PKS	Type	z	L_{178}	L_5	$L_{\rm X_u}$	$L_{\rm X_u}-$	$L_{\rm X_u}+$	$L_{\rm X_a}$	$L_{\rm X_a}-$	$L_{\rm X_a}+$	$L_{\rm IR}$	$L_{\rm [O\,III]}$	$L_{\rm [O\,III]}$	$L_{\rm [O\,III]}$
4C 12.03	E	0.156	42.10	40.00	<41.91	–	–	<43.02	–	–	–	–	40.97	–
3C 6.1	N	0.840	43.87	41.61	44.92	44.89	44.94	<44.17	–	–	45.100	0.010	–	42.15
3C 16	E	0.405	43.09	39.73	<42.74	–	–	<43.69	–	–	–	–	–	41.81
3C 19	N	0.482	43.25	40.14	44.09	44.06	44.12	<43.55	–	–	–	–	–	–
3C 20	N	0.174	42.82	39.97	42.56	42.45	42.64	44.05	43.94	44.44	44.293	0.004	41.21	40.73
3C 22	B	0.938	43.96	41.95	–	–	–	–	–	–	45.900	0.010	–	43.16
3C 28	E	0.195	42.54	<38.96	<41.36	–	–	<42.27	–	–	<42.740	–	40.96	41.81
3C 31	E	0.017	40.31	39.45	40.65	40.54	40.74	<40.63	–	–	42.341	0.002	39.47	–
3C 33	N	0.060	41.95	39.98	41.92	41.88	41.97	43.90	43.60	44.11	44.080	0.012	42.19	41.44
3C 33.1	B	0.181	42.34	40.68	42.43	42.14	42.59	44.38	44.26	44.66	44.878	0.002	42.30	–

Table B3 – (*Continued.*)

PKS	Type	z	L_{178}	L_5	L_{X_u}	$L_{X_u}-$	$L_{X_u}+$	L_{X_a}	$L_{X_a}-$	$L_{X_a}+$	L_{IR}	$L_{[O\,III]}$	$L_{[O\,III]}$	$L_{[O\,III]}$
3C 34	N	0.689	43.70	40.80	–	–	–	–	–	–	–	–	–	43.61
3C 35	E	0.068	41.35	39.77	<40.85	–	–	<43.07	–	–	–	–	40.03	–
3C 41	N	0.795	43.66	40.72	–	–	–	–	–	–	–	–	–	42.70
3C 42	N	0.395	43.07	40.67	42.61	42.44	42.73	44.33	43.28	44.64	–	–	42.04	41.89
3C 46	N	0.437	43.16	40.75	–	–	–	–	–	–	–	–	42.80	42.22
3C 47	Q	0.425	43.52	42.23	45.01	44.97	45.04	45.05	44.77	45.21	45.805	0.004	43.28	42.63
3C 48	Q	0.367	43.64	43.18	45.00	45.00	45.01	45.00	45.00	45.01	46.146	0.002	43.12	42.25
3C 49	N	0.621	43.44	41.54	–	–	–	–	–	–	–	–	–	–
3C 55	N	0.735	44.02	41.57	–	–	–	–	–	–	45.820	0.013	–	42.34
3C 61.1	N	0.186	42.76	40.00	41.92	41.58	42.10	43.93	43.74	44.10	43.700	0.030	42.49	41.44
3C 66B	E	0.022	40.69	39.97	41.04	41.00	41.08	<40.39	–	–	42.008	0.004	40.06	39.87
3C 67	B	0.310	42.73	40.82	44.26	44.23	44.29	44.26	43.55	44.29	–	–	42.83	42.26
3C 76.1	E	0.032	40.75	39.07	40.96	40.79	41.12	<41.28	–	–	41.966	0.017	<39.85	–
3C 79	N	0.256	43.07	40.90	42.42	42.34	42.49	44.18	43.65	44.75	45.326	0.004	42.86	42.21
3C 83.1B	E	0.026	40.88	39.46	40.91	40.15	41.54	<41.14	–	–	42.205	0.004	–	–
3C 84	N	0.018	40.92	42.32	42.54	42.52	42.57	<42.37	–	–	44.217	–	41.62	41.09
3C 98	N	0.031	41.29	38.97	40.65	40.51	40.76	42.71	42.67	42.74	–	–	41.02	40.24
3C 109	B	0.306	43.08	42.48	45.23	45.18	45.29	45.23	44.60	45.29	45.975	0.001	43.32	42.09
4C 14.11	E	0.206	42.41	41.18	43.01	42.94	43.07	<42.78	–	–	–	–	41.24	–
3C 123	E	0.218	43.68	41.76	42.00	41.05	42.27	43.58	43.36	43.68	43.810	0.067	42.00	–
3C 132	N	0.214	42.52	40.10	<41.99	–	–	43.25	43.04	43.40	–	–	–	–
3C 138	Q	0.759	43.92	42.85	–	–	–	–	–	–	45.800	0.010	43.46	42.57
3C 147	Q	0.545	44.04	43.98	–	–	–	–	–	–	45.500	0.010	43.79	43.45
3C 153	N	0.277	42.82	<40.20	<41.99	–	–	<42.89	–	–	43.590	0.097	41.64	42.49
3C 171	N	0.238	42.80	40.18	41.86	41.69	41.98	44.08	43.96	44.18	–	–	42.89	42.45
3C 172	N	0.519	43.46	40.17	–	–	–	–	–	–	44.310	0.062	–	42.77
3C 173.1	E	0.292	42.90	40.89	41.55	41.34	41.69	<43.13	–	–	43.400	0.079	40.85	–
3C 175	Q	0.768	43.96	42.26	–	–	–	–	–	–	45.700	0.010	43.10	42.77
3C 175.1	N	0.920	43.95	42.09	–	–	–	–	–	–	–	–	–	42.67
3C 184	N	0.994	44.08	<40.41	43.48	42.48	43.95	44.76	44.57	44.90	45.300	0.010	–	42.89
3C 184.1	N	0.119	41.95	39.99	41.73	41.45	41.89	43.91	43.70	44.22	–	–	42.23	41.48
DA 240	E	0.036	41.08	40.17	40.90	40.78	41.01	<40.80	–	–	–	–	39.76	40.04
3C 192	N	0.060	41.54	39.51	40.65	40.38	40.72	42.46	42.18	42.83	42.710	0.028	41.36	41.31
3C 196	Q	0.871	44.63	41.84	–	–	–	–	–	–	46.000	0.010	–	–
3C 200	E	0.458	43.21	41.97	43.58	43.52	43.64	<43.78	–	–	44.100	0.010	–	–
4C 14.27	N	0.392	43.05	<39.68	42.34	42.17	42.48	<43.05	–	–	–	–	–	–
3C 207	Q	0.684	43.71	43.49	45.14	45.06	45.19	45.14	45.06	45.19	45.500	0.010	43.05	<42.15
3C 215	Q	0.411	43.13	41.54	44.84	44.81	44.87	44.84	44.46	44.87	–	–	42.59	42.22
3C 217	N	0.898	43.88	<40.80	–	–	–	–	–	–	–	–	–	43.29
3C 216	Q	0.668	43.84	43.79	–	–	–	–	–	–	45.700	0.010	<42.46	42.43
3C 219	B	0.174	42.82	41.27	43.99	43.94	44.04	43.99	43.94	44.04	44.210	0.016	41.77	41.27
3C 220.1	N	0.610	43.66	42.08	44.50	44.48	44.52	<44.04	–	–	44.700	0.010	42.79	42.46
3C 220.3	N	0.685	43.74	<40.02	–	–	–	–	–	–	45.100	0.010	–	–
3C 223	N	0.137	42.14	40.29	43.16	43.12	43.19	43.67	43.43	44.27	–	–	42.18	41.71
3C 225B	N	0.580	43.74	40.68	–	–	–	–	–	–	44.483	0.129	–	42.62
3C 226	N	0.820	43.94	41.82	–	–	–	–	–	–	46.261	0.006	–	42.74
4C 73.08	N	0.058	41.35	39.62	41.48	41.36	41.57	43.59	43.45	43.90	–	–	40.94	40.57
3C 228	N	0.552	43.71	41.72	43.86	42.81	43.91	43.65	42.81	43.94	44.574	0.087	–	42.15
3C 234	N	0.185	42.76	41.56	42.89	42.87	42.91	44.36	44.26	44.60	45.590	0.006	43.13	42.12
3C 236	E	0.099	41.82	40.98	42.84	41.80	43.18	<42.86	–	–	–	–	40.90	41.17
4C 74.16	?	0.810	43.82	41.11	–	–	–	–	–	–	–	–	–	–
3C 244.1	N	0.428	43.39	40.66	43.25	43.10	43.36	<42.92	–	–	45.130	0.009	43.03	–
3C 247	N	0.749	43.63	41.41	–	–	–	–	–	–	–	–	–	43.01
3C 249.1	Q	0.311	42.79	41.93	44.72	44.57	44.77	44.74	44.43	45.04	45.493	0.001	43.38	–
3C 254	Q	0.734	43.96	42.13	45.32	45.25	45.40	45.32	45.25	45.40	45.600	0.010	43.71	43.13
3C 263	Q	0.652	43.69	42.94	45.18	45.12	45.24	45.18	45.12	45.24	45.800	0.010	43.71	42.90
3C 263.1	N	0.824	44.02	41.45	–	–	–	–	–	–	44.980	0.016	–	42.97
3C 264	E	0.021	40.69	39.98	41.90	41.89	41.91	<40.60	–	–	42.315	0.003	39.16	40.10
3C 265	N	0.811	44.06	41.40	43.45	43.33	43.54	44.49	44.28	44.63	45.860	0.010	43.80	43.85
3C 268.1	N	0.973	44.19	41.39	–	–	–	–	–	–	45.300	0.010	–	42.27
3C 268.3	B	0.371	42.92	40.24	–	–	–	–	–	–	–	–	42.49	–
3C 272.1	E	0.003	38.84	38.22	39.69	39.63	39.75	<39.04	–	–	40.964	0.001	37.98	–
A1552	E	0.084	41.59	40.34	<40.92	–	–	<42.21	–	–	–	–	–	–
3C 274	E	0.004	40.88	39.87	40.53	40.51	40.56	<39.28	–	–	41.506	0.003	38.95	–

Table B3 – (*Continued.*)

PKS	Type	z	L_{178}	L_5	L_{X_u}	$L_{X_u}-$	$L_{X_u}+$	L_{X_a}	$L_{X_a}-$	$L_{X_a}+$	L_{IR}	$L_{[O\,III]}$	$L_{[O\,III]}$	$L_{[O\,III]}$
3C 274.1	N	0.422	43.29	40.83	43.27	43.21	43.33	<43.56	–	–	<43.910	–	41.36	–
3C 275.1	Q	0.557	43.64	42.72	44.52	44.51	44.54	44.52	44.51	44.54	45.100	0.010	–	42.67
3C 277.2	N	0.766	43.81	40.57	43.67	43.61	43.72	<43.81	–	–	–	–	–	43.21
3C 280	N	0.996	44.32	41.11	42.85	42.55	43.03	45.00	44.81	45.13	45.800	0.010	–	43.68
3C 284	N	0.239	42.57	40.35	42.22	42.19	42.26	43.98	42.80	44.63	–	–	41.60	–
3C 285	N	0.079	41.53	39.64	40.54	40.26	40.76	43.38	43.30	43.46	–	–	40.56	40.46
3C 286	Q	0.849	44.03	41.85	–	–	–	–	–	–	45.600	0.010	–	42.69
3C 288	E	0.246	42.81	41.34	<41.41	–	–	<42.48	–	–	<43.250	–	–	–
3C 289	N	0.967	43.99	42.11	–	–	–	–	–	–	45.400	0.010	–	42.57
3C 292	N	0.710	43.60	40.82	43.62	43.32	43.80	44.40	44.26	44.51	44.800	0.010	–	–
3C 293	E	0.045	41.06	40.36	40.97	40.79	41.15	42.88	42.85	42.91	43.300	0.001	39.81	41.56
3C 295	N	0.461	44.05	40.91	42.50	42.18	42.68	44.48	44.43	44.97	45.004	0.005	41.99	42.33
3C 296	E	0.024	40.51	39.68	41.38	41.15	41.62	<41.42	–	–	40.816	0.097	39.74	–
3C 299	N	0.367	42.98	40.23	–	–	–	–	–	–	–	–	–	42.66
3C 300	N	0.272	42.88	40.91	43.40	43.38	43.42	<42.49	–	–	43.400	0.146	42.02	42.48
3C 303	B	0.141	42.05	41.54	43.91	43.85	43.97	43.91	43.85	43.97	–	–	41.74	41.90
3C 305	N	0.042	41.09	39.75	40.56	40.30	40.72	<40.95	–	–	–	–	41.04	40.13
3C 309.1	Q	0.904	44.12	44.40	45.78	45.76	45.79	45.78	45.76	45.79	46.000	0.010	43.70	42.94
3C 310	E	0.054	41.87	40.42	40.26	39.00	40.58	<42.19	–	–	42.089	0.032	40.07	–
3C 314.1	E	0.120	41.88	<39.22	41.38	41.12	41.54	<42.30	–	–	42.098	0.097	39.70	–
3C 315	N	0.108	42.00	<41.31	<41.20	–	–	<42.36	–	–	43.010	0.048	40.88	–
3C 319	E	0.192	42.49	<39.64	42.47	42.29	42.64	<42.80	–	–	<42.680	–	<40.18	39.98
3C 321	N	0.096	41.77	40.50	41.54	41.45	41.62	42.80	42.40	43.94	44.916	0.001	40.91	41.32
3C 326	E	0.090	41.89	40.08	42.20	42.15	42.23	<41.25	–	–	<42.160	–	40.40	41.25
3C 325	Q	0.860	43.96	41.37	<43.16	–	–	44.56	44.43	44.70	45.600	0.010	–	42.79
3C 330	N	0.549	43.76	40.46	43.08	42.99	43.15	43.90	43.60	44.00	45.000	0.010	–	43.19
NGC 6109	E	0.030	40.62	39.44	40.04	39.60	40.26	<40.55	–	–	–	–	–	–
3C 334	Q	0.555	43.39	42.64	45.08	44.99	45.15	45.08	44.99	45.15	45.700	0.010	43.37	42.54
3C 336	Q	0.927	43.91	42.36	–	–	–	–	–	–	45.400	0.010	43.46	–
3C 341	N	0.448	43.17	40.41	42.77	42.57	42.92	43.25	42.95	43.64	45.558	0.002	42.80	41.77
3C 338	E	0.030	41.29	40.03	40.51	40.38	40.59	<40.76	–	–	42.018	0.007	39.54	40.79
3C 340	N	0.775	43.67	40.94	–	–	–	–	–	–	44.900	0.010	–	42.67
3C 337	N	0.635	43.52	40.18	–	–	–	–	–	–	44.300	0.010	–	41.63
3C 343	Q	0.988	43.90	<43.58	–	–	–	–	–	–	45.900	0.010	42.68	41.99
3C 343.1	N	0.750	43.59	<43.17	–	–	–	–	–	–	44.700	0.010	42.71	42.44
NGC 6251	E	0.024	40.43	40.35	42.74	42.72	42.76	<41.08	–	–	42.873	0.001	–	–
3C 346	N	0.162	42.15	41.83	43.40	43.38	43.41	<42.44	–	–	43.960	0.004	41.33	–
3C 345	Q	0.594	43.34	44.59	45.64	45.58	45.71	45.64	45.58	45.71	–	–	–	–
3C 349	N	0.205	42.48	41.10	41.82	41.52	41.92	43.87	43.82	43.91	–	–	41.56	–
3C 351	Q	0.371	43.06	41.05	41.92	41.74	42.08	44.80	44.77	44.82	46.005	0.001	42.84	–
3C 352	N	0.806	43.80	41.43	–	–	–	–	–	–	44.800	0.010	–	43.05
3C 380	Q	0.691	44.32	44.67	45.81	45.72	45.89	45.81	45.72	45.89	45.900	0.010	43.76	42.99
3C 381	B	0.161	42.34	40.18	42.11	42.00	42.20	44.31	44.18	44.44	44.650	0.010	42.38	40.92
3C 382	B	0.058	41.48	40.85	44.58	44.57	44.59	44.58	44.57	44.59	44.240	0.008	41.78	40.73
3C 386	E	0.018	40.51	39.62	39.49	38.45	39.83	<40.18	–	–	41.550	0.007	<40.25	–
3C 388	E	0.091	41.98	40.77	41.74	41.65	41.81	<42.01	–	–	42.660	0.049	40.71	40.52
3C 390.3	B	0.057	41.85	41.08	44.18	44.15	44.23	44.18	44.15	44.23	44.370	0.011	42.11	40.95
3C 401	E	0.201	42.65	41.19	42.74	42.69	42.79	<43.05	–	–	43.170	0.125	41.06	–
3C 427.1	E	0.572	43.83	40.53	<42.45	–	–	<43.24	–	–	<43.800	–	–	–
3C 433	N	0.102	42.45	39.77	41.06	40.77	41.22	43.92	43.80	44.02	44.670	0.005	41.68	–
3C 436	N	0.215	42.65	41.02	42.59	42.55	42.62	43.53	43.35	43.72	43.520	0.062	41.56	–
3C 438	E	0.290	43.35	40.87	42.67	42.39	42.84	<43.14	–	–	<43.270	–	<41.47	–
3C 441	N	0.708	43.70	41.36	–	–	–	–	–	–	44.800	0.010	–	42.42
3C 442A	E	0.027	40.71	38.21	40.00	39.60	40.42	<40.95	–	–	–	–	–	40.56
3C 449	E	0.017	40.16	39.08	40.49	40.43	40.54	<40.46	–	–	40.358	0.084	39.21	–
3C 452	N	0.081	42.23	40.99	41.77	41.52	41.94	44.18	43.60	44.67	44.130	0.010	41.35	41.44
NGC 7385	E	0.024	40.44	39.90	41.11	41.00	41.26	<41.10	–	–	–	–	–	–
3C 454.3	Q	0.859	43.70	45.07	46.37	46.24	46.47	46.37	46.24	46.47	–	–	–	–
3C 455	Q	0.543	43.41	40.72	–	–	–	–	–	–	–	–	43.07	42.81
3C 457	N	0.428	43.23	40.69	43.35	43.30	43.40	44.56	44.52	44.88	–	–	42.49	–
3C 465	E	0.029	41.16	40.41	40.91	40.57	41.42	<41.02	–	–	42.109	0.007	39.79	–

This paper has been typeset from a TEX/LATEX file prepared by the author.